Magnetic structure and magneto-transport properties of Fe–based Heusler alloys

Ph.D. THESIS

By

KULBHUSHAN MISHRA

DEPARTMENT OF PHYSICS

INDIAN INSTITUTE OF TECHNOLOGY INDORE

April 2025

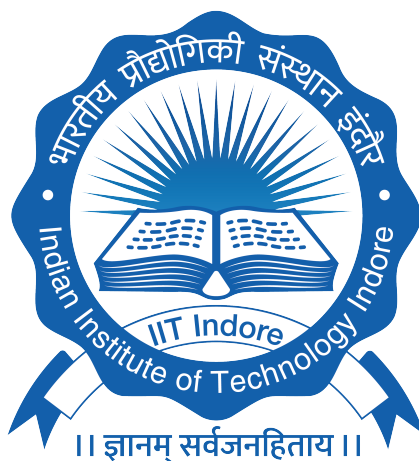# Magnetic structure and magneto-transport properties of Fe–based Heusler alloys

A THESIS

Submitted in partial fulfillment of the

requirements for the award of the degree

of

DOCTOR OF PHILOSOPHY

by

KULBHUSHAN MISHRA

DEPARTMENT OF PHYSICS

INDIAN INSTITUTE OF TECHNOLOGY INDORE

April 2025

INDIAN INSTITUTE OF TECHNOLOGY INDORE

CANDIDATE'S DECLARATION

I hereby certify that the work which is presented in the thesis entitled **MAGNETIC STRUCTURE AND MAGNETO-TRANSPORT PROPERTIES OF Fe-BASED HEUSLER ALLOYS** in the partial fulfillment of the requirements for the award of the degree of **DOCTOR OF PHILOSOPHY** and submitted in the **DEPARTMENT OF PHYSICS, Indian Institute of Technology Indore**, is an authentic record of my own work carried out during the time period from January 2020 to April 2025 under the supervision of Prof. Preeti A. Bhobe, Professor, Department of Physics, Indian Institute of Technology Indore.

The matter presented in this thesis has not been submitted by me for the award of any other degree of this or any other institute.
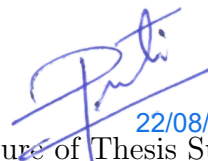
Kulbhushan 22/08/2025
Signature of student with date

Kulbhushan Mishra

- -

This is to certify that the above statement made by the candidate is correct to the best of my/our knowledge.

22/08/2025
Signature of Thesis Supervisor with date

Prof. Preeti A. Bhobe

- -

Kulbhushan Mishra, has successfully given his Ph.D. Oral Examination held on

22/08/2025
Signature of Thesis Supervisor

Date:

- -

Acknowledgments

If I remember correctly, it was a warm evening during the peak summer of 2019 in Punjab. We were celebrating Chandra Prakash's PhD admission; we call him CP. We laughed until we couldn't breathe when he recounted his interview story. Apparently, he had confidently told the committee, *"I rejected IIT Indore,"* only for them to correct him: *"No, IIT Indore rejected you!"* It was CP's endearing innocence and uniquely funny English that made his stories about IIT Indore all the more entertaining. Just six months later, I found myself walking into the same place, appearing for my PhD interview at the Department of Physics, IIT Indore. I was almost blank, unaware of the faculty members or their research areas. Yet, without much hesitation, I marked *Prof. Preeti Bhobe* as my preferred supervisor and listed *magnetism* as my research interest. Five years later, that spontaneous decision has turned out to be one of my life's most surprising—and fulfilling—chapters.

Preeti Ma'am is an outstanding mentor, and her vision for research is humbling. She surprises you with her observations and her ability to bring the best out of you. Her tenacity to continue with research against all odds, hitting the problem hard with all her strength, and a contagious smile. Her flexibility to jump into unexplored areas and make a way through. But that is just one part of her. She has been a guide cum friend to me, who stood as a strongest pillar of support during the difficult times. She has been a companion in my grief and happier than me in my happiness. There are countless reasons to thank her, but let's not attempt to. Through Preeti Ma'am, I also met Prof. Priolkar. He has had a deep impression on me, both physics-wise and as a character in general. His smile and calmness are contagious. We all in the lab admire him or, say, adore him. I thank him for all his patience, hearing, chats and laughs, and teaching various things. His encouragement and support, his appreciation and care.

I sincerely thank Prof. Pankaj R. Sagdeo and Prof. I. A. Palani for being part of my doctoral committee. Their insightful comments, motiva-

tion, and support inspired me in many ways.

I gratefully acknowledge Prof. A. K. Nigam and Prof. Pratap Raychaudhuri for generously extending access to laboratory facilities for various magnetic measurements. Their support has been instrumental in carrying out key experiments during the course of my research.

I sincerely thank Dr. Elaine, Goa University, for her constant guidance and willingness to help with every aspect of the neutron diffraction experimental work. Her support has been crucial throughout the process.

I am also deeply thankful to Dr. A. D. Fortes and Dr. Christopher M. Howard from the Rutherford Appleton Laboratory, UK, for their invaluable assistance during neutron diffraction measurements and for their insightful feedback during data analysis.

I thank Dr. Shishir Kumar Pandey for carrying out the density functional theory (DFT) calculations and contributing significantly to my work's theoretical understanding.

I am grateful to Dr. Rajeev Rawat, UGC-DAE CSR, Indore, for facilitating magneto-transport and specific heat measurements and for many fruitful discussions that helped shape the interpretation of the data. I would also like to thank Rajeev Joshi and Priyanshi for their kind help and support during these measurements.

Finally, I extend my thanks to my friends at UGC-DAE CSR, Indore—Praveen, Pramod, Najneen, Ashutosh, Dharmendra, and Akshaya—for their camaraderie and for making my visits both enjoyable and memorable.

I now take a moment to acknowledge the thorns and roses of my life—my friends. In countless ways, they surround you: to support you, to help you, and—when you least expect it—to pull your leg. A true friend is a double-edged sword, and it's nearly impossible to thank them enough for their terrible jokes, brutal teasing, spontaneous dance moves, and late-night conversations that suddenly turn serious. To my M.Sc.

batchmates—Sudhakar and CP— for being the best duo of my life. Abhinav, for those unexpected bursts of motivation and random campus walks that always came at the right time. Nikhitha, for her kindness, unwavering support, and constant faith in me. Umashankar, birthdays could not have been more fun, and summer noons would have been a little less painful without him. I also express my gratitude to the professors who taught me during my M.Sc.—Verma Sir, Mann Sir, Sinha Sir, and P.K. Ma'am—for their kindness and encouragement, and for making me believe that hard work does indeed pay off.

I have been fortunate to share my journey at IIT Indore with a wonderful group of friends who made this phase truly memorable. Ashwani—without him, this place would have felt very different. His quirky yet funny suggestions, long walks, and endless philosophical conversations have genuinely helped me grow into a better version of myself. Abhishek, Vivek, Kailash, and Anuradha—thank you for the countless tea breaks, card games, late-night chats, shared laughter over good food, and a constant sense of belonging. Swapnesh—for engaging physics discussions, encouraging me to play football, and for sharing an exasperating perspective on life. Shraddha—for the unforgettable Ujjain trip and chess battles, and most importantly, for showing me how to remain hopeful and happy in every situation. Shushmita — for the endless discussions on the theoretical aspects of my work, for constantly encouraging me to think of newer ideas, and for the many good times we shared over tea breaks.

I want to acknowledge the people I spent most of my days with—my labmates. Bikash is a senior, labmate, flatmate, and above all, a true friend. For sharing and being a partner in all my adventures, the burden of daily struggles, cooking amazing meals, and being my last resort in times of worry. Like an elder brother, he has always pulled me out of trouble before I even realized I was in it. Anlin, Aarti, Astha—for always being honest, pointing out my flaws without hesitation, and constantly reminding me to stay grounded. Prathmesh and Ramavatar, without them, tea breaks and city trips could not have been more joyous and fun.

Now, I would like to thank my senior labmates, Dr. Mithun, Dr. Sayan, Dr. Gowtham, and Dr. Tamalika, whose insights, encouragement, and willingness to share their experience have been invaluable throughout my research.

Finally, I would like to express my heartfelt gratitude to the many people who have shaped me—my parents, brothers and sisters, and teachers. Their unwavering love, support, and guidance have made this journey meaningful and fulfilling.

.

Dedicated to the family

LIST OF PUBLICATIONS

Based on this thesis:

1. **Kulbhushan Mishra**, P. A. Bhobe, "Magnetic properties and identification of Griffiths-like phase in Mn_2FeSi Heusler antiferromagnet," *J. Alloys. Compd*, **970**, 172611 (2024).

2. **Kulbhushan Mishra**, Bibhas Ghanta, A. K. Bera, and P. A. Bhobe, "Identification of disorder and effect of annealing on physical properties of half-metallic Fe-Ti-Sn based Heusler alloys," *J. App. Phy.*, **137**, 075137 (2025).

3. **Kulbhushan Mishra**, Shishir Kumar Pandey, S. Chaudhuri, Rajeev Rawat, and P. A. Bhobe, "Observation of Kondo-like electrical transport in ferromagnetic $Fe_2Ti_{1-x}Mn_xSn$ Heusler Alloys," Phy. Rev. B **111**, 235146 (2025).

4. **Kulbhushan Mishra**, Elaine T. Dias, Rajeev Joshi, A. D. Fortes, Christopher M. Howard, Rajeev Rawat, and P. A. Bhobe, "Evidence of magnetoelastic coupling and magnetic phase coexistence in $Mn_{1.7}Fe_{1.3}Si$ Heusler Alloy," Under review.

Outside of this thesis:

1. **Kulbhushan Mishra**, Rajeev Joshi, Rajeev Rawat, and P. A. Bhobe, "Semiconductor-like electrical transport and weak localization in disordered $Fe_2Ti_{0.5}Mn_{0.5}Sn$ Heusler alloys," Under review

2. Shivendu Mishra, Dilip Pandey, **Kulbhushan Mishra**, Lydie Viau, and Abhinav Raghuvanshi,"Copper(i) iodide coordination polymers with triazole substituted pyridine ligands: photophysical and electrical conductivity properties," *New J. Chem.*, **47**, 19751 (2023);

Presentation at conferences/meetings:

1. Oral presentation on "Tunable magnetic properties and occurrence of half-metallicity in Fe-based Heusler alloys" at 34th AGM of Materials Research Society of India (December 2023) (organized at IIT BHU)..

2. Poster presentation on "Study of structural and transport properties of Al substituted Fe_2TiSn" **Kulbhushan Mishra**, Sayan Chaudhury, and P. A. Bhobe, 65th DAE Solid State Physics Symposium, 2021.

3. Poster presentation on "Structural and magnetic properties of $Mn_2FeSi_{1-x}Al_x$", **Kulbhushan Mishra**, P. A. Bhobe, 66th DAE Solid State Physics Symposium, (December 2022) (organized at BIT Mesra, Ranchi).

4. Poster presentation on "Structural, magnetic and transport properties of Mn-Fe based Heusler alloys" **Kulbhushan Mishra**, P.A. Bhobe, International Conference on Applied Materials (February 2023) (organized at Goa University, Goa).

5. Workshop on Data Analysis of Neutron Scattering (Elastic and Inelastic) and Users Meeting, (12-16 June 2023), jointly organized by Jawaharlal Nehru Centre for Advanced Scientific Research (JNCASR) and Rutherford Appleton Laboratory (RAL) at JNCASR, Bangalore.

6. Poster presentation on "Mn-substituted Fe_2TiSn: A wandering axis ferromagnet." **Kulbhushan Mishra**, P. A. Bhobe, International Conference on Magnetism Materials and Applications, (December 2023) (organized by Magnetic Society of India).

7. Poster presentation on "Anomalous magnetoresistance, metamagnetic transition and magnetoelastic coupling in metallic canted antiferromagnet" **Kulbhushan Mishra**, Elaine T. Dias, Rajeev Joshi, A. D. Fortes, Christopher M. Howard, Rajeev Rawat, and P.A. Bhobe, National Conference on Electronic Structure (November 2024) (organized at SMR University AP).

Contents

List of Figures

List of Tables

.

Chapter 1

Introduction

1.1 General Aspects

We rely on various natural and synthetic solid materials in our daily lives.
In recent years, the focus has increasingly shifted toward developing smart
materials—those that can dynamically respond to external stimuli by al-
tering their physical properties. These materials are gaining prominence
across diverse fields such as energy conversion, energy harvesting, biomed-
ical applications, and spintronics. Within this context, certain material
families like oxides, two-dimensional ($2D$) layered compounds, Kagome
lattices, and Heusler alloys have emerged as particularly versatile and mul-
tifunctional.

Among them, intermetallic Heusler alloys stand out as a remark-
able class of materials that have captivated scientific interest since their
serendipitous discovery in 1903, when Fritz Heusler observed long-range
ferromagnetic (FM) ordering in Cu_2MnAl—an alloy composed entirely of
non-magnetic elements [1]. This unexpected behavior sparked ongoing ex-
ploration into the rich physics of Heusler systems.

Heusler alloys are known for their highly tunable properties, which
include magnetism and high spin polarization [2], heavy fermion behavior
[3], superconductivity, spin density wave ordering [4], first-order magneto-

structural phase transitions [5], magnetocaloric effects [6], thermoelectricity [7], the Nernst effect [8], and even topological insulating phases [9]. This extraordinary range of functionalities makes Heusler alloys ideal candidates for advanced applications in spintronics, quantum technologies, and energy-efficient devices.

Critically, the physical properties of Heusler alloys are intricately linked to their crystal structure, which offers remarkable compositional flexibility by accommodating a wide range of elements from the periodic table. This structural adaptability positions Heusler alloys at the forefront of both fundamental research and next-generation technological applications.

One of the key factors influencing the performance of Heusler alloys is antisite disorder, where atoms swap Wyckoff positions, disrupting the ideal crystal arrangement. These disorders can significantly influence the electronic structure and magnetic interactions within the alloy, leading to deviations from expected behavior, such as changes in electrical transport, magnetoresistance, spin dynamics, or even the suppression of desirable phases like half-metallic ferromagnetism. Understanding the interplay between the crystal structure and the material properties, especially the impact of antisite disorder, is crucial for optimizing these alloys for specific applications.

1.1.1 Origin of magnetism in Huesler alloys

One of the most intriguing discoveries in the early study of Heusler alloys was the emergence of ferromagnetism in Cu_2MnAl after appropriate heat treatment, despite the alloy being composed solely of paramagnetic and diamagnetic elements. This unexpected behavior was initially attributed to forming solid solutions of the type $(CuMn)_3Al$, allowing variation in the Cu and Mn content. Early investigations primarily focused on tuning the Cu-to-Mn ratio, and the crystal structure of these alloys was analyzed using X-ray sources such as copper, molybdenum, and chromium. However,

Figure 1.1: Periodic table showing typical X (orange color), Y (sky blue color), and Z (green color) elements in Heusler compounds.

these studies failed to establish a clear relationship between the magnetic properties and the underlying crystal structure. Elis Persson later demonstrated that the ferromagnetic phase corresponded specifically to the stoichiometric composition Cu_2MnAl, which crystallizes in a body-centered cubic (BCC) structure [10]. Continuing this work, Persson synthesized a series of $(CuMn)_3Al$ alloys subjected to various heat treatments and found that ferromagnetism emerged only when the Mn concentration reached 19 atomic percent, sufficient to form an ordered face-centered cubic (FCC) Mn sublattice. To further probe the role of structure and composition in the emergence of ferromagnetism, a $Cu_{2.2}Mn_{0.65}Al$ alloy was prepared and subjected to two distinct thermal treatments: (i) annealing at 500°C followed by slow cooling, and (ii) annealing at 800°C followed by rapid quenching in water. The first treatment led to the formation of a δ-Cu_9Al_4-type structure, which was non-magnetic, whereas the second produced a BCC structure with an FCC superlattice that exhibited strong ferromagnetism. These results clearly indicate that the magnetic behavior of Heusler alloys is uniquely tied to their crystal structure [11].

The crystal structure of Heusler alloys is most accurately described

3

using four interpenetrating face-centered cubic (FCC) sublattices labeled A, B, C, and D, which are located at the positions (0, 0, 0), (0.25, 0.25, 0.25), (0.5, 0.5, 0.5), and (0.75, 0.75, 0.75), respectively. Typically, an ordered Heusler alloy with the formula X_2YZ crystallizes in the cubic space group Fm$\bar{3}$m (space group no. 225), and this structure is known as the Cu_2MnAl-type or the L2$_1$-Strukturbericht type. In this structure, the X atoms occupy the B and D sites (Wyckoff position $8c$), while the Y and Z atoms sit at the C ($4b$) and A ($4a$) positions, respectively.

Besides this commonly observed structure, Heusler alloys are further classified into three additional types:

- Inverse Heusler alloys: These appear when the atomic number of Y is greater than that of X. They crystallize in the Hg_2CuTi-type structure with space group F$\bar{4}$3m (space group no. 216). In this structure, X atoms occupy the (0.5, 0.5, 0.5) and (0.75, 0.75, 0.75) sites, while Y and Z atoms are at (0.25, 0.25, 0.25) and (0, 0, 0), respectively.

- Quaternary Heusler alloys: These have two different X elements and are represented by the formula XX′YZ. They crystallize in a cubic structure similar to that of LiMgPdSb.

- Half-Heusler alloys: With a general formula of XYZ, they crystallize in a non-centrosymmetric cubic structure with space group F$\bar{4}$3m. In this structure, the X, Y, and Z atoms are located at (0.25, 0.25, 0.25), (0.5, 0.5, 0.5), and (0, 0, 0), respectively, forming three interpenetrating FCC sublattices.

1.1.2 Identification of disorder in Heusler alloys:

In the generalized Heusler structure described above, nonzero Bragg reflections occur only when all the Miller indices (hkl) of the scattering planes are either all even or all odd. The intensities of these reflections are determined by the square of the structure factor, F, which for the three types

of reflections is given by,

$$F(111) = 4|f_X - f_Y| \tag{1.1}$$

$$F(200) = 4|2f_X - (f_Y + f_Z)| \tag{1.2}$$

$$F(220) = 4|2f_X + (f_Y + f_Z)| \tag{1.3}$$

where f_X, f_Y, and f_Z represents the scattering factor for elements X, Y and Z. F(111) and F(200) contain difference of scattering term and hence correspond to the order-dependent superlattice reflections, whereas F(220) is the sum of the scattering factors and is independent of the order, known as the principal reflection [12].

1.1.3 Electronic properties of Heusler alloys

The electronic properties of Heusler alloys play a central role in their diverse applications in cutting-edge technologies such as spintronics, thermoelectric devices, and magnetic storage. These materials exhibit various electronic behaviors, including metallic, semiconducting, semimetallic, half-metallic, and the recently discovered spin gapless semiconductor (SGS) state. Some Heusler compounds have also emerged as promising topological materials, hosting nontrivial electronic states such as Weyl and Dirac nodes. These topological features arise from the strong interplay between spin-orbit coupling and the material's crystalline symmetry.

In general, the electronic and magnetic ground states of Heusler alloys can be understood through the Slater–Pauling (SP) rule, which links the total magnetic moment per formula unit (M_t) to the total number of valence electrons (Z_t) [13]. For full-Heusler compounds, the relationship is typically given by $M_t = Z_t - 24$. When $Z_t = 24$, the compound is non-magnetic and displays semiconducting-like resistivity with a finite gap in the density of states (DOS).

1.1.3.1 Half-metallicity

In half-metallic ferromagnetic (HMF) Heusler compounds like Co_2MnSi, one spin channel (majority) is metallic while the other (minority) is semi-conducting or insulating, resulting in 100% spin polarization at the Fermi level—an ideal feature for spintronic applications [2]. Many Co_2- and Mn_2-based Heusler alloys have been predicted as HMFs, where the minority spin states are fully occupied, and the majority states determine an integer magnetic moment, consistent with the Slater–Pauling (SP) rule. A notable extension is the fully compensated half-metallic ferrimagnet, proposed by van Leuken and de Groot, which combines 100% spin polarization with zero net magnetization. Besides the Slater–Pauling (SP) rule, the Rhodes-Wohlfarth (RW) ratio serves as an additional indicator of half-metallic ferromagnetism (HMF) [14, 15]. The RW ratio is defined as p_c/p_s, where p_c is the effective paramagnetic moment per atom obtained from Curie-Weiss fitting, and p_s is the saturation magnetic moment at 0 K. This ratio helps distinguish the nature of magnetism: it is close to 1 for localized moment ferromagnets and greater than 1 for itinerant ferromagnets. Interestingly, for HMFs, the RW ratio is typically much less than 1. This unusual behavior is attributed to (i) antiferromagnetic exchange interactions between localized moments and spin-polarized itinerant holes, which lower the Curie constant and thus reduce p_c, and (ii) modifications in the electronic structure of HMFs in the paramagnetic state [16].

1.1.3.2 Spin-gapless semiconductor (SGS)

Spin gapless semiconductors (SGS), first identified in Heusler compounds like Mn_2CoAl, are an emerging material ideal for spintronic applications. Unlike conventional semiconductors or half-metals, SGSs have a finite bandgap in one spin channel and a nearly zero gap in the other, enabling tunable spin-polarized transport. Their key advantages include a high Curie temperature, low energy required for carrier excitation, and the presence of both electrons and holes with 100% spin polarization. Char-

acteristic signatures of SGS materials are nearly temperature-independent conductivity (very low temperature coefficient of resistance), negligible Seebeck coefficient, minimal variation in carrier concentration with temperature, linear magnetoresistance at low temperatures, and low anomalous Hall conductivity (typically a few hundred S/cm) [17].

1.1.3.3 Topological semimetals

Topological semimetals, characterized by vanishing band gaps and topologically protected surface states, have drawn significant attention for their unusual electronic behavior. Key examples include Weyl, Dirac, nodal line, nodal surface, and multi-fold degenerate semimetals—each holding strong promise for future spintronic technologies. Several Heusler compounds have recently emerged as topological semimetals, hosting Weyl or Dirac nodes. These features give rise to intriguing properties such as the anomalous Hall effect (AHE), large magnetoresistance, and unconventional magnetotransport behavior [8, 18].

1.2 Magnetic ordering in Heusler alloys

Early studies highlighted the critical role of chemical structure in determining the magnetic properties of Heusler alloys, with Mn believed to be the primary carrier of the magnetic moment. This assumption was first confirmed experimentally by Felcher et al. (1963) through neutron diffraction measurements on Cu_2MnAl [19]. By applying a strong magnetic field to distinguish between magnetic and nuclear scattering, they demonstrated that the compound was highly chemically ordered and that the entire magnetic moment could be attributed to the Mn atoms. Subsequent investigations have supported this finding, showing that in most Mn-based Heusler alloys, the magnetic moment is localized at the Mn site. An exception is observed in Co-containing alloys, where the magnetic moment is shared between Mn and Co atoms [20].

The interaction between neighboring magnetic moments in ferromagnets was first introduced by Weiss through the molecular field theory, where the influence of surrounding atoms was modeled as an internal field proportional to the overall magnetization. This framework assumes that magnetic moments are localized and interact via direct exchange. However, direct exchange requires significant overlap of $3d$ wavefunctions, which is unlikely in Heusler alloys due to the large interatomic distances.

In chemically ordered Heusler compounds (X_2YZ), Mn atoms occupy the Y-sublattice and are surrounded by eight X and six Z atoms. The closest Mn–Mn interactions occur only at the third-nearest neighbor shell, with typical separations of 2.6, 3.0, and 4.2 $\mathring{A}$ for the first, second, and third neighbors, respectively, distances too large for effective direct exchange. Unlike the localized model, the collective electron theory considers $3d$ and $4s$ electrons as delocalized and itinerant. While it has been useful in describing ferromagnetism in transition metals, its applicability to Heusler alloys is limited due to its lack of sensitivity to elemental distinctions.

A more suitable framework for Heusler alloys is the s–d exchange interaction described by the Ruderman–Kittel–Kasuya–Yosida (RKKY) theory. Here, conduction electrons mediate long-range, oscillatory exchange interactions between localized moments. The sign and strength of these interactions—whether ferromagnetic or antiferromagnetic—depend on the conduction electron density and the separation between the magnetic moments. Consequently, in Heusler alloys, the magnetic coupling between Mn atoms is mediated by the itinerant electrons of the X and Z atoms, making their electronic structure crucial in determining the nature and strength of magnetic interactions [12, 21, 22].

1.2.1 Effect of disorder on the magnetic properties of Heusler alloys

Disorder in Heusler alloys can significantly impact their magnetic properties by affecting the local magnetic interactions. Additionally, it can lead to

the formation of regions with different magnetic properties within the same materials. Such clusters give rise to intriguing magnetic states, including superparamagnetism, Griffiths' phase, spin glass, and correlated spin glass.

1.2.1.1 Superparamagnetism

Superparamagnetism (SPM) arises in nano-scale ferromagnetic particles, small enough to form single magnetic domains, where the energy cost of domain wall formation exceeds the gain from reducing demagnetizing energy. These particles, with a net magnetic moment comprising all atomic moments, are typically well-separated, minimizing interparticle interactions. Although their magnetization prefers specific directions due to anisotropy, thermal energy causes spontaneous flipping. When $k_B T \gg KV$ (with K as the anisotropy constant and V the particle volume), the system behaves like a paramagnet. The relaxation time (τ) for magnetization reversal is given by $\tau = \tau_0 \exp(KV/k_B T)$, where $\tau_0 \sim 10^{-9}$ s. As temperature decreases, magnetization fluctuations slow, and depending on the measurement timescale (t_m), two regimes emerge: (i) if $t_m \gg \tau$, the system appears blocked below a characteristic blocking temperature (T_B); (ii) if $t_m \ll \tau$, the net moment remains zero in zero field, indicating the SPM state. Under an applied field, moments align along the field, and magnetization increases with decreasing temperature in temperature-dependent magnetization (M(T)) measurements [23]. Isothermal M(H) behavior varies with temperature and can be described using the following equations;

(i) $T_B < T < KV/10 \ k_B$

$$M(H) = nm^* tanh(\mu_0 Hm/k_B T) \qquad (1.4)$$

(ii) $T > KV/k_B$

$$M(H) = nmL(\mu_0 Hm/k_B T) \qquad (1.5)$$

where n is the density of nanoparticles, m is the magnetic moment of the nanoparticle, and L(x) is the Langevin function.

1.2.1.2 Griffiths' phase

Griffiths' phase (GP) refers to the presence of short-range ferromagnetic (FM) clusters that persist above the Curie temperature (T_C). Originally proposed by Griffiths in the context of a randomly diluted Ising ferromagnet, where certain lattice sites are either vacant or occupied by nonmagnetic ions, GP has since been observed in real materials. Experimentally, it is now well established that static or quenched disorder plays a crucial role in the formation of GP. In such disordered systems, isolated regions with strong FM correlations can form, producing finite-size FM clusters embedded in a paramagnetic matrix. As a result, although spontaneous long-range magnetization is absent, short-range FM interactions lead to magnetic anomalies above T_C. These anomalies become significant in the temperature window between T_C and a higher characteristic temperature known as the Griffiths temperature (T_G).

The key signature of GP is a downward deviation in the inverse susceptibility (χ^{-1}) versus temperature plot, deviating from Curie-Weiss behavior. This anomaly weakens under higher magnetic fields, as the applied field aligns spins outside the clusters, masking the effect. In the GP regime ($T_C < T < T_G$), the susceptibility follows a power-law behavior: $\chi^{-1} \propto (T - T_C)^{1-\lambda}$, where $0 < \lambda < 1$. In Heusler alloys exhibiting GP, the exponent λ typically ranges between 0.89 and 0.97 [24–27].

1.2.1.3 Spin glass

Spin glass was originally introduced to describe certain magnetic alloys exhibiting non-periodic "freezing" of spin orientations. A spin glass is a disordered magnetic system where the spins undergo a collective but random freezing below a characteristic temperature, T_f, without forming conventional long-range magnetic order. At T_f, the system becomes trapped in one of many metastable ground states, leading to an irreversible, frozen spin configuration. Two key features underpin spin glass behavior are: quenched disorder and magnetic frustration. In Heusler alloys, the RKKY-type ex-

change interaction, whose sign oscillates with distance, combined with a random distribution of atomic sites, leads to competing ferromagnetic and antiferromagnetic interactions, causing frustration. While spin glasses may appear similar to superparamagnets, they differ fundamentally: (i) spin-spin interactions are negligible in superparamagnets but essential in spin glasses, and (ii) spin glasses exhibit a cooperative phase transition at T_f, whereas superparamagnets undergo a gradual blocking of non-interacting magnetic moments [23, 28–30].

1.2.1.4 Ferromagnetically correlated clusters

A unique magnetic state can emerge in systems with weak random magnetocrystalline anisotropy, evidenced by the irreversible behavior of ZFC and FC M(T) curves at low temperatures. Spins are spatially disordered in a zero magnetic field, and no net magnetization is present. However, spin-spin correlations persist over a finite length scale ξ, within which local ferromagnetic order exists. Unlike conventional ferromagnets, there are no sharp domain walls; instead, local magnetization directions gradually rotate across the sample. When a weak magnetic field $H < H_s = H^4_r/H^3_{ex}$ (where H_r and H_{ex} are anisotropy and exchange fields, respectively) is applied, the CSG state remains stable. For intermediate fields $H_S < H < H_{ex}$, the system enters a ferromagnet with wandering axis (FWA) state, where spins align roughly along the field but retain a non-collinear structure. In this regime, magnetization increases gradually toward saturation, governed by a characteristic field dependence [31–34]. In this regime, the magnetization approaches saturation as;

$$M(H) = M_s \left[1 - \frac{1}{15} \left(\frac{H_s}{H + H_c} \right)^{\frac{1}{2}} \right] \tag{1.6}$$

For $H \gg H_S$, the correlation length of the spins decreases with increasing field strength, while the tipping angles between spins become completely uncorrelated across the system. In this high-field regime, spins are nearly aligned with the applied field, except for slight deviations caused by random

11

anisotropy, smaller than those observed in the ferromagnet with wandering axis (FWA) state. This state is referred to as a correlated spin glass under strong fields. In such cases, isothermal magnetization gradually approaches saturation as,

$$M(H) = M_s \left[1 - \frac{1}{15} \left(\frac{H_r}{H + H_{ex}} \right)^2 \right] \tag{1.7}$$

1.3 Electrical transport in Heusler alloys

The characteristic feature of a metallic system is the presence of conduction electrons. Consequently, the electrical resistivity, $\rho(T)$, becomes a complex physical quantity, as it is influenced by the electronic structure and various scattering mechanisms that affect electron relaxation. These include scattering from structural defects, phonons, magnons, and electron-electron interactions, all contributing to the temperature dependence of $\rho(T)$.

1.3.1 residual resistivity (ρ_0)

Residual resistivity arises from static imperfections that disrupt the periodicity of the crystal lattice, with structural defects being the most common contributors. This type of scattering dominates at low temperatures and is largely temperature-independent. Its magnitude is determined by the concentration of defects present in the sample. A common way to assess the structural quality or homogeneity of a metallic sample is through the residual resistivity ratio (RRR), defined as ρ_{300K}/ρ_0, where ρ_0 is the resistivity at low temperature. The crystal with a smaller defect concentration, i.e., smaller ρ_0 or higher purity, shows higher RRR and vice versa.

1.3.2 electron-phonon scattering (ρ_{ph}):

Phonons represent propagating lattice distortions and scatter conduction electrons both elastically and inelastically. The phonon contribution to resistivity, ρ_{ph}, is strongly influenced by the Debye temperature (Θ_D), which

sets the energy scale for the highest-energy phonons in a metal. For T $\gg \Theta_D$, electrons are efficiently scattered across the Fermi surface by single phonon events, resulting in a linear temperature dependence of ρ_{ph}. In contrast, at T $\ll \Theta_D$, multiple scattering events are required to randomize the electron's motion, leading to a T^5 dependence of ρ_{ph}.

1.3.3   electron-electron scattering (ρ_{ee}):

The contribution of electron-electron (e–e) interactions to electrical resistivity,ρ_{ee}, originates from Coulomb scattering among conduction electrons. This phenomenon was first explored in the seminal works of Landau–Pomeranchuk [35] and Baber [36], who demonstrated that e–e scattering yields a resistivity term proportional to $A_{ee} T^2$, where A_{ee} is a material-dependent constant. In ultra-clean metallic systems, this T^2 dependence contributes to $\rho(T)$ at low temperatures.

1.3.4   electron-magnon scattering (ρ_{mag}):

In the paramagnetic region, the random orientation of magnetic moments enhances the scattering of conduction electrons, resulting in higher resistivity. Upon magnetic ordering, this spin disorder is suppressed due to the alignment of magnetic moments, thereby reducing electron scattering and lowering resistivity. Below the magnetic ordering temperature, T_C, quantized spin excitations known as magnons emerge. Electron-magnon scattering then contributes to the temperature dependence of resistivity, $\rho(T)$, particularly at low temperatures. This scattering can occur via two main mechanisms: (i) one-magnon scattering, which follows a T^2 dependence, and (ii) two-magnon scattering, which exhibits a $T^{9/2}$ dependence at low temperatures and $T^{7/2}$ at higher temperatures.

Thus, the electrical resistivity of the metallic magnetic Heusler alloy is expressed as the combination of all these processes,

$$\rho(T) = \rho_0 + \rho_{ee} + \rho_{ph} + \rho_{mag} \tag{1.8}$$

1.3.5 Effect of disorder and origin of negative temperature coefficient of resistance

Electrons move ballistically in a perfectly periodic potential, but real crystals have imperfections and lattice vibrations that cause scattering. At finite temperatures, these vibrations and static disorder disrupt periodicity, leading to inelastic scattering from phonons, preventing electrons from retaining their phase over long distances. However, at very low temperatures, elastic scattering dominates, allowing electrons to maintain phase coherence over larger distances. This phase coherence produces coherent interference phenomena, leading to observable macroscopic effects.

Disorder greatly affects the electrical resistivity and overall properties of Heusler alloys. In these alloys, disorder plays a crucial role in determining electrical resistivity. While electron-phonon and electron-magnon interactions typically lead to a positive temperature coefficient of resistivity (TCR), atomic antisite disorder enhances electron-electron interactions and weak localization, resulting in a negative TCR at low temperatures. Additionally, magnetic disorder can give rise to the Kondo effect. The competition between these mechanisms often leads to a resistivity minimum, highlighting the complex impact of disorder on the transport properties of these materials.

1.3.5.1 Weak localization (WL)

Weak localization (WL) arises from coherent backscattering of electrons due to disorder. It can be understood by considering the quantum interference between two time-reversed paths that return an electron to its origin after multiple scatterings. If path–1 and its time-reversed counterpart, path–2, have amplitudes $A1$ and $A2$, then under time-reversal symmetry, $A1 = A2 = A$. The resulting constructive interference enhances the probability of return by a factor of four compared to classical expectations. This increased backscattering leads to a quantum correction in resistivity, with

the WL contribution following a $T^{1/2}$ dependence at low temperatures for three three-dimensional systems [37].

1.3.5.2 Kondo spin-flip scattering

Magnetic impurities embedded in a metallic lattice can lead to significant electron scattering via the Kondo effect. In this phenomenon, an electron from the Fermi sea may tunnel into the impurity state, while another electron tunnels back into the sea within a time interval constrained by the uncertainty principle. This typically involves spin exchange, modifying the system's energy spectrum, and forming a sharp Kondo resonance near the Fermi level. The result is enhanced electron scattering and increased resistivity, which varies logarithmically with temperature, i.e., $\rho(T) \propto lnT$ at low temperatures [38].

Notably, such logarithmic temperature dependence can also arise from other mechanisms like two-level system (TLS) tunneling [39] or scattering from spin fluctuations [40]. However, if the resistivity minimum remains unaffected by a strong applied magnetic field, the Kondo effect can be ruled out as the dominant mechanism [41, 42].

1.3.5.3 Electron-Electron Interaction (EEI)

In disordered metals, two interacting electrons with similar energies $\varepsilon_1 = \varepsilon_2 = \varepsilon$ can encounter each other multiple times during a time interval on the order of $\hbar/\varepsilon$. Due to diffusive motion, the interaction processes occurring in this interval interfere, summing their probability amplitudes. This interference leads to an enhancement of electron-electron interactions [37, 43]. EEI contribution to resistivity in three-dimensional (3D) disordered systems is given by $\rho_{EEI}(T) = \rho_{EEI}T^{1/2}$.

The scattering mechanisms discussed above account for the anomalous behavior of resistivity at very low temperatures, particularly in metallic systems with dilute disorder. However, a negative temperature coefficient of resistivity (TCR) can persist in highly disordered alloys even at

elevated temperatures. This negative TCR is not only attributed to strong structural disorder but can also arise from charge-carrier localization. Such localization typically occurs in systems exhibiting a deep energy gap or a pseudogap near the Fermi level, as is often seen in semimetals [44].

One of the key frameworks for understanding electrical transport in disordered metallic systems is the generalized Faber-Ziman diffraction theory, initially developed for liquid metals [45] and later extended to amorphous and crystalline solids by Cote and Meisel [46, 47]. In this model, the resistivity of the highly resistive metals can be expressed as

$$\rho(T) = exp(-2\overline{W(T)})(\rho_0 + \Delta_{ep}) \tag{1.9}$$

where,

$$\overline{W(T)} = \frac{3 < \hbar^2 > T^2}{2Mk_B\Theta^3} \int_0^{\Theta/T} (\frac{1}{e^z - 1} + \frac{1}{z})\, dz \tag{1.10}$$

Here, ρ_0 is the residual resistivity due to the scattering of electrons with static defects, and Δ_{ep} is the inelastic electron-phonon interaction term, $\overline{W(T)}$ is an average Debye-Waller exponent [48, 49], $\hbar$ is reduced Planck constant, k_B stands for Boltzmann constant, Θ corresponds to the Debye temperature, k is the scattering wave vector of conduction electrons, and M is the molar mass. The bracket $< >$ denotes averaging over the scattering vectors k at the Fermi energy. For disordered metals with a high value of ρ_0, Δ_{ep} is negligible compared to ρ_0. Since $2\overline{W(T)}$ increases with increasing T, equation (1.9) will lead to a negative TCR.

1.3.5.4 Hopping mechanism

The semiconductor-like behavior of $\rho(T)$ may also occur due to the localized impurity state near the Fermi level. At non-zero temperatures, localized electrons may contribute to the electron transport due to the hopping of charge carriers from one localized state to another. Usually, hopping conductivity in crystalline semiconductors dominates at low temperatures when free carriers with high mobility are frozen out. In many amorphous and insulating materials, where the concentration of free carriers is negligible, while the density of defects, impurities, and other trapping centers for

electrons is very high, hopping is the main conductivity mechanism. The important postulate of the hopping mechanism is that two states with equal energies are located at a finite distance from one another, and hopping is accompanied by the emission or absorption of phonons [50].

(1) The simplest form of hopping mechanism is presented by transmission between nearest neighbors, known as *nearest-neighbor hopping*, where the resistivity is described as $\rho = \rho_0 T \exp(E_a/2k_B T)$, where E_a is activation energy, k_B is Boltzmann constant, and T is absolute temperature. The condition necessary for the realization of nearest-neighbor hopping is the existence of a large number of pairs of close neighbors, with one of them being free.

(2) With the decrease in temperature, the number of empty sites among the nearest neighbors is too small, and hopping to the nearest centers freezes out. In this case, the hopping between states with energies closer to the Fermi level will be realized. This leads to a new kind of hopping conductivity called *Variable-Range-Hopping (VRH)*, as proposed by N. F. Mott [51]. In VRH, the resistivity is described as $\rho = \rho_0 \exp(T_0/T)^{1/4}$, where T_0 is characteristics Mott's temperature.

(3) In Mott's–VRH, it was assumed that DOS near the Fermi level is constant. However, due to Coulomb interaction between different charge carriers, electrons localized on states near the Fermi level will be redistributed to reduce the total electron energy. This leads to the formation of a "soft" Coulomb gap at the Fermi level, which leads to the resistivity behavior as $\rho = \rho_0 \exp(T_0/T)^{1/2}$. This hopping mechanism is known as *"Efros–Shklovskii" law* [52].

1.4   Motivation

This thesis studies the magnetic structure and magnetotransport properties of selected Fe-based Heusler alloys. Understanding the interplay between crystallographic order, magnetic interactions, and charge transport

is crucial for fundamental insights and technological enhancement. Here, particular emphasis is given to understanding the magnetic phase transitions, spin ordering, disorder effects, and their influence on phenomena such as magnetoresistance and electronic transport with temperature and applied magnetic field. Using a combination of structural (X-ray and neutron diffraction), magnetic (magnetization, susceptibility), and transport (resistivity, magnetoresistance, heat capacity) measurements, this work aims to reveal how changes in composition and synthesis conditions impact the magnetic structure and transport behavior in these Fe-based Heusler systems. The outcomes contribute to the understanding of spin-dependent transport in complex magnetic materials and provide a foundation for tailoring Heusler alloys for next-generation spintronic devices.

In this thesis, we have studied the magnetism and magnetotransport in Fe-based Heusler alloys, particularly disorder effects, spin-dependent transport, and metamagnetic transitions in Fe-based Heusler alloys, using a combination of powder neutron diffraction, magnetic measurements, and transport property analyses. In particular, we investigated the following full-Heusler alloys;

- Fe_2TiSn and its half-metallic derivatives.
- Al substituted Mn_2FeSi.
- Mn substituted Fe_2TiSn.
- $Mn_{1.7}Fe_{1.3}Si$.

1.5   Organization of thesis

- **Chapter 1:** The first chapter briefly overviews the crystal structure, electronic properties, magnetic ordering, and magneto-transport in Heusler alloys. This chapter also discusses the effect of anti-site disorder on magnetic properties and electrical transport. It also defines the broad objective and structure of this thesis work.
- **Chapter 2:** The second chapter briefly describes various experimen-

tal techniques used to characterize the synthesized samples. The different characterization techniques employed in the present study for structural analysis include X-ray diffraction (XRD, energy dispersive X-ray spectroscopy (EDX), powder neutron diffraction, magnetic and electrical transport measurement, and X-ray absorption fine structure spectroscopy (XAFS). For ab initio calculations, we have used Quantum Espresso and SPR-KKR for density of states and Heisenberg exchange interaction calculations. To analyze the powder X-ray and neutron diffraction data, we have used the Rietveld refinement method as employed in the FullProf software.

- **Chapter 3:** This chapter begins with exploring the amount of anti-site disorder and the effect of secondary annealing on the physical properties of Fe_2TiSn and its Sb and Cr substituted half-metallic compositions, namely $Fe_2TiSn_{0.5}Sb_{0.5}$, and $Fe2Ti_{0.75}Cr_{0.25}Sn$. We have quantified the amount of anti-site disorder in these compositions using temperature-dependent powder neutron diffraction. The presence of anti-site disorder significantly affects these compositions' magnetic and electrical transport properties. Further, we have subjected all the compositions to secondary heat treatment and studied their effects on their electrical resistivity and magnetization, suggesting a noticeable decrease in antisite disorder.

- **Chapter 4:** In this chapter, we have explored the electronic structure, crystal and microstructure, and magnetic properties of Mn_2FeSi, using density of states calculations, X-ray diffraction, and temperature and field-dependent magnetization measurements. We have also elucidated the impact of atom swapping among different constituents of Mn_2FeSi on its magnetic and electronic properties. Furthermore, we synthesized Mn_2FeSi in a pure cubic inverse Heusler phase by substituting 10 % Al at the Si site and subsequently examined its magnetic properties in detail. Our magnetic study unveiled an anti-ferromagnetic (AFM) ground state at temperatures below 50 K and a Griffiths-like phase within 184–260 K in a cubic Heusler compound.

These findings contribute to a deeper understanding of the electronic properties of Mn_2FeSi and highlight the intriguing complexities arising from disorder and its profound influence on the magnetic behavior of Heusler alloys.

- **Chapter 5:** In this chapter, we report the detailed investigation of the structural, magnetic, and transport properties of Mn-substituted Fe_2TiSn compositions. X-ray diffraction (XRD) results show the formation of an ordered $L2_1$ structure with reduced antisite disorder. The low temperature upturn in the electrical resistivity is due to the Kondo-like spin scattering. This interpretation is further supported by specific heat measurements. The temperature and field-dependent magnetization measurements indicate the presence of anisotropy in the system due to the strong local magnetic moment of Mn atoms. Additionally, EXAFS measurements indicate that the magnetocrystalline anisotropy in the cubic Heusler compound primarily originates from local lattice distortions. We have also performed the electronic structure calculations to better understand the ground state properties.

- **Chapter 6:** In this chapter, we comprehensively investigated the magnetotransport, magnetic, and structural properties of $Mn_{1.7}Fe_{1.3}Si$. Temperature-dependent resistivity measurement confirms the metallic nature of the prepared composition. The isothermal field-dependent magnetization and magnetotransport data reveal a field-induced metamagnetic transition at low temperatures. Additionally, temperature-dependent magnetization shows the spin reorientation transition (SRT) between 65 K and 55 K. Below 55 K, temperature-dependent neutron powder diffraction (NPD) analysis confirms the presence of canted antiferromagnetic ordering. The variation of unit cell volume with temperature, extracted from the refinement of the NPD data, shows anomalous slope change around magnetic transitions, hinting at strong magnetoelastic coupling in $Mn_{1.7}Fe_{1.3}Si$. The H-T phase diagram, constructed from magnetore-

sistance and magnetization curves, reveals the presence of magnetic phase coexistence at low temperatures.

- **Chapter 7:** The last chapter of the thesis includes the concluding remarks and future prospects of the studied compositions.

.

Chapter 2

Experimental and Theoretical Methods

2.1 Overview

This chapter provides a comprehensive outline of the experimental and theoretical methodologies employed in this work to synthesize and characterize the materials, along with the computational approaches used to support the experimental findings. We discuss the steps involving the sample preparation techniques and the instruments used for the same. Next, the techniques used to confirm elemental stoichiometry and structural characterization, such as FE-SEM, EDX, X-ray, and neutron diffraction, are discussed. Description of the magnetic properties and magneto-transport measurements is also discussed. Next, we discuss the principles and data analysis techniques for Extended X-ray Absorption Fine Structure (EXAFS) used to study the local atomic structure of the materials. As the chapter proceeds, we briefly describe computational approaches used to support experimental findings.

2.2 Experimental Methods

2.2.1 Sample preparation

The polycrystalline beads of Heusler composition discussed in this thesis were prepared by arc melting the 99.99% pure elements in an inert argon gas atmosphere. A water/air-cooled cylindrical copper (Cu) hearth serves as an anode as well as crucible for melting the samples in an arc furnace, while a water-cooled tungsten tip serves as the cathode. An argon (Ar) atmosphere is used to create an electric arc between the copper hearth and the tungsten electrode, which melts the components. The four main components of the tri-arc furnace are a power supply, a water chiller to cool the system while melting, a vacuum unit to remove air from the chamber, and a chamber where the melting occurs, as shown in 2.1. The electrode is connected to the high-range power source. First, desired high-purity (99.99%) starting components were obtained, weighed according to the stoichiometry, and placed on the Cu hearth. The air inside the chamber is evacuated by the rotary pump, followed by the flushing of Ar gas through the chamber. This process is repeated 6-8 times to ensure a completely inert atmosphere inside the chamber. The constituent elements were melted using an arc generated by briefly touching the tungsten tip (cathode) to the copper hearth (anode) in an inert argon atmosphere. During the melting process, the hearth and the tungsten electrode are continuously cooled by circulating chilled water to prevent overheating. To ensure sample homogeneity and minimize weight loss, the melting process is typically repeated 3–4 times. The arc-melted samples are vacuum-sealed in an evacuated quartz tube under high vacuum (less than 10^{-5} mbar) and annealed at different protocols depending on the samples.

A low-speed diamond saw was used to cut the samples precisely into appropriate dimensions for various characterization techniques. A portion of the bead was ground into a fine powder using an agate mortar and pestle and subsequently sieved through a 0.09 mm mesh. This finely

Figure 2.1: (a) Labeled image of the tri-arc furnace, and (b) the top image of the melting chamber.

ground powder was utilized for diffraction studies, including X-ray and neutron diffraction, as well as Extended X-ray Absorption Fine Structure (EXAFS) analysis. The remaining pieces were carefully cut to meet the specific transport and magnetic characterization experiment requirements.

2.2.2 Field Emission Scanning Electron Microscopy

The field emission scanning electron microscope (FE-SEM) images a sample's surface by raster scanning over it with a high-energy electron beam. The electrons interact with the atoms comprising the samples to produce information about surface topography and compositions from nanometer to micrometer resolution. In FE-SEM, primary electrons are generated from a field emission source and accelerated in a high electrical field gradient. Electromagnetic lenses focus and deflect these primary electrons in a high vacuum column to produce a narrow beam. As these primary electrons penetrate the surface of the sample, various signals are generated. There are mainly low-energy secondary electrons (SE) (energies of < 50 eV), high-energy backscattered electrons (BSE) (energies of > 50 eV), and characteristic X-rays. These signals are collected using detectors to form an image or to analyze the samples' surface. Secondary and back-scattered electrons, which are of most interest, are conventionally separated according to their energies as they are generated by different mechanisms. The
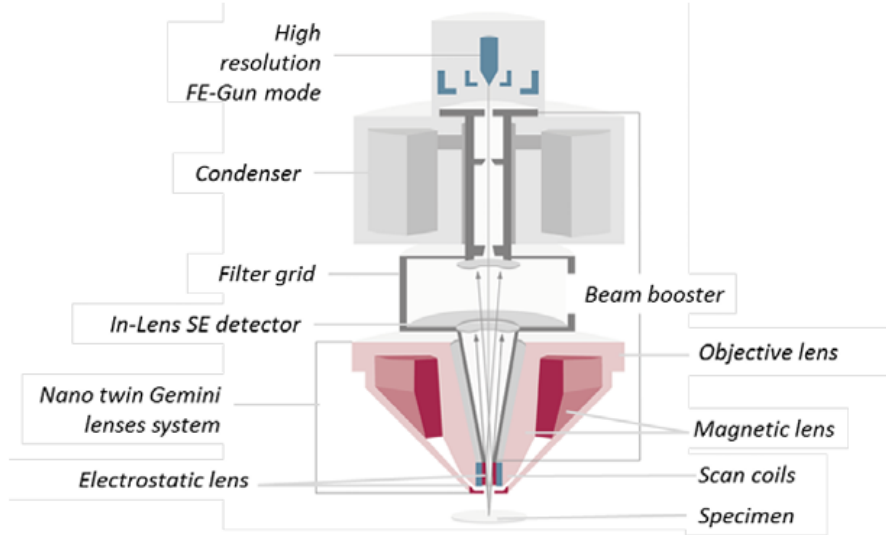
Figure 2.2: Schematic diagram of FE-SEM.

back-scattered electrons (BSE) can be used to differentiate various phases in a sample based on compositional contrast. BSE detectors collect electrons scattered back from the sample, and the signal intensity depends on the atomic number of the elements present. Regions with heavier elements appear brighter, while those with lighter elements appear darker. This compositional contrast enables the identification of different phases within a sample, making BSE microscopy particularly useful for studying multiphase materials, detecting inclusions, and assessing chemical homogeneity.

In this thesis, the FE-SEM micrograph and BSE images were taken using FE-SEM, JEOL, and JSM-7610 F. Before the measurements, the sample surface was gently polished using emery polishing papers of different grits and polishing cloth until it became mirror-finished and was mounted into the FE-SEM sample holder with carbon tape.

2.2.3 Energy Dispersive X-ray Spectroscopy

Energy dispersive spectroscopy is abbreviated as EDS, EDX, or sometimes it is termed as energy dispersive X-ray analysis (EDXA). It's an investigative method that is widely used in elemental or chemical characterization
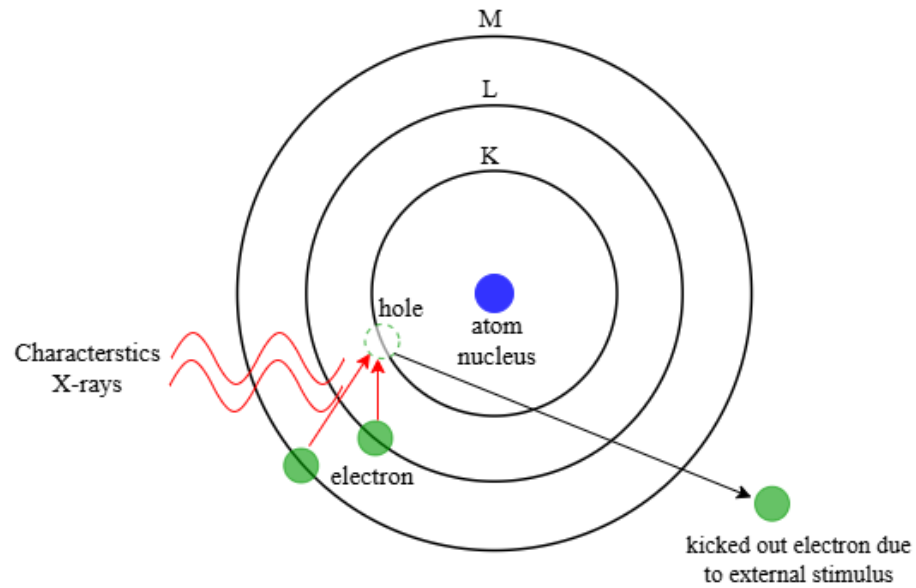
Figure 2.3: A schematic showing the mechanism of characteristic X-ray generation.

of the sample. EDS is actually built within the FE-SEM setup. EDS works by measuring the energy and intensity of the X-rays that are emitted when they are exposed to the electron beam. During EDS analysis, a high-energy electron beam interacts with atoms of the sample and generates characteristic X-rays. A detector converts X-rays into voltage signals, which feed a pulse processor to measure signals and pass them to a data analyzer for display and investigation. These characteristics of X-rays are unique for each element, and detecting and measuring these X-rays is used to determine which elements are present in the sample and at what quantity. This principle is depicted in Fig.2.3

2.2.3.1 Diffraction techniques

Crystal structure plays a fundamental role in determining the physical properties of materials, influencing everything from the hardness of metals to the strength of magnets and the behavior of water and ice. The properties of elements can vary significantly depending on how atoms are arranged or combined with other elements. A crystal structure is defined as the combination of a lattice—a periodic array of points in three-dimensional

27
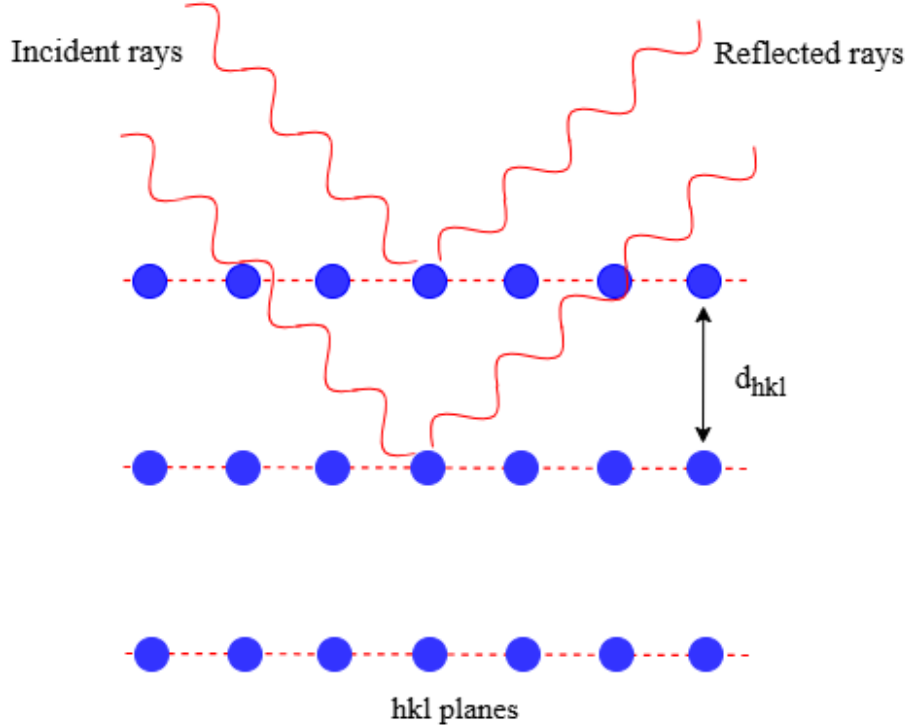
Figure 2.4: Schematic showing the visualization for Bragg's law.

space—and a motif, which consists of atoms associated with each lattice point. Based on symmetry and atomic arrangement, crystal structures can be broadly classified into different types. Diffraction techniques serve as one of the most fundamental methods for identifying and analyzing crystal structures. They are essential in condensed matter physics, offering key insights into both structural and magnetic properties. When a wave interacts with a material, it produces a diffraction pattern characterized by peak positions and intensities. The peak positions reveal information about the lattice, while the peak intensities provide details about the atomic motif. By analyzing diffraction patterns, researchers can determine atomic arrangements, lattice parameters, crystallographic phase transitions, and even magnetic structures. Such insights are crucial for developing materials with tailored properties for applications in spintronics, thermoelectrics, and magneto-transport. This thesis employs two primary diffraction techniques: X-ray diffraction (XRD) and neutron diffraction, each offering unique advantages for structural and magnetic studies.

X-ray diffraction: X-ray diffraction (XRD) is a powerful technique

to determine the crystal structure, phase composition, and lattice parameters of materials. It is based on the constructive interference of X-rays scattered by the periodic atomic planes in a crystalline material, described by Bragg's law: $2dsin\theta = n\lambda$. This law of diffraction relates crystal lattice parameters d (spacing between the atomic planes of the solid) and wavelength of incident radiation (λ) with the diffraction angles (θ), and n is the order of diffraction. Fig.2.4 shows the schematic of the Bragg diffraction condition. In XRD measurement, a monochromatic X-ray beam is directed at the fine powder of the sample, and a detector collects the diffracted X-rays as a function of 2θ. The resulting diffraction pattern provides information about the crystal structure, phase purity, and degree of crystallinity. The peak positions correspond to specific atomic arrangements, while peak intensities reflect the atomic occupancy and structure factor. Broadening of peaks can indicate strain, defects, or small crystallite size. In this thesis, the room temperature XRD is performed with Cu K$_\alpha$ source ($\lambda = 1.54$ Å) using two different diffractometers, Empyrean, Malvern Panalytical X-ray diffractometer, and Bruker D8 Advance diffractometer.

Neutron diffraction: The concept that neutrons would also diffract like X-rays was first proposed by Dana Mitchell and Philip Powers. They proposed that neutrons have a wave-like nature, which is explained by the de Broglie equation, $\lambda = h/mv$, where λ is the wavelength of the source usually measured in Å, h is Planck's constant, v is the velocity of the neutron, and finally m represents the mass of the neutron. Neutrons are scattered by the nucleus of the atoms, unlike X-rays, which are scattered by the electron cloud of the atoms. This leads to more accurate identification of the crystal structure and inherent disorder/defect when elements of similar atomic numbers are present in the composition. One of the key advantages of neutron diffraction over XRD is its ability to probe magnetic structures. Since neutrons possess an intrinsic spin, they interact with unpaired electron spins in a material, allowing direct observation of magnetic ordering, spin arrangements, and magnetic phase transitions. This makes neutron diffraction indispensable for studying complex magnetic materials,

including Heusler alloys.

Based on the energy (E) of neutrons, they are classified into four categories: (i) thermal ($E = 25$ meV), (ii) epithermal ($E = 0.25$–10 eV), (iii) fast ($E = 10$ keV–20 MeV) and (iv) cold ($E = 10$–25 meV). Of particular interest in condensed matter research are neutrons with wavelengths comparable to the radii of atoms (~ 1–2×10^{-10} m). These so-called thermal neutrons are strongly diffracted by the ordered arrangements of atoms in crystals. The neutrons produced in the neutron sources (reactors or spallation) are initially fast, but they are slowed down using a moderator, a material that efficiently scatters neutrons without absorbing them. Through multiple elastic collisions with moderator atoms, neutrons reach thermal equilibrium with the medium. H_2O, D_2O, and Graphite are a few examples of moderators that bring neutrons with high energy to the energy range of thermal neutrons.

Data analysis: The diffraction data were analyzed using the Rietveld refinement method, implemented through the FullProf suite [53]. Rietveld refinement is a robust and widely used technique in crystallography for extracting detailed structural information from X-ray and neutron diffraction patterns. The method relies on the least-squares fitting approach, where the observed diffraction profile is compared with a calculated one based on a structural model. Through iterative refinement, key parameters such as lattice constants, atomic positions, site occupancies, thermal displacement factors, and microstructural features (e.g., strain and crystallite size) are optimized. This technique is particularly valuable for investigating complex materials such as Heusler alloys, where features like antisite disorder and intricate magnetic structures critically influence the material's physical properties.

FullProf is a widely adopted program for performing Rietveld refinement, facilitating the analysis of both X-ray and neutron diffraction data. The refinement process in FullProf requires a structured input file known as a .pcr file, which includes all the essential parameters for the

calculation. This file contains essential parameters, including instrumental settings (wavelength, instrumental zero, etc.), lattice parameters (a, b, c, α, β, γ), atomic positions, site occupancies, thermal parameters, and peak profile functions. For magnetic structure refinement, additional details such as the magnetic symmetry and the orientation and magnitude of spin moments must be specified. The refinement iteratively adjusts these parameters to minimize the difference between the observed and calculated diffraction patterns using a least-squares approach. Convergence is achieved when the model accurately reproduces the experimental data while preserving physically meaningful and consistent values for all refined parameters.

The indication of a good fit is measured in terms of the reliability factors (R values) and Goodness of the fit parameter (χ^2). The different R values and χ^2 are given by the following equations:

(a) Weighted profile R–factor (R_{wp})

$$R_{wp} = \left[\frac{\sum_i w_i(y_{i0} - y_{ic})^2}{\sum_i w_i y_{i0}^2} \right]^{1/2} \tag{2.1}$$

(b) Expected R–factor (R_{exp})

$$R_{exp} = \left[\frac{N - P + C}{w_i y_{i0}^2} \right]^{1/2} \tag{2.2}$$

(c) Goodness of fit (χ^2)

$$\chi^2 = \left[\frac{R_{wp}}{R_{exp}} \right]^2 \tag{2.3}$$

here y_{i0} and y_{ic} are the observed and calculated intensities, and $w_i = \frac{1}{y_i}$ is the weighting factor. N is the total number of points used in the refinement, P is the number of refined parameters, and C is the number of constraints. N-P+C is the number of degrees of freedom. The signature of a good fit is to obtain the low value of R_{wp} and χ^2 after the final iteration. The χ^2 value between 1 and 2 is considered to be a good fit.

2.2.4   Magnetic Property Measurement

The magnetic properties of all the compounds discussed in this thesis were characterized using a 'Superconducting Quantum Interference De-
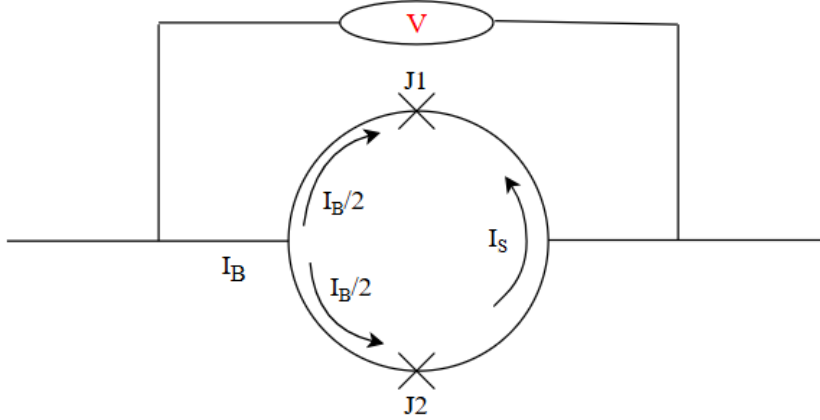
Figure 2.5: Schematic diagram of two Josephson junctions connected in parallel with a voltmeter.

vice' or SQUID-based Magnetic Properties Measurement System (MPMS) by Quantum Design and Physical Property Measurement System configured with a vibrating sample magnetometer (PPMS–VSM).

SQUID magnetometer: A Superconducting Quantum Interference Device (SQUID) operates by combining the principles of flux quantization and Josephson tunneling to detect extremely small magnetic fields. It consists of a superconducting loop with one or more Josephson junctions, allowing it to convert difficult-to-measure magnetic flux into an easily measurable voltage. To understand the workings of a SQUID, consider a scenario when it is biased with a current (I_B) well below its critical current value, as shown in Fig.2.5. The critical current is the maximum current a SQUID can carry without being resistive. When the two junctions in the SQUID are identical, the loop is symmetrical, and there is no magnetic flux present in the loop, the voltage drop across it is zero. Now, if there is a magnetic flux inside the superconducting loop, it will oppose this flux by generating a screening current (T_S) that flows opposite to the bias current. This reduces the net current through the SQUID, leading to a measurable voltage drop across the loop. The induced voltage is directly proportional to the applied magnetic flux, enabling precise detection of minute magnetic fields.
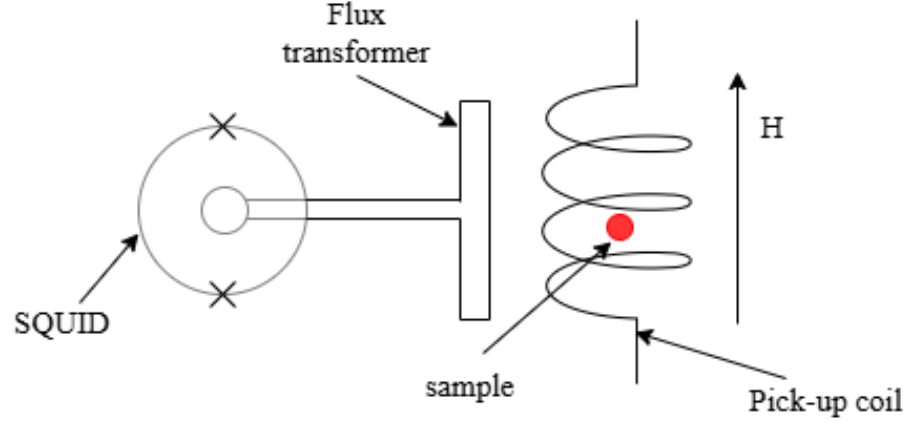
Figure 2.6: Schematic showing the working principle of a SQUID magnetometer.

The schematic in Fig.2.6 illustrates the working principle of a SQUID magnetometer, which consists of a sample insertion rod, pick-up coil, flux transformer, and SQUID sensor. As the sample—acting as a tiny magnet—oscillates within the pick-up coil, it induces a current in the coil due to Lenz's law. This induced current is then transferred to a flux transformer, which in turn generates a corresponding magnetic field within the superconducting loop of the SQUID. The resulting magnetic flux inside the SQUID is directly proportional to the magnetic moment of the sample, enabling precise magnetization measurements.

AC magnetic susceptibility: Magnetic susceptibility is a measure of a sample's magnetization, and it is defined as $\chi = M/H$, where M is magnetization and H is the applied DC magnetic field. In the DC measurement, an AC output signal is detected, but this signal arises from the periodic movement of the sample, and therefore, it does not represent the response of the sample with respect to time variation. On the other hand, in an AC measurement, the moment of the sample changes in response to an applied AC magnetic field, and thus, the dynamics of the magnetic system can be studied. The principle of measuring AC susceptibility involves subjecting the sample to a small alternating magnetic field, $H = H_{ac}cos(\omega t)$, where H_{ac} is the amplitude of the field. Simultaneously, a static DC magnetic field may also be applied. The flux variation due to the sample is picked up by

the sensing coil surrounding the sample, and the resulting voltage induced in the coil is detected. For a measurement, the sample is placed between the superconducting magnets and in a well-uniform magnetic field, which creates a magnetic moment in the sample. During a typical AC susceptibility measurement, the sample vibrates in a sinusoidal motion, further generating a sinusoidal signal in pick-up coils placed appropriately. The voltage induced in the pick-up coil is then amplified and measured using a lock-in amplifier in the VSM detection module.

2.2.5 Electrical Transport Measurement

Electronic transport refers to the movement of charge carriers, primarily electrons and holes, through a material in response to external stimuli such as electric fields, temperature gradients, or magnetic fields. This fundamental process is central to understanding and designing materials for electronic, thermoelectric, and spintronic applications. At the most basic level, electronic transport follows Ohm's law, which relates the current density to the applied electric field through the electrical conductivity. The classical Drude model offers an early description, treating electrons as classical particles that scatter off lattice ions, leading to an expression for conductivity in terms of carrier density, charge, relaxation time, and effective mass. Further, a more accurate and general framework is provided by the Boltzmann transport equation, which incorporates the electronic band structure and various scattering mechanisms to describe transport phenomena like resistivity, Seebeck coefficient, and Hall effect across a range of temperatures and external fields. At low temperatures, various effects, such as weak localization, Kondo effect, and variable range hopping, can significantly alter the transport behavior, often requiring quantum mechanical treatment.

Electrical transport measurements are fundamental characterization techniques that offer valuable insights into a material's scattering mechanisms and electronic band structure. In this study, the electrical resistivity of the samples was measured using the standard four-probe technique with
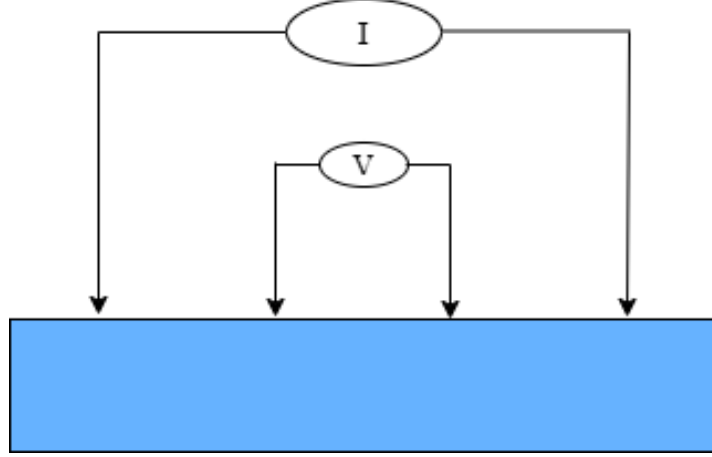
Figure 2.7: Schematic diagram of connections to measure electrical resistivity using the 4-probe method. Outer two probes represent the constant current supply, while the inner two probes are used to measure the voltage.

a home-built resistivity setup integrated with a superconducting magnet system. Rectangular bar-shaped specimens were prepared by cutting the samples with a low-speed diamond saw to ensure uniform geometry. Electrical contacts were established using high-purity silver epoxy and fine copper wires. Here, a constant current is applied through the outer probes (+I and –I), while the resulting voltage drop is measured across the inner probes (+V and –V). To eliminate thermoelectric effects and enhance measurement accuracy, the direction of the current is reversed during each cycle. The resistance R is calculated using Ohm's law, $R = V/I$. This technique effectively removes the contribution of contact resistance and offers higher sensitivity. The sample's electrical resistivity ρ is determined using the relation $\rho = RA/l$, where A is the cross-sectional area of the sample, and l is the distance between the voltage probes.

Additionally, some measurements were carried out using a home-built electrical resistivity setup based on a Closed-Cycle Refrigerator (CCR) system. In this configuration, the temperature was controlled using a CCR unit from JANIS, USA, in combination with a Lakeshore 335 temperature controller. The current was supplied using a Keithley 6221 DC & AC current source, and the voltage was measured with a Keithley 2182A Nanovoltmeter.
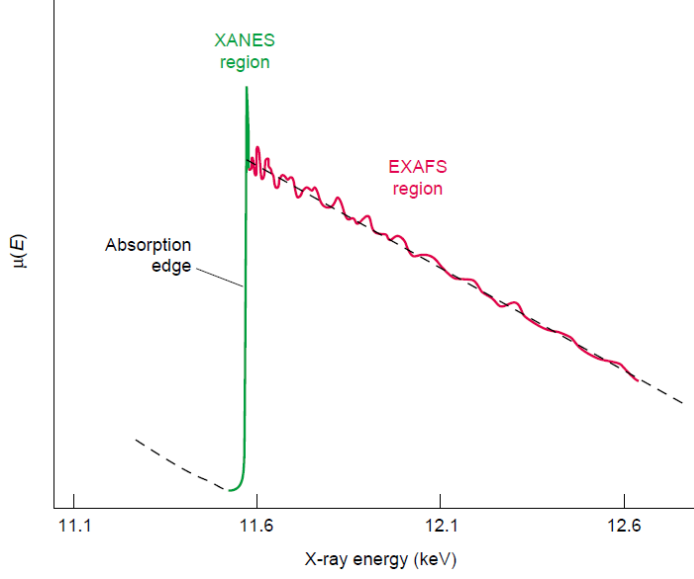
Figure 2.8: A typical XAS spectrum showing absorption edge, XANES, and EXAFS regions.

2.2.6 X-ray absorption spectroscopy

In X-ray absorption spectroscopy (XAS), a sample is irradiated with monochromatic X-rays of energy $h\nu$, and the absorption is monitored as the photon energy is scanned. When the incident photon energy becomes sufficient to excite a core-level electron to states above the Fermi level, a sharp increase—or an "edge"—in the absorption cross-section is observed, marking the onset of a particular absorption edge. XAS spectra are traditionally measured in transmission mode, where the absorption is inferred from the ratio of the X-ray intensity before (I_0) and after (I) passing through the sample. The transmitted intensity, I, depends on the sample thickness t and the absorption coefficient μ, and follows the Lambert-Beer law: $I = I_0 e^{-\mu t}$.

The X-ray absorption coefficient μ generally exhibits a smooth dependence on photon energy and can be approximately expressed as $\mu = \frac{\rho Z^4}{ME^3}$, where ρ is material's density, Z is the atomic number, M is the atomic mass, and E is the photon energy. However, the smooth variation in μ is only an approximate behavior. After the absorption edge, the absorption coefficient exhibits a fine structure, called X-ray Absorption Fine Structure (XAFS),

due to the quantum mechanical effects. XAFS is conventionally divided into two regimes for practical interpretation: X-ray Absorption Near Edge Structure (XANES) and Extended X-ray Absorption Fine Structure (EXAFS). Although both arise from the same underlying quantum mechanical processes, this division is helpful in distinguishing their distinct sensitivities. XANES, which spans the region close to the absorption edge, is particularly sensitive to the absorbing atom's oxidation state and local coordination environment (e.g., tetrahedral or octahedral geometry). In contrast, EXAFS—occurring at higher energies beyond the edge—provides quantitative information on the local atomic structure, such as interatomic distances, coordination numbers, and the types of neighboring atoms.

In this thesis, EXAFS measurements are performed using a synchrotron source at DESY–PETRA III, Germany, and the data were analyzed using the Demeter software suite [54].

2.3 Theoretical Methods

2.3.1 Introduction

The theoretical picture of any material involves the inhomogeneous electron gas moving in a potential field of atomic nuclei, which is considered static (Born-Oppenheimer approximation). Solving such models requires approximation schemes, such as the independent electron approximation (Hartree approximation and Hartree-Fock approximation). However, density functional theory (DFT) is one of the most widely used methods for "*ab initio*" calculations of the structure of atoms, molecules, crystals, surfaces, and their interaction. It has tremendous application for calculating the band structure and density of the state of electrons in solids. In particular, it has successfully explained the electronic structure and magnetic properties of transition metals and their alloys.

DFT is an approach to solving the Schrödinger equation by writ-

ing the quantities of interest, in terms of particle density, $n(\vec{r})$, instead of the many-electron wave function. The advantage of using the $n(\vec{r})$ is that it has only three variables, which are the position coordinates, while the many-electron wave function has $3N$ (N is several electrons). Consequently, many-body Schrödinger equation can be treated as a single-particle Hartree-type equation in terms of electron density, which experiences an effective potential.

2.3.2 Hohenberg-Kohn theorems

The first Hohenberg-Kohn theorem states that "*the ground state density $n(\vec{r})$ of the interacting electrons in some external potential V_{ext} determines this potential uniquely and hence ground state energy.*

$$E_0 = E[n_0] = < \psi_0 | \hat{T} + \hat{V}_{ext} + \hat{U}_{ee} | \psi_0 > \qquad (2.4)$$

where, $\psi_0 = \psi(n_0)$. The external potential $< \psi_0 | V_{ext} | \psi_0 > = V_{ext}[n_0]$.

This theorem says that there cannot be two different V_{ext} that yield the exact ground state electron density, or, in other words, the ground state density uniquely specifies the external potential V_{ext}.

The second Hohenberg-Kohn theorem says that "*For any given density (r) associated to an N electron system with external potential $V_{ext}(r)$ the minimum of the energy functional is obtained with the ground state density.*

$$E_0 \le E[n] = T[n] + V_{ext}[n] + U_{ee}[n] \qquad (2.5)$$

This theorem establishes that the ground-state electron density uniquely determines the system's total energy, and it provides the basis for the variational principle used in density functional theory (DFT) calculations.

2.3.3 Kohn-Sham equations

The Kohn-Sham equations are foundational principles in density functional theory (DFT) that provide a practical framework for calculating the ground-state properties of many-electron systems. They suggested that the exact ground-state energy of an interacting many-electron system can be obtained by solving a set of non-interacting single-particle equations, provided that the precise exchange-correlation function is known.

Thus, in the Kohn-Sham approach, a fictitious non-interacting system is constructed so that its density is the same as that of the interacting electrons. The system is described by a set of single-particle Schrödinger-like equations:

$$\left(\frac{-\hbar^2}{2m}\Delta^2 + V_{eff}(r) \right) \psi(r) = E\psi \tag{2.6}$$

where, ψ is Kohn-Sham orbitals, E is orbital energy, and $V_{eff}(r)$ is effective potential defined as,

$$V_{eff}(r) = V_{ext}(r) + V_{Hartree}(r) + V_{xc}(r) \tag{2.7}$$

The Kohn-Sham equation has to be solved self-consistently. Starting with the initial guess for the electron density $n(r)$, the corresponding effective potential $V_{eff}(r)$. A new electron density is computed from these initial guesses, and the previous steps are carried out. This procedure is then repeated until convergence is reached. Once this is done, the ground state energy can be expressed by,

$$E[n] = T[n] + \int n(r)V_{ext}dr + E_{Hartree}[n] + E_{XC}[n] \tag{2.8}$$

where $T[n]$, $E_{Hartree}[n]$, and $E_{XC}[n]$ represents kinetic energy of non-interacting electrons, classical Coulomb energy of charge density, and exchange-correlation energy, which accounts for all quantum mechanical interactions, respectively. The accuracy of the Kohn-Sham method depends on the approximation used for $E_{xc}[n]$, as the exact functional is generally unknown.

2.3.4 Exchange-Correlation energy functional

The exchange and correlation interactions in DFT represent the quantum mechanical effects of electron behavior beyond the classical explanation of electron-electron repulsion. The exchange-correlation energy functional, $E_{xc}[n]$, incorporates these effects in the ground state energy of the system. The first effect (electron exchange) arises based on the Pauli exclusion principle, which states that two electrons with a similar spin state cannot occupy the same energy state. Hartree-Fock approximation incorporates exact exchange energy, while the electron correlation effect is ignored. The correlation interaction explains the many-body effects of the dynamic correlation between electrons. The difference between the exact ground state energy and the Hartree-Fock approximated energy is called correlation energy, E_C. The exchange-correlation energy functional combines the exchange and correlation effects into a single term: $E_{XC}[n] = E_X[n] + E_C[n]$. The exact form of $E_{xc}[n]$ is unknown and must be approximated for practical calculations.

2.3.4.1 Approximations for Exchange-Correlation energy functional

(a) Local density approximation (LDA): LDA is the simplest and widely used approximation for exchange-correlation energy. In this approximation, the electron density is considered to be locally smooth and varying. In LDA, the E_{XC} is expressed as

$$E_{xc}[n(r)] = \int n(r)\epsilon_{XC}[n(r)]d^3r \tag{2.9}$$

where ϵ_{XC} is the exchange and correlation energy per particle of the homogeneous electron gas of density $n(r)$.

LDA works very accurately for bulk metals, where slowly varying electron density can be compared with the homogeneous electron gas. However, cell parameters are usually underestimated in this approximation, and the

bulk modulus is overestimated. Binding energies are almost always overestimated, while it tends to underestimate atomic ground state energies and ionization energies.

(b) Generalized Gradient Approximation (GGA): In a real system, the electron density can not be considered homogeneous because there are non-local correlation effects. So, in the circumstances, the density variation is given by the expansion of density in terms of its gradient *i.e.* $\Delta n(r)$, $\Delta^2 n(r)$. Considering only the linear term of the electron density gradient, the GGA can be written as

$$E_{XC}[n(r)] = \int n(r)\epsilon_{XC}[n(r), \Delta(r)]d^3r \qquad (2.10)$$

GGA describes the magnetic and structural ground state quite accurately for transition metals and alloys compared to the LDA.

2.3.5 DFT implementation by Quantum Espresso

Computationally less expensive but reasonably accurate calculations can be performed by pseudopotentials or projector augmented wave (PAW) potentials, as it does not use core-level electrons as a part of the basis set. Quantum Espresso (QE) is an open-source suite of code based on the methods of plane-wave potentials for performing DFT calculations [55, 56]. This thesis uses ultrasoft pseudopotentials, a plane wave basis set, and generalized gradient approximation with Perdew-Burke-Ernzerhof (PBE) functional form for exchange-correlation energy [57]. The implementation of DFT using QE involves steps like (i) preparation of structural information, such as atomic positions and lattice parameters, and (ii) performing self-consistent field (SCF) calculations, where ground state electronic density is iteratively determined by solving Kohn-Sham equations, and (iii) various post-DFT tools (e.g. dos.x, band.x) have been implemented for analyzing the results.

2.3.6 SPR-KKR: Exchange interaction calculation

The spin-polarized relativistic Korringa-Kohn-Rostoker (SPR-KKR) package allows the calculation of the electronic structure of arbitrary three-dimensional periodic systems. The SPR-KKR package is based on the KKR-Green's function formalism, which makes use of multiple scattering theory. This implies that the information on the electronic structure of a system is not expressed in terms of Bloch wave function and eigenvalues, but the corresponding Green's function, leading to the extreme flexibility of the method.

Using the SPR-KKR package, it is possible to calculate the exchange coupling parameters J_{ij} of the Heisenberg model

$$H_{ex} = -\Sigma J_{ij} e_i e_j \tag{2.11}$$

where e_i and e_j are unit vectors having the directions of the corresponding local magnetic moment on-site i and j, where

$$J_{ij} = \frac{1}{4\pi} Im \int^{E_F} Trace(t_{i\uparrow}^{-1} - t_{i\downarrow}^{-1})(t_{j\uparrow}^{-1} - t_{j\downarrow}^{-1})\tau_{\downarrow}^{ij} dE \tag{2.12}$$

The J_{ij} are calculated with respect to the central site i of a cluster with radius $R_{clu} = max|R_i - R_j|$.

.

Chapter 3

Identification of disorder and effect of annealing on physical properties of half-metallic Fe-Ti-Sn based Heusler alloys

3.1 Overview

In literature, various attempts have been made to decrease the antisite disorder in Fe_2TiSn. In their works, Chaudhuri et al. [58–60], have demonstrated that with proper substitution for Sn and Ti sites, the antisite disorders are controllable and the system can be driven to the half-metallicity. For example, the substitution of Sb at the Sn site increases the saturation magnetization from 0.1 $\mu_B/f.u.$ for Fe_2TiSn to 0.45 $\mu_B/f.u.$ for $Fe_2TiSn_{0.5}Sb_{0.5}$, and system shows the half-metallic characteristics. This increase in the magnetic moment is attributed to the enhanced RKKY-type Fe-Fe interaction upon Sb substitution. However, the saturation magnetic moment in this compound deviates from the Slater-Pauling rule. The presence of antisite disorder in Heusler alloys is one of the main reasons for such deviation. A similar situation has also emerged in $Fe_2Ti_{0.75}Cr_{0.25}Sn$. Despite various strategies to decrease the antisite disorder in Fe_2TiSn with

proper substitution targeting the Ti and Sn sites, a quantitative assessment of its extent and nature within these compounds is lacking. Thus, We present a neutron diffraction study on Fe_2TiSn, $Fe_2Ti_{0.75}Cr_{0.25}Sn$ and $Fe_2TiSn_{0.5}Sb_{0.5}$, aimed at quantifying the disorder. Furthermore, the effect of secondary annealing on disorder was investigated using electrical resistivity and magnetization measurements. Neutron diffraction proved invaluable in elucidating the atomic arrangements and site occupancies critical for understanding the disorder. Our findings underscore the importance of quantifying antisite disorder in Heusler compounds and highlight the role of neutron diffraction in this endeavor. Additionally, the impact of secondary annealing on the disorder, as revealed by electrical resistivity and magnetization measurements, provides valuable insights for the design and development of half-metallic Heusler alloys for spintronic applications.

3.1.1 Neutron diffraction

The evolution of NPD patterns with temperature for the three compositions is shown in Fig.3.1. Preliminary analysis indicates that these compounds crystallize in the cubic structure with Fm$\bar{3}$m space group. The crystal structure remains unchanged in the 2.5 K to 320 K temperature range. Further, no extra peak is seen in any of the low-temperature patterns, nor is there any enhancement in the intensity of the Bragg peaks that could indicate magnetic scattering. The temperature dependence of the integrated intensity of some selected Bragg peaks reveals no enhancement of intensity at low temperatures due to magnetic scattering. These results show the possible absence of long-range ferromagnetic and/or antiferromagnetic ordering in the compositions.

Next, we analyze the crystal structure of these as-prepared compositions to identify the extent of disorder in them. Since the neutron scattering amplitudes of Fe (9.45 fm), Ti (-3.44 fm), and Sn (6.33 fm) are very different, NPD measurement is advantageous in this regard. Fig.3.2 shows the Rietveld refinement of the neutron diffraction pattern at high temperature

Table 3.1: Atomic coordinates and site occupancies for as-prepared Fe_2TiSn, $Fe_2Ti_{0.75}Cr_{0.25}Sn$, and $Fe_2TiSn_{0.5}Sb_{0.5}$ obtained after Rietveld refinement of NPD data measured at 300 K.

Composition	Atoms	Wyckoff Position	x	y	z	Occupancy
			Fractional coordinate			
Fe_2TiSn	Fe/Ti	$8c$	0.25	0.25	0.25	0.974(4)/0.026(11)
	Ti/Fe	$4b$	0.5	0.5	0.5	0.948(4)/0.052(1)
	Sn	$4a$	0	0	0	1
$Fe_2TiSn_{0.5}Sb_{0.5}$	Fe/Ti/Sb	$8c$	0.25	0.25	0.25	0.872(3) / 0.025(1) / 0.103(3)
	Ti/Fe	$4b$	0.5	0.5	0.5	0.950(1) / 0.050(1)
	Sn/Sb/Fe	$4a$	0	0	0	0.501(1) / 0.294(3) / 0.206(3)
$Fe_2Ti_{0.75}Cr_{0.25}Sn$	Fe/Ti	$8c$	0.25	0.25	0.25	0.955(1) / 0.045(1)
	Ti/Fe/Cr	$4b$	0.5	0.5	0.5	0.660(1) / 0.089(1) / 0.25(4)
	Sn	$4a$	0	0	0	1
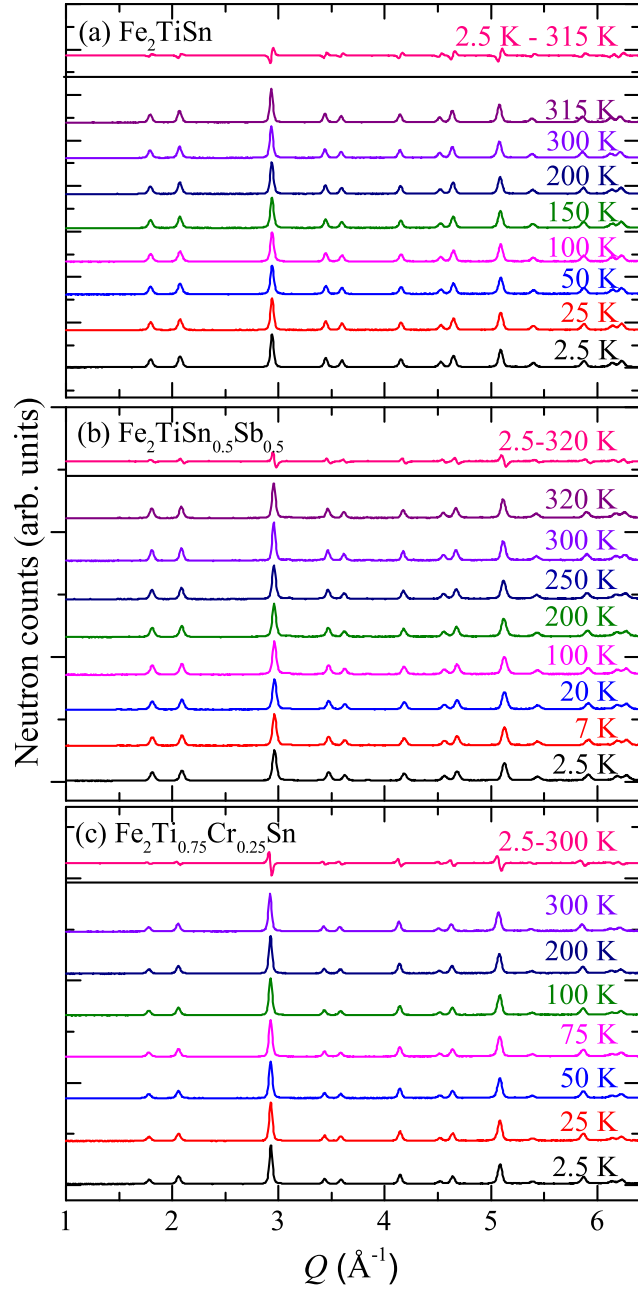
Figure 3.1: Temperature evolution of neutron diffraction patterns for as-prepared (a) Fe_2TiSn, (b) $Fe_2TiSn_{0.5}Sb_{0.5}$, and (c) $Fe_2Ti_{0.75}Cr_{0.25}Sn$. A difference pattern between 2.5 K and the maximum measured temperature is also shown in the upper panel of each picture.

(paramagnetic phase) and 2.5 K (below the magnetic ordering temperature). The quality of the refinement is evident from the close agreement between the observed and calculated patterns. The diffraction patterns at both temperatures are nearly identical, with no observable additional
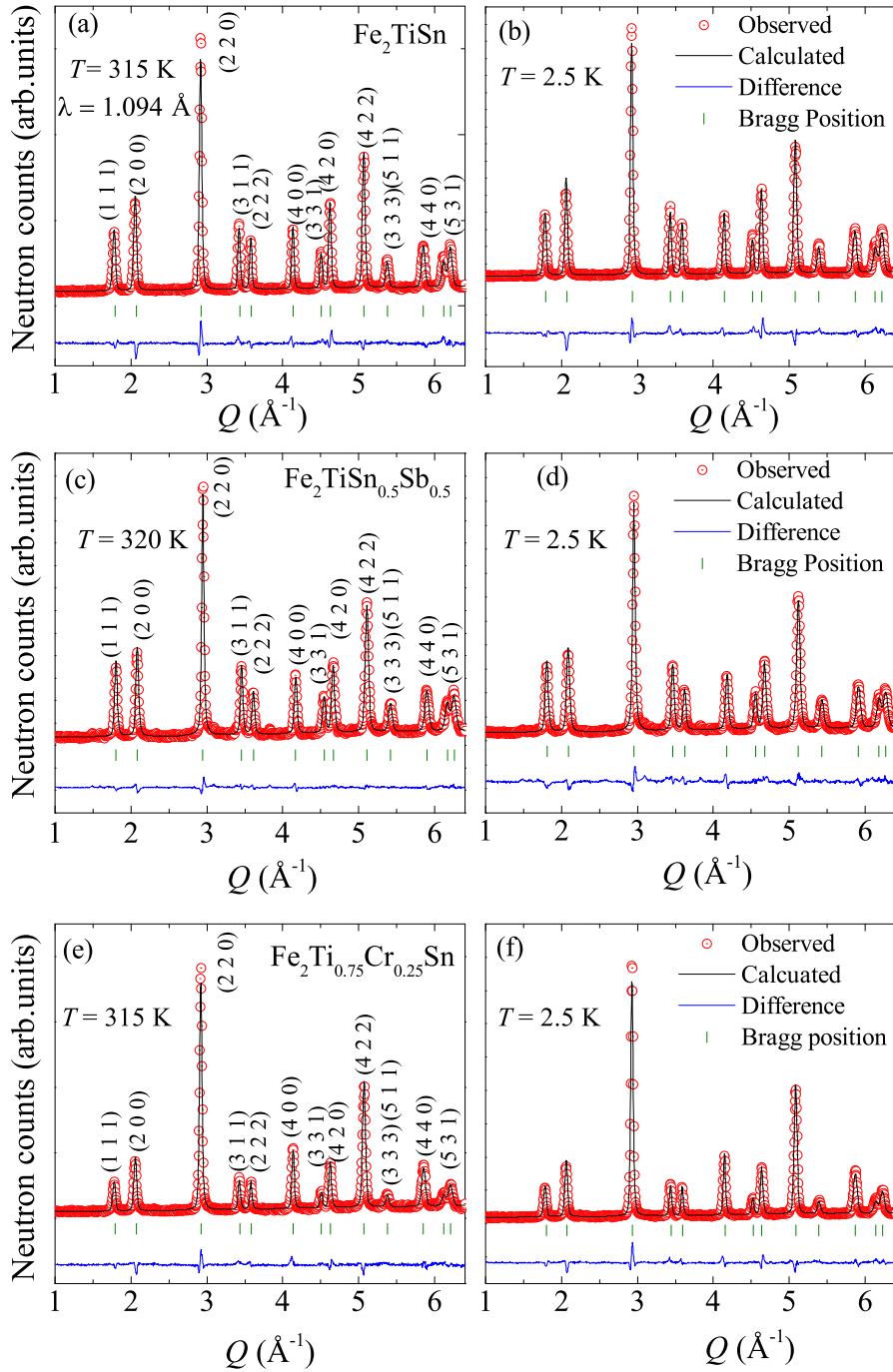
Figure 3.2: Rietveld refinement of the powder neutron diffraction patterns at high temperature (paramagnetic phase) and 2.5 K for (a,b) Fe_2TiSn, (c,d) $Fe_2TiSn_{0.5}Sb_{0.5}$, and (e,f) $Fe_2Ti_{0.75}Cr_{0.25}Sn$, respectively.

peaks or changes in peak positions or intensities. This confirms the structural stability of the compositions across the temperature range and rules out the possibility of any structural phase transitions occurring below the magnetic ordering temperature. Table 3.1 presents the values of atomic

coordinates and site occupancies after refinement. Fe_2TiSn contains four formula units in a unit cell, which include 8 Fe atoms at the $8c$ site, 4 Ti, and 4 Sn atoms at $4b$ and $4a$ sites, respectively. Refinement of the data indicates mixing between Fe and Ti atoms at the Wyckoff positions (0.25, 0.25, 0.25) and (0.5, 0.5, 0.5), while the Sn atoms reside at the Wyckoff position (0, 0, 0) without detectable mixing. A similar situation is found in $Fe_2Ti_{0.75}Cr_{0.25}Sn$, where slight mixing of Fe and Ti is present at site $8c$ (0.25, 0.25, 0.25) and $4b$ (0.5, 0.5, 0.5), respectively. However, in the case of $Fe_2TiSn_{0.5}Sb_{0.5}$ the antisite disorder becomes more complex. In addition to the Fe/Ti mixing between $8c$ and $4a$ site, there is also a significant antisite disorder between the $8c$ (Fe) and $4a$ (Sn/Sb) sites. The lattice constant obtained from the room temperature NPD patterns (paramagnetic phase) decreases from 6.0757(2)Å in Fe_2TiSn to 6.02727(7)Å in Sb-substituted $Fe_2TiSn_{0.5}Sb_{0.5}$, while it remains nearly unchanged in $Fe_2Ti_{0.75}Cr_{0.25}Sn$.

Given that the magnetic interactions in Heusler alloys are largely governed by the Ruderman–Kittel–Kasuya–Yosida (RKKY)-type exchange interaction, which is sensitive to the separation between the magnetic ions, such changes in the lattice constant induced by atomic substitution significantly influence these materials' magnetic and transport properties. Previous studies of the local crystal structure using X-ray Absorption Spectroscopy (XAFS) indicate that reduced lattice parameters in Sb substituted Fe_2TiSn shorten the Fe - Fe bond distance such that it enhances the RKKY-type exchange interaction between them [58]. In contrast, due to no significant change in lattice constants of 25% Cr substituted composition, the local structure around magnetic ions like Fe or Cr is not affected, and the magnetic ordering seen in this compound results from the strong localized moments formed at Cr sites [60]. The present NPD results also reinforce the inference drawn from such earlier studies.
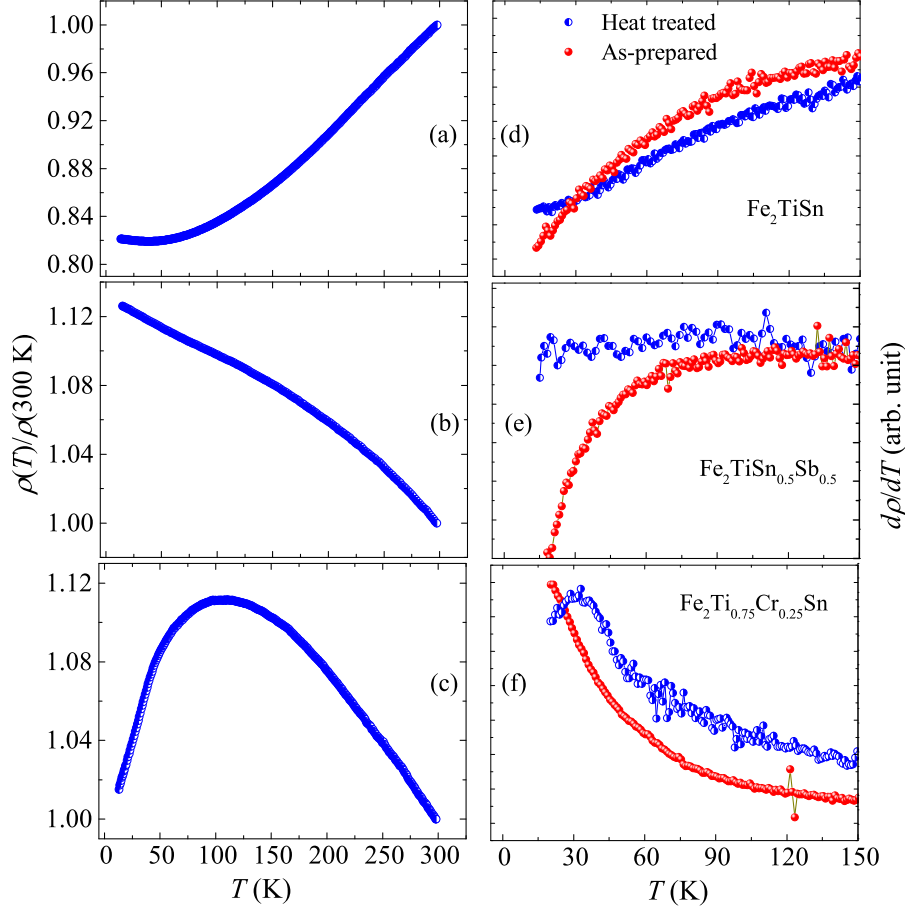
Figure 3.3: (a)-(c) The temperature variation of normalized electrical resistivity of the heat-treated Fe_2TiSn, $Fe_2TiSn_{0.5}Sb_{0.5}$, and $Fe_2Ti_{0.75}Cr_{0.25}Sn$, and (d)-(f) the temperature derivative of the electrical resistivity of the as-prepared and heat-treated Fe_2TiSn, $Fe_2TiSn_{0.5}Sb_{0.5}$, and $Fe_2Ti_{0.75}Cr_{0.25}Sn$ respectively.

3.1.2 Electrical resistivity

A secondary annealing treatment of the as-prepared compositions effectively tunes its anti-site disorder. A visual illustration of this is seen by comparing the temperature dependence of electrical resistivity curves obtained for the as-prepared and heat-treated (Fig.3.3) samples of the three compositions. The normalized electrical resistivity, $\rho(T)/\rho(300)$, of the heat-treated samples is presented in Fig.3.3(a-c). Overall, the resistivity curves of the heat-treated samples appear similar to those of the as-prepared samples, with significant differences in $\rho(T)$ curves at low tem-

peratures. In the case of Fe_2TiSn, the low-temperature upturn in the $\rho(T)$ of the as-prepared sample flattens out after heat treatment. To emphasize this further, the low-temperature resistivity is fitted using the equation $\rho(T) = \rho_0 + \rho_{e-e}T^2 - \rho_{WL}T^{1/2}$, where ρ_0, ρ_{e-e} and ρ_{WL} represents residual resistivity, coefficient of electron-electron interaction and last term represents contribution from weak localization. The fitting yields a value of ρ_{WL} to be 0.52×10^{-6} for heat-treated Fe_2TiSn, which is lower than the as-prepared composition (16.91×10^{-6}) as reported in Ref. [58]. The reduction in the value of ρ_{WL} quantifies the marked decrease in the weak localization effect, directly pointing to a substantial reduction in anti-site disorder after the heat treatment of the sample. Likewise, the cusp-like feature reported in the as-prepared $Fe_2TiSn_{0.5}Sb_{0.5}$ disappears, and linear variation in $\rho(T)$ is observed for its heat-treated counterpart. The sudden drop in the low-temperature $\rho(T)$ of the as-prepared $Fe_2Ti_{0.75}Cr_{0.25}Sn$ changes its curvature in the heat-treated sample. All these features are very pronounced in the $d\rho/dT$ curve of all these samples, as shown in Fig.3.3(d-f).

Despite the possible prediction of half-metallicity in $Fe_2TiSn_{0.5}Sb_{0.5}$ and $Fe_2Ti_{0.75}Cr_{0.25}Sn$, the low-temperature resistivity behavior of both these compositions is quite different. As shown in Fig.3.3(b), the low-temperature $\rho(T)$ of $Fe_2TiSn_{0.5}Sb_{0.5}$ shows a linear increase in the resistivity up to the lowest measured temperature. Previously it has been shown in Ref. [59] that the low-temperature resistivity of the as-prepared $Fe_2TiSn_{0.5}Sb_{0.5}$ fits the description of the phonon-assisted variable range hopping (VRH) mechanism, where $\rho(T) \propto \exp(T_0/T)^{-1/4}$. The present NPD analysis of as-prepared $Fe_2TiSn_{0.5}Sb_{0.5}$ fully agrees with such a transport mechanism, as the presence of significant anti-site disorder leads to localized impurity states between the valence and conduction bands that dominate the electron transport in terms of a hopping mechanism. However, the same VRH mechanism does not provide a good fit to the low temperature $\rho(T)$ data of the heat-treated sample, indicating a substantial decrease in spatially localized electronic states near the Fermi level. Thus, the combined electrical resistivity and NPD analysis highlight that

the secondary annealing effectively reduces anti-site disorder in the heat-treated $Fe_2TiSn_{0.5}Sb_{0.5}$. In the case of as-prepared $Fe_2Ti_{0.75}Cr_{0.25}Sn$, $\rho(T)$ increases with decreasing temperature up to the magnetic ordering temperature below which it shows a downward fall [60]. A similar trend is seen in its heat-treated counterpart. Still, unlike the as-prepared sample where $d\rho/dT$ continues to increase down to the lowest measurement temperature, the heat-treated sample shows a decrease in $d\rho/dT$ below 30 K. This behavior aligns with that observed in Fe_2TiSn and $Fe_2TiSn_{0.5}Sb_{0.5}$ after heat treatment, indicating that the change in $d\rho/dT$ is due to a reduction in anti-site disorder.

3.1.3   Magnetic properties
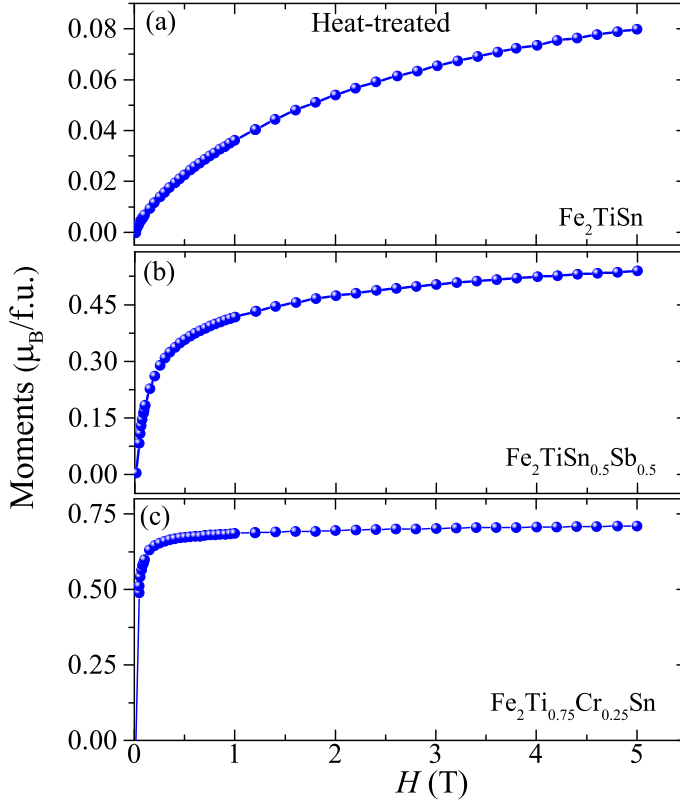
Figure 3.4: Isothermal field dependent magnetization curve of heat-treated (a) Fe_2TiSn, (b) $Fe_2TiSn_{0.5}Sb_{0.5}$, and (c) $Fe_2Ti_{0.75}Cr_{0.25}Sn$ at $T = 5$ K.

The isothermal magnetization, $M(H)$, recorded for the heat-treated samples is shown in Fig.3.4. The effect of reduction in anti-site disorder

is also seen in the magnetic properties. Compared to the $M(H)$ curve of as-prepared compositions reported in the literature, the heat-treated samples show a decrease in the saturation magnetic moment (M_S) of Fe_2TiSn by one order of magnitude. As discussed in the literature, Fe-Ti anti-site disorder in Fe_2TiSn gives rise to ferromagnetically interacting clusters. The decrease in M_S value, from 0.18 μ_B/f.u. for an as-prepared sample to 0.08 μ_B/f.u. for heat-treated sample, supports the inference regarding the reduction of the overall disorder after secondary heat treatment. Notably, the M_S value of the heat-treated sample closely aligns with that of 7% Ti substituted $Fe_{2-x}Ti_{1+x}Sn$, a composition known for exhibiting minimal anti-site disorder in the Fe-Ti-Sn system [61]. In Fe_2TiSn, Fe-Ti and Fe-Sn anti-site disorder are magnetic, and when such defects are present at a concentration comparable to the experimental values, they significantly affect the magnetic properties [62]. In the case of heat-treated $Fe_2TiSn_{0.5}Sb_{0.5}$, the M_S value increases from 0.45 μ_B/f.u. (as-prepared) to 0.52 μ_B/f.u., which matches the theoretically predicted SP value for half-metallic composition. In this composition, the magnetic behavior is primarily driven by Sb substitution, with contributions from Fe-Ti and Fe-Sn(Sb) defects depending on growth conditions [62, 63]. Our NPD analysis confirms the presence of Ti-Fe and Fe-Sn(Sb) anti-site disorder in the as-prepared sample, which is healed with heat treatment, resulting in a M_S value closer to the value obtained from the SP rule. On the other hand, the heat-treated $Fe_2Ti_{0.75}Cr_{0.25}Sn$ tends to saturate more easily with an increasing magnetic field compared to its as-prepared counterpart. The $M(H)$ of as-prepared $Fe_2Ti_{0.75}Cr_{0.25}Sn$ displays a soft magnetic nature with magnetization that does not fully saturate even at 5 T and attributed to the competing FM/AFM interactions due to anti-site disorder [60].

It is apparent that the disorder significantly affects the electrical and magnetic properties of Heusler alloys. In a system with desirable half-metallicity, the anti-site disorder can introduce impurity electronic states at the Fermi level, as observed in the $Fe_2TiSn_{0.5}Sb_{0.5}$. These impurity states decrease the degree of spin-polarization, compromising the half-metallic

nature. The present study demonstrates that secondary annealing at lower temperatures effectively heals anti-site disorder, and a more ordered crystal structure can be achieved. As a result, the impurity states associated with the inherent anti-site disorder are eliminated, and high spin polarization can be restored. Thus, secondary annealing could be a key step in tuning the crystal structure of Heusler alloys, ensuring the integrity of half-metallicity. Effective spin injection and transport depend on high spin polarization in spintronic systems like magnetic tunnel junctions, spin valves, and spin-transfer torque memory. This work immediately helps the development of next-generation spintronic technologies by offering a means to reduce disorder and optimize the performance of half-metallic Heusler alloys.

3.2   Conclusion

In summary, temperature dependent neutron diffraction confirms the single-phase Heusler structure for Fe_2TiSn, $Fe_2TiSn_{0.5}Sb_{0.5}$ and $Fe_2Ti_{0.75}Cr_{0.25}Sn$, with no structural transition down to 2.5 K. Despite no significant increase in peak intensity below the magnetic transition temperature, likely due to a weak magnetic signal, refinement reveals antisite disorder between Fe and Ti sites. Secondary heat treatment of the same samples at 600°C led to a marked reduction in anti-site disorder, as confirmed by temperature-dependent resistivity and isothermal field-dependent magnetization measurements. These findings underscore the beneficial impact of heat treatment on improving the magnetic and structural properties of the samples, emphasizing the critical role of annealing processes in tailoring material properties for potential applications in spintronics and related fields.

.

Chapter 4

Identification of Griffiths'-like phase in Heusler antiferromagnet

4.1 Overview

Mn-based Heusler alloys have diverse applications in spintronics, spin-transfer torque MRAM, shape memory alloys, and spin-gapless semiconductors. Among them, half-metallic ferrimagnets (HMFIs), such as Mn_2YZ compounds, are particularly intriguing due to their low total magnetic moment, which minimizes stray fields and enhances stability against external fields. Theoretically, Mn_2FeSi is predicted to crystallize in an inverse Heusler phase with a magnetic moment of 2 μ_B/f.u, but experimental attempts have resulted in an antiferromagnetic/ferrimagnetic state with multiphase structures, making the pure inverse Heusler phase elusive.

Antisite disorder is a key factor influencing the physical properties of Heusler alloys, yet its effect on the magnetic moment and spin polarization of Mn_2FeSi remains unexplored. Since atomic site exchange is common in Heusler alloys, careful consideration is essential when comparing theoretical and experimental results. To address this, we synthesized Mn_2FeSi in a pure cubic inverse Heusler phase by substituting 10% Al at the Si site

and systematically investigated its magnetic behavior. Our study reveals an antiferromagnetic (AFM) ground state below 50 K and a Griffiths-like phase between 184 K and 260 K in a cubic Heusler system. These findings provide valuable insights into the role of disorder in tuning the electronic and magnetic properties of Heusler alloys.
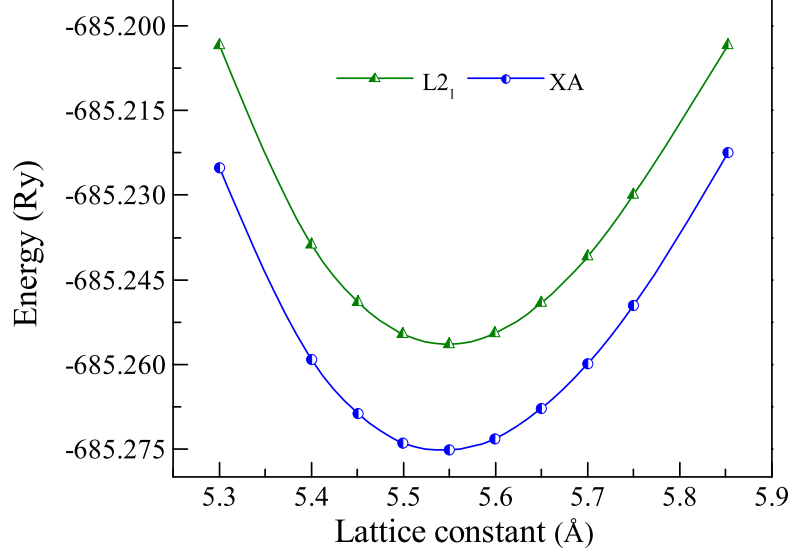
Figure 4.1: Calculated total energy as a function of lattice parameters for the L2$_1$ and XA phase of Mn$_2$FeSi.

4.2 Results and discussion

4.2.1 Electronic structure calculation

The crystal structure of Heusler alloy (formula X_2YZ), where X and Y is transition metal and Z is main group element, can be described as four interpenetrating FCC sublattices at Wyckoff positions A (0,0,0), B (0.25,0.25,0.25), C (0.5,0.5,0.5), and D (0.75,0.75,0.75). These compounds typically crystallize in one of two main structures: Cu_2MnAl-type L2$_1$ and Hg$_2$CuTi-type XA, also known as the inverse Heusler structure. The site preference of the 3d transition metal atoms depends on the number of valence electrons (Z$_V$). If Z$_V(Y)$ > Z$_V(X)$, where X and Y represent transition metal elements from the same period of the periodic table, the two

57
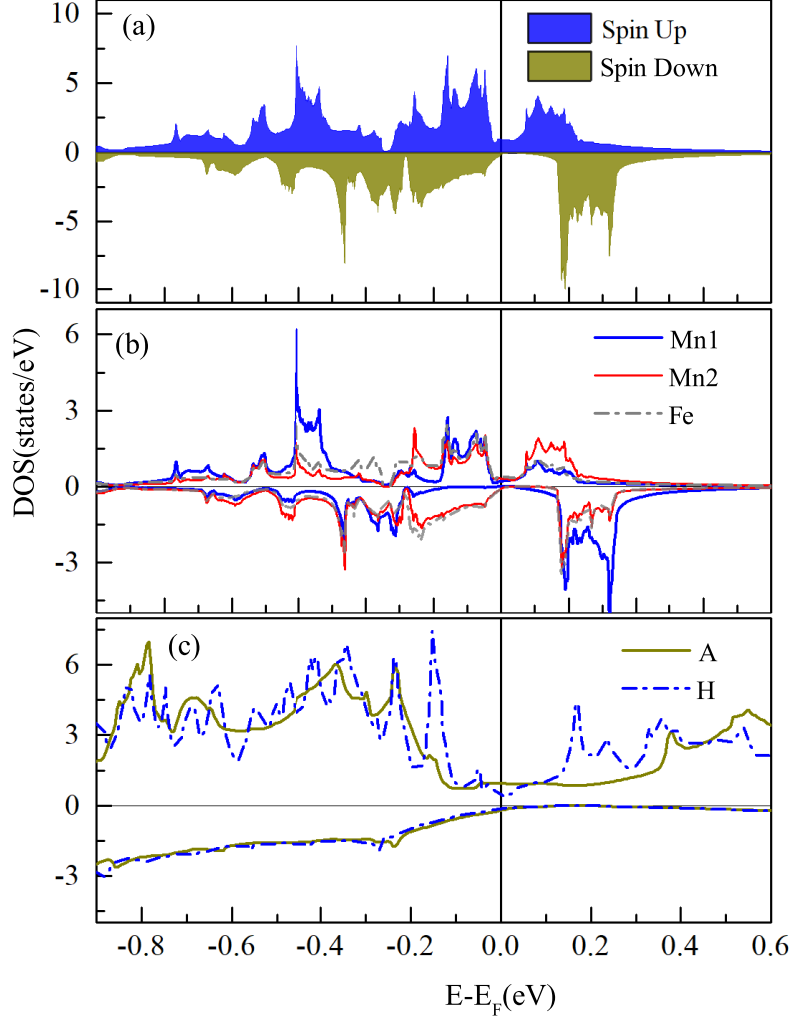
Figure 4.2: Total (a), and partial (b) spin-polarized density of states for Mn$_2$FeSi. (c) A comparison of total DOS at the Fermi level for configuration A and H.

X atoms occupy two inequivalent sites (C and D), forming an XA-type structure. In this configuration, the Y and Z atoms occupy the B and A sites, respectively. For Mn$_2$FeSi, where Mn and Fe are adjacent elements within the same period of the periodic table, the variation of total energy as a function of lattice parameters is calculated for both L2$_1$ and XA type structures, as shown in Fig.4.1, suggests XA-type structure is more stable as compared to L2$_1$. The total energy vs. lattice constant (E vs. a) curve fitted using Birch-Murnaghan's equation enables the determination of the optimized lattice parameter, which is 5.56 Å for the XA type Mn$_2$FeSi structure.
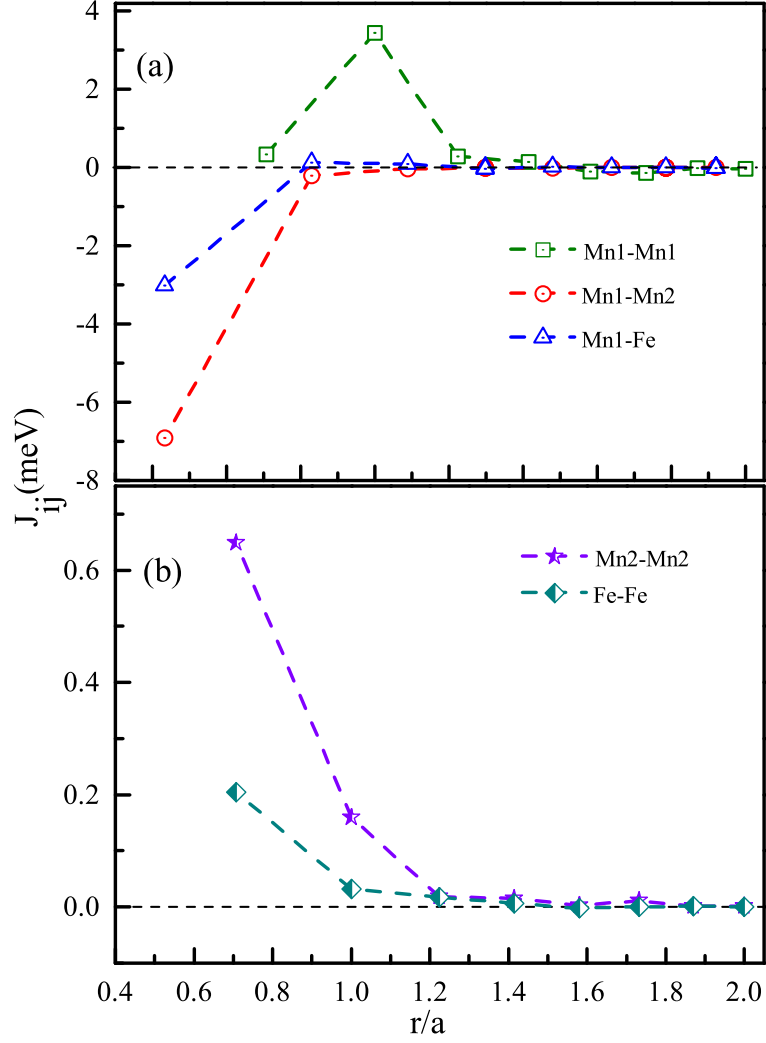
Figure 4.3: Heisenberg exchange coupling parameter, J_{ij}, for (a) Mn1-Mn1, Mn1-Mn2, Mn1-Fe, and (b) Mn2-Mn2, Fe-Fe distances, plotted against the respective bond distances normalized to the lattice parameter.

Further, the calculations explicitly focus on the XA phase of Mn$_2$FeSi, utilizing theoretically obtained equilibrium lattice constant. In this structure, the Mn atoms occupying the C and D sites carry labels Mn1 and Mn2, respectively. The computed magnetic moments are 2.224 μ_B for Mn1, -0.614 μ_B for Mn2, and 0.426 μ_B for Fe, yielding a total magnetic moment of 2.08 $\mu_B/f.u.$. This value aligns with the Slater-Pauling rule for the magnetic moment for a half-metallic Heusler alloy. The low magnetic moment at the Fe site indicates significant quenching of the magnetic moment associated with Fe atoms. Notably, the marked difference in magnetic moments

Table 4.1: Possible atomic configurations resulting from various possibilities of antisite disorder, its relative formation energy, ΔE, and total magnetic moment, M_{cal}. Here ΔE represents the difference in the energy with respect to the ideal XA configuration.

Config.	Wyckoff Positions				ΔE	M_{cal}
	C	D	B	A	(eV)	$(\mu_B/f.u.)$
A	4Mn1	4Mn2	4Fe	4Si	0	2.08
B	3Mn1,Si	4Mn2	4Fe	3Si,Mn1	1.424	1.872
C	2Mn1,2Si	4Mn2	4Fe	2Si,2Mn1	1.893	1.99
D	4Mn1	4Mn2	3Fe,Si	3Si,Fe	3.06	3.22
E	4Mn1	4Mn2	2Fe,2Si	2Si,2Fe	4.376	0.41
F	4Mn1	3Mn2,Si	4Fe	3Si,Mn2	2.897	3.17
G	4Mn1	2Mn2,2Si	4Fe	2Si,2Mn2	4.007	3.36
H	4Mn1	3Mn2,Fe	3Fe,Mn2	4Si	0.081	2.07
I	4Mn1	2Mn2,2Fe	2Fe,Mn2	4Si	0.106	2.08
J	3Mn1,Fe	4Mn2	3Fe,Mn1	4Si	0.307	2.11
K	2Mn1,2Fe	4Mn2	2Fe,2Mn1	4Si	0.581	2.15

between Mn1 and Mn2 atoms is particularly intriguing. Furthermore, each Mn1 atom is surrounded by four antiferromagnetically aligned Mn2 atoms, creating a complex interaction network. This interplay between Mn1 and Mn2 can give rise to competing magnetic interactions, potentially leading to magnetic frustration and/or a non-collinear spin alignment.

Next, we calculated the density of states (DOS) for Mn_2FeSi, shown in Fig. 4.2(a). The result reveals significant DOS at the Fermi level for the spin-up sub-band, whereas E_F is positioned at the valence band's edge for minority spin states, and the system shows high spin polarization. A limited yet significant DOS is present at E_F for minority spin states, with the primary contribution originating from the Mn2 and Fe atoms, as shown in Fig.6.2(b). Consequently, a weak splitting between the spin-up and spin-down states of Mn2 and Fe atoms contributes to its relatively small

magnetic moment than that of the Mn1 atom.

The Heisenberg exchange interaction (J_{ij}) calculations, presented in Fig.4.3, demonstrated the pivotal role of the Mn1-sublattice in governing the magnetic properties of Mn_2FeSi. The RKKY-type exchange interaction between Mn1 atoms is confirmed by oscillatory nature of their J_{ij}. A substantial negative value of interaction energy (-8 meV) between Mn1 and Mn2 indicates the antiferromagnetic (AFM) interactions between these atoms. A small positive value of J_{ij} for the Fe - Fe interaction energy suggests a weak ferromagnetic (FM) contribution and a relatively small magnetic moment in the Fe sublattice.

To examine the impact of antisite disorder on the magnetic and electronic properties of Mn_2FeSi, we performed theoretical calculations by interchanging atoms at their occupied Wyckoff positions. it is to be noted here that unit cell relaxation for a given configuration was performed before the self-consistent field (SCF) calculations, and no change in atomic positions occurred. Table-4.1 presents the configurations obtained by interchanging the transition metals among themselves as well as with the Si atom. Three categories emerge from such swapping: (1) Fe with Si ($B2$-type disorder), (2) Mn1/ Mn2 with Si ($A2$-type disorder), and (3) Mn1/ Mn2 with Fe ($DO3$-type disorder). The total magnetic moment and energy differences (ΔE) for various configurations (B to K) are calculated relative to the XA phase of Mn_2FeSi (configuration A) and are listed in Table-4.1. All configurations show positive ΔE values, indicating they are energetically less favorable than the ideal XA phase. However, configurations where Mn1 and Mn2 are swapped with Fe (H to K) exhibit significantly lower ΔE values and a magnetic moment of approximately 2 μ_B/f.u., compared to those where Si is interchanged with transition metal atoms. This suggests that the formation of $DO3$-type disorder is more energetically favorable than $B2$-type disorder.

Configurations H to K exhibit magnetic moments consistent with the predictions of the Slater-Pauling rule, suggesting that $DO3$-type disorder

has a negligible impact on the half-metallic ground state. Although both configurations A and H maintain a half-metallic density of states (DOS), a comparison at the Fermi level, as shown in Fig. 4.3(c), reveals a reduction in majority spin states for configuration H. The highest total magnetic moment of 3.36 μ_B/f.u. is observed in configuration G, where Si partially swaps positions with Mn2. In contrast, exchanging Si with Fe (configuration E) results in the lowest magnetic moment of 0.41 μ_B/f.u., accompanied by the highest ΔE. These variations highlight the crucial influence of antisite disorder on the magnetic properties of Mn_2FeSi. This interplay between atomic disorder, magnetism, and local atomic environments will be revisited later when discussing the experimentally recorded magnetic moment of Mn_2FeSi.

Motivated by our theoretical calculations, we aim to study the structural and magnetic properties of the pure Heusler phase of Mn_2FeSi with a total absence of the secondary phases or presence in minimal percentages to cause any significant impact. It is well-documented in the literature that achieving a stoichiometric Mn_2FeSi in its pristine Heusler phase presents a formidable challenge. Mindful of this, we employed a strategic approach involving doping a nonmagnetic element, Al, at the Si site to form the $Mn_2FeSi_{1-x}Al_x(x = 0, 0.10, 0.15)$ compositions.

4.2.2 Microstructural Analysis

Electron microscopy was used to examine the surface morphology of $Mn2FeSi1 - xAlx$ compositions with $x = 0$, 0.1, and 0.15. As shown in Fig.4.4, the stoichiometric Mn_2FeSi composition exhibits distinct bright and dark contrasts, indicating the presence of two phases. Energy-dispersive X-ray (EDX) analysis of these regions reveals compositional differences: one corresponds to a Si-deficient phase ($Mn_{2.18}Fe_{1.02}Si_{0.81}$), while the other maintains a near-stoichiometric composition ($Mn_{2.02}Fe_{1.02}Si_{0.99}$). In contrast, the $x = 0.1$ composition displays a uniform, featureless surface, suggesting the formation of a single-phase structure. However, for $x = 0.15$,

the two-phase contrast reappears, indicating a return to phase separation.

Elements	Spectrum 1	Spectrum 2
Mn	54.40	50.57
Fe	25.38	25.40
Si	20.19	24.77
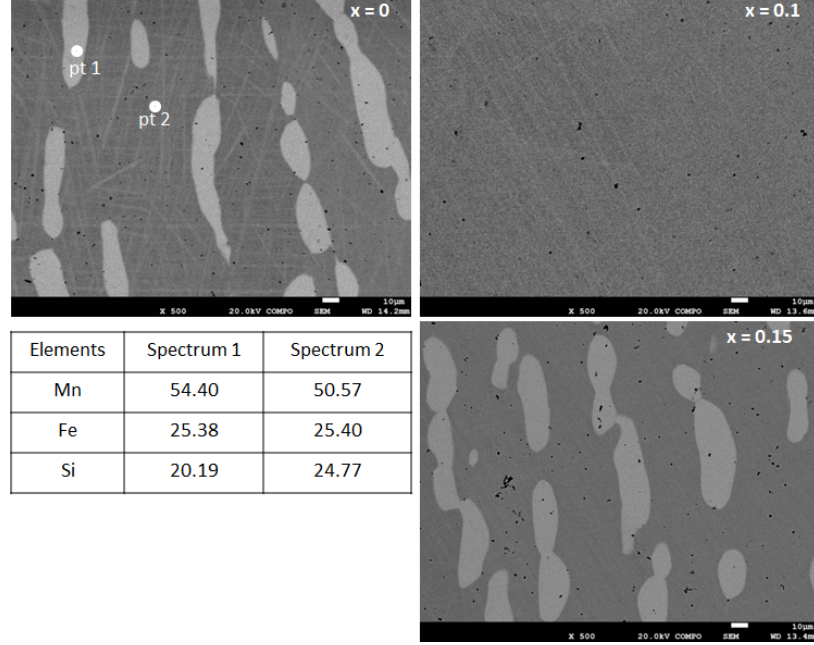
Figure 4.4: Backscattered Electron images of $x = 0$, 0.10, and 0.15, represented at a magnification scale of 10 μm. The table encapsulates the atomic percentage of different elements obtained at the light and dark contrasts observed in the image for $x = 0$ composition.

4.2.3   Structural Analysis

The Powder X-ray Diffraction (XRD) patterns for $Mn_2FeSi_{1-x}Al_x$ ($x = 0$, 0.1, 0,15) compositions are presented in Fig.4.5. Consistent with the observed surface morphology, the XRD profiles for $x = 0$ and 0.15 exhibit peaks corresponding to the primary XA phase along with an additional phase, identified as the β-Mn phase. Interestingly, despite the uniform appearance in backscattered electron microscopy, the XRD pattern for $x = 0.1$ reveals a single minor extra peak at approximately 43.44°. Rietveld refinement of the XRD patterns was performed for all three $Mn_2FeSi_{1-x}Al_x$ compositions, considering two structural phases: the primary XA-ordered Heusler phase and a secondary β-Mn phase. The β-Mn phase consists of a 20-atom unit cell with atoms occupying two distinct crystallographic sites: $8c$ (0.06361, 0.06361, 0.063610) and $12d$ (0.125, 0.20224, 0.45224). It has a

lattice constant of 6.24 Å [64]. Building on the earlier EDX analysis, the Si-deficient composition is attributed to the β-Mn phase. After Rietveld refinement, the calculated lattice parameters for the primary XA phase are 5.678 Åfor $x = 0$, 5.681 Åfor $x = 0.1$, and 5.693 Åfor $x = 0.1$. The proportion of the secondary β-Mn phase relative to the XA phase is 17.63 % for $x = 0$, decreases to less than 2% for $x = 0.1$, and then rises to 8.27% for $x = 0.15$. Notably, the minimal presence of the secondary phase in $x = 0.1$ suggests that this composition is close to an ideal single-phase XA-type Mn$_2$FeSi. Hence, the rest of the study focuses on the $x = 0.1$ composition results.
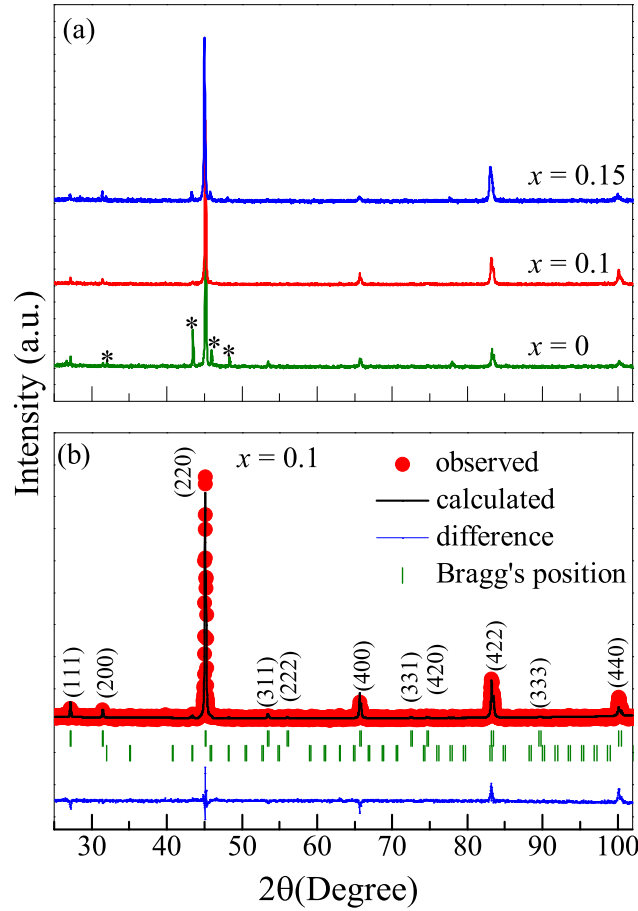
Figure 4.5: (a) XRD profile for Mn$_2$FeSi$_{1-x}$Al$_x$ ($x = 0, 0.10, 0.15$). Peaks marked with (*) are due to the secondary β - Mn phase. (b) Rietveld refined XRD pattern of $x = 0.1$

Next, a qualitative analysis of antisite disorder is conducted by ex-

amining the intensities of the superlattice reflections in the XRD patterns. In a typical X_2YZ Heusler system, the structure factors for the superlattice reflections (111), (200), and the main reflection (220) are determined using the following expression:

$$F(111) = 4|f_Y - f_X|$$

$$F(200) = 4|2f_X - (f_Y + f_Z)|$$

$$F(220) = 4|2f_X + (f_Y + f_Z)|$$

Any disorder in the site occupancy hence affects the intensity of superlattice reflections vis-á-vis the (220) main peak [12]. From the current XRD profiles, the intensity ratios $A_{exp} = I_{200/220}$ and $B_{exp} = I_{111/220}$ are obtained for each composition and used in the expression for the order parameters, $S^2 = A_{exp}/A_{Th}$ and $S^2(1 - 2\alpha)^2 = B_{exp}/B_{Th}$; the subscript 'Th' refers to the corresponding theoretical values, expected for a perfectly ordered system. A complete $B2$ - type disorder is characterized by $S = 1$ and $\alpha = 0.5$ [65, 66]. In the case of $x = 0.1$, S is 0.9 and $\alpha = 0.14$, indicating a partial $B2$-type antisite disorder within the main XA phase [65, 67]. In other words, the $x = 0.1$ is likely to have a partial swapping between Fe-Si/Al atoms.

4.2.4 Magnetic Properties

The Temperature- and magnetic field-dependent magnetization measurements were performed for all three compositions, as shown in Fig.4.6. The magnetization M(T) was recorded in a 0.01 T magnetic field over a temperature range of 5 K to 350 K using zero-field-cooled (ZFC) field-cooled (FC) protocols. All compositions exhibit antiferromagnetic ordering below the Néel temperature, $T_N \sim 50$ K. Notably, thermo-magnetic irreversibility between the ZFC and FC curves is observed well above T_N, which can be attributed to various factors, including short-range ferromagnetic (FM)

correlations, magnetocrystalline anisotropy, and competing FM-AFM interactions [68]. Given that the $x = 0$ and 0.15 compositions contain a significant fraction of the magnetic β-Mn phase, isolating the intrinsic magnetic properties of the XA phase in Mn$_2$FeSi is challenging. Therefore, further analysis focuses only on the magnetization data for the $x = 0.1$ composition, which contains less than 2% of the β-Mn phase.
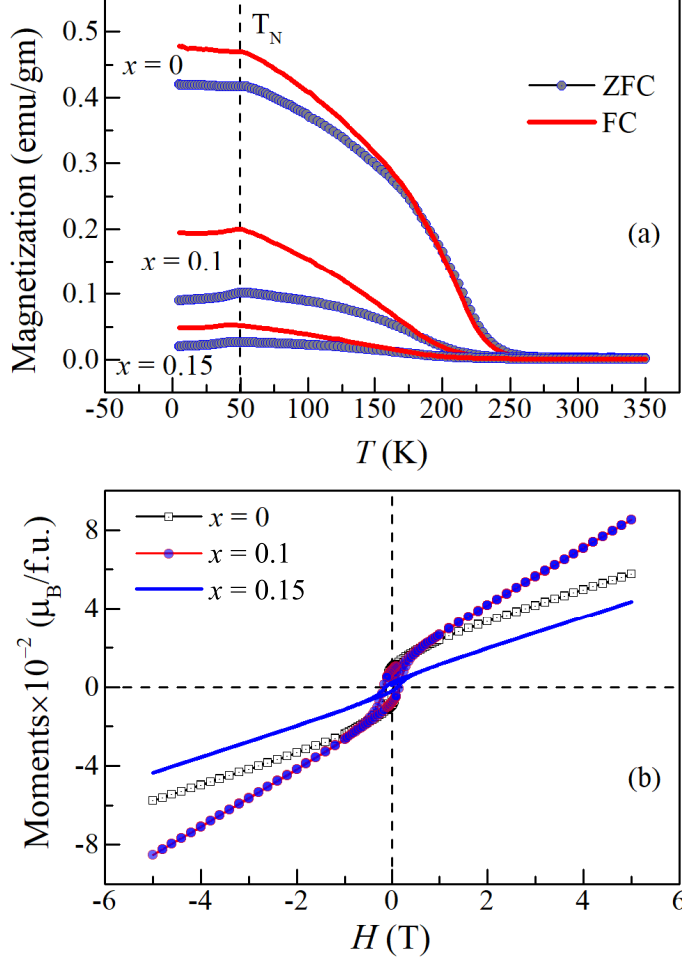
Figure 4.6: (a) Temperature dependence of the magnetization measured at an applied magnetic field of 0.01 T, and (b) Magnetization as a function of the applied field, at 5 K.

Further, Fig.4.7(b) shows the inverse dc susceptibility (χ^{-1} vs T) of $x = 0.1$, fitted with the Curie-Weiss law, $\chi = $ C/(T - θ) in the region between 260 K to 350 K. The fitting yields a negative θ (= -176.91 K) value, congruent with the low-temperature AFM order. Since $\theta >> $ T$_N$ and a sizable bifurcation exist between the ZFC and FC magnetization, the

composition is magnetically frustrated [26] due to the competing magnetic interactions. While Curie-Weiss fitting can be used to estimate the paramagnetic moment, which provides insight into the magnetic elements in the material, this correlation becomes complex in multi-component magnetic intermetallics like Heusler alloys. Strong hybridization between atomic orbitals significantly influences magnetic interactions, making it difficult to directly associate the total moment with individual elemental contributions. Additionally, Mn_2FeSi is susceptible to antisite disorder, further impacting its overall magnetic behavior. Consequently, we refrain from extracting the paramagnetic moment from the present Curie-Weiss fit.
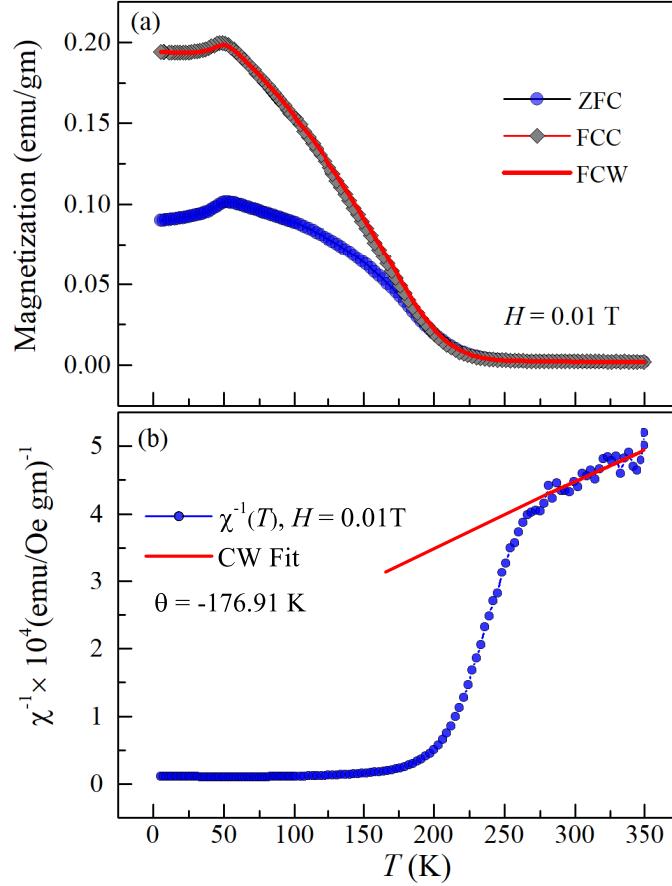
Figure 4.7: (a) M(T) curve measured at 0.01 T (in the inset, at H = 0.05 T), and (b) Curie-Weiss fitting of χ^{-1} vs T curve (at H = 0.01 T) of $x = 0.1$

It can be seen in Fig.4.7(b) that below 260 K, a distinct deviation from linearity is observed in χ^{-1}. This knee-like downturn also softens with

increasing magnetic field, as illustrated in Fig. 4.8(a). Such deviations from Curie-Weiss behavior, occurring well above the long-range magnetic transition temperature, have previously been linked to the presence of a Griffiths phase in various materials [25, 69–71]. The Griffiths phase (GP) is characterized by the emergence of ferromagnetic short-range ordering within a predominantly paramagnetic matrix, persisting up to a characteristic temperature, T_G. Beyond T_G, the material transitions into a purely paramagnetic state. In high magnetic fields, these short-range FM clusters are masked by a linear increase of the paramagnetic contribution to the susceptibility.
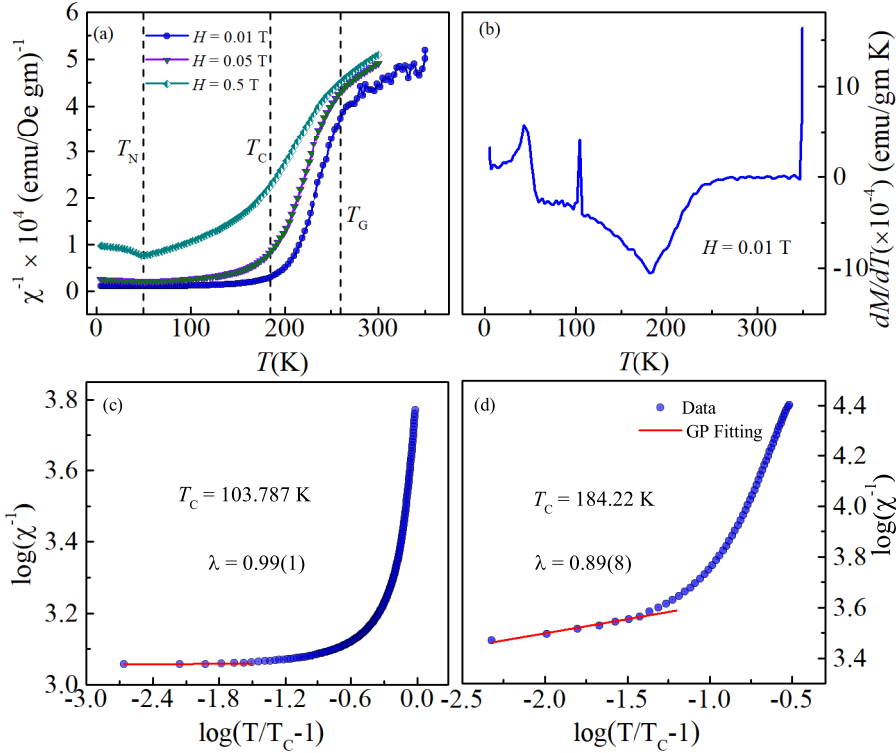
Figure 4.8: (a) χ^{-1} vs T of $x = 0.1$ measured at H = 0.01, 0.05, and 0.5 T. (b) dM/dT, and (c,d) Power law fitting (see text for details).

In the Griffiths phase, the inverse susceptibility obeys a power law given by $\chi^{-1} \propto (T - T_C)^{(1-\lambda)}$, where $0 < \lambda < 1$, for $T_C < T < T_G$. Here, T_C is the critical temperature, and λ represents the deviation from CW law [72–75]. Estimating the value of T_C in such a system is complicated. A workable solution is to fit the power law in the temperature range where

a maximum change in slope of the dM/dT curve occurs [76]. Thus, the power law in the present case can be fitted with T_C = 103.22 K or 184.86 K, as presented in Fig4.8(b-d). Fixing the value of T_C = 184.68 K yields a better fit with λ = 0.90(5), which matches the values observed in other Heusler alloys [25, 27]. A value of λ close to unity in the GP regime and significant divergence between T_N and T_C denotes the resilience of this unique magnetic phase in the $x = 0.1$ composition.

Further insight into the origin of the Griffiths phase (GP) in the $x = 0.1$ composition is gained from the field-dependent magnetization plots shown in Fig.4.9(a). A pronounced hysteresis loop is observed at low fields, which transitions into a linear M(H) behavior at higher fields—an indication of ferromagnetic correlations coexisting within an antiferromagnetic (AFM) background. Notably, this magnetic ordering persists even at 100 K, well above T_N. The Arrot plots at 5 K and 100 K (see Fig.4.9(b)) exhibit quasi-linear behavior at higher H/M values, with no positive intercept on the M^2 axis. The absence of spontaneous magnetization, even at 5 K, further highlights the dominance of competing magnetic interactions in this system.

Having confirmed the presence of Griffiths phase in $x = 0.1$, temperature-dependent AC susceptibility (χ_{ac}) measurements were recorded in the temperature range 10 K to 150 K. Fig.4.10 presents the real component of $\chi_{ac}(T)$ at various frequencies. The peak corresponding to the antiferromagnetic (AFM) ordering temperature, T_N, remains unchanged with varying frequencies, indicating the non-glassy nature of this magnetic phase. In contrast, a second peak observed around 130 K originates from the short-range magnetic correlations associated with the Griffiths phase. This feature diminishes with increasing frequency, further supporting its correlation with the GP [77].

In magnetic materials, the Griffiths phase (GP) often arises due to factors such as phase separation, quenched disorder, cluster formation, and competing magnetic interactions, particularly in quasi-two-dimensional
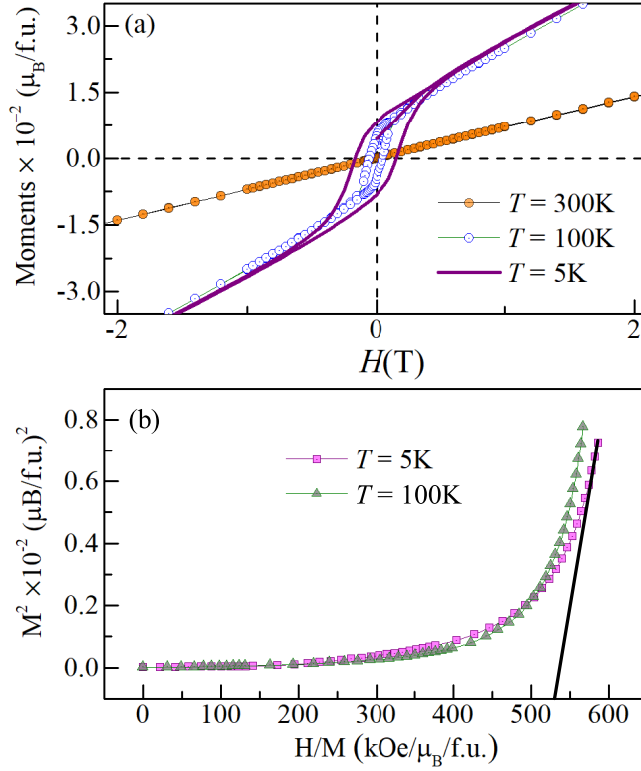
Figure 4.9: (a) Isothermal M(H) at different temperatures, and (b) Arrot plot of $x = 0.1$
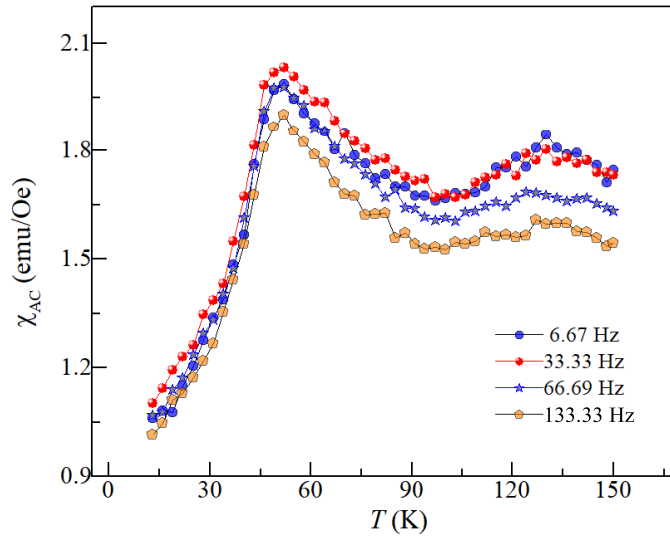
Figure 4.10: Frequency dependence of $\chi_{AC}(T)$ for $x = 0.1$

systems. In the current case, The $x = 0.1$ composition crystallizes into a stable cubic inverse Heusler structure, which remains resistant to structural phase transitions even at low temperatures. This stability suggests

that structural instability is not the driving factor behind the emergence of GP in $x = 0.1$. Instead, in the XA phase of this composition, the two Mn atoms occupy inequivalent positions, resulting in varying bond distances with Fe atoms. Given that the magnetic interactions in this system follow the Ruderman-Kittel-Kasuya-Yosida (RKKY) mechanism, these variations in bond distances lead to competing magnetic interactions, contributing to the GP behavior. Additionally, as discussed in the preceding section, electronic structure calculations highlight the influence of antisite disorder on the total magnetic moment of this material. Therefore, antisite disorder is also a significant factor in the development of GP in the $x = 0.1$ composition.

All earlier experimental attempts to obtain stoichiometric Mn_2FeSi resulted in the formation of multi-phasic structures. As per our theoretical calculations, $B2$-type disorder (configuration E) exhibits a small value of the total magnetic moment but has a higher relative formation energy. Thus, the present experimental endeavor to substitute a small amount of Si with Al seems to relax the lattice as well as its competing magnetic interactions, which are together conducive for crystallizing the XA phase (with a minimal $< 2\%$ secondary phase) and a partial $B2$-type antisite disorder contributes towards its reduced total magnetic moment.

4.3 Conclusion

Through first-principles studies, we investigate the influence of different types of disorder on the electronic and magnetic properties of Mn_2FeSi. Our calculations revealed that swapping elements amongst their Wyckoff positions leads to significant alterations in the total magnetic moment and a reduction in spin polarization. Additionally, an analysis of the Heisenberg exchange coupling parameter indicates the presence of competing interactions between the two inequivalent Mn sites and the Fe sublattice. We also complement our calculations with an experimental study, wherein we successfully prepare a phase-pure Mn_2FeSi by substituting 10% Al at the Si

site. This study represents the first successful synthesis and characterization of cubic Heusler Mn_2FeSi, providing valuable insights into its magnetic properties. Apart from confirming the long-range AFM ordering with an Néel temperature of around 50 K, the temperature and field-dependent magnetization measurements help identify a Griffiths phase across a broad temperature range much higher than the Néel temperature. In conclusion, this study provides valuable insights into the electronic and magnetic properties of the XA phase of the cubic Mn_2FeSi Heusler system.

.

Chapter 5

Observation of Kondo-like transport and wandering axis ferromagnetism in Mn substituted $Fe_2Ti_{1-x}Mn_xSn$

5.1 Overview

This chapter explores the impact of Mn substitution on the electronic, magnetic, and transport properties of $Fe_2Ti_{1-x}Mn_xSn$. First-principles calculations reveal a spin-polarized density of states upon Mn doping. Resistivity and magneto-transport measurements indicate Kondo-like scattering at low temperatures and a linear negative temperature coefficient at higher temperatures, supported by specific heat data. Magnetization studies suggest a ferromagnetic ground state with a wandering axis and weak anisotropy. XRD confirms a highly ordered cubic structure with reduced disorder, while XAFS reveals local distortions around Mn, contributing to random anisotropy. These findings shed light on the emergence of a spin-polarized band structure and a unique magnetic ground state in Mn-substituted $Fe_2Ti_{1-x}Mn_xSn$, offering new insights into spintronic materials.
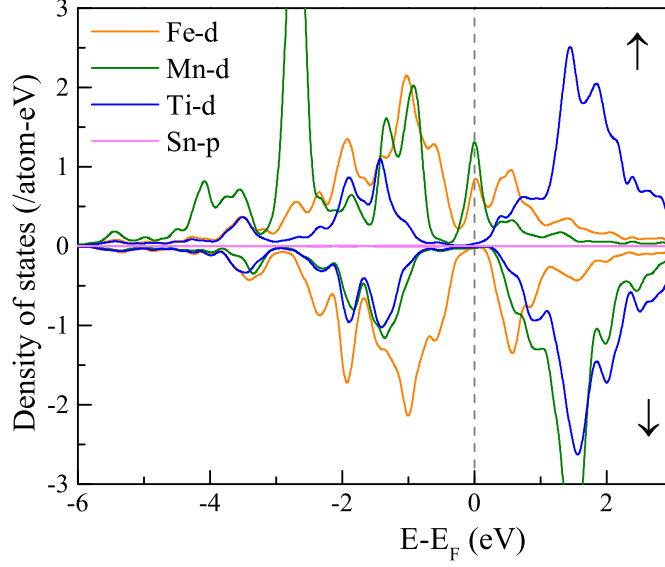
Figure 5.1: Atom-projected spin-polarized density of states for Fe, Mn, and Ti -d and Sn p orbitals in $Fe_2Ti_{0.75}Mn_{0.25}Sn$ in the ferromagnetic arrangements.

5.2 Results and Discussion

5.2.1 Density of states and crystal structure

The density of states (DOS) of the $Fe_2Ti_{1-x}Mn_xSn$ is calculated using a DFT-only approach. For this case, the atom-projected spin-polarized DOS of Fe, Mn, Ti -d and Sn p states are shown in Fig.5.1. Many insightful observations can be made from this plot. First, the system shows the half-metallic character of the DOS with mainly Fe and Mn d states in the spin-up channel, while there is a band gap in the spin-down channel at the Fermi level. Though Ti d states also contribute below the Fermi level, the dominant contributors remain the d states of Fe and Mn atoms, and the magnetic properties arise from the interactions among all three transition metal atoms. Second, this interaction can be considered itinerant as the system is metallic. Third, the magnetic moment on the Mn site is large, while Fe and Ti atoms carry negligible moments, and both Mn & Fe have finite contributions to the DOS at the Fermi level. Recall that we
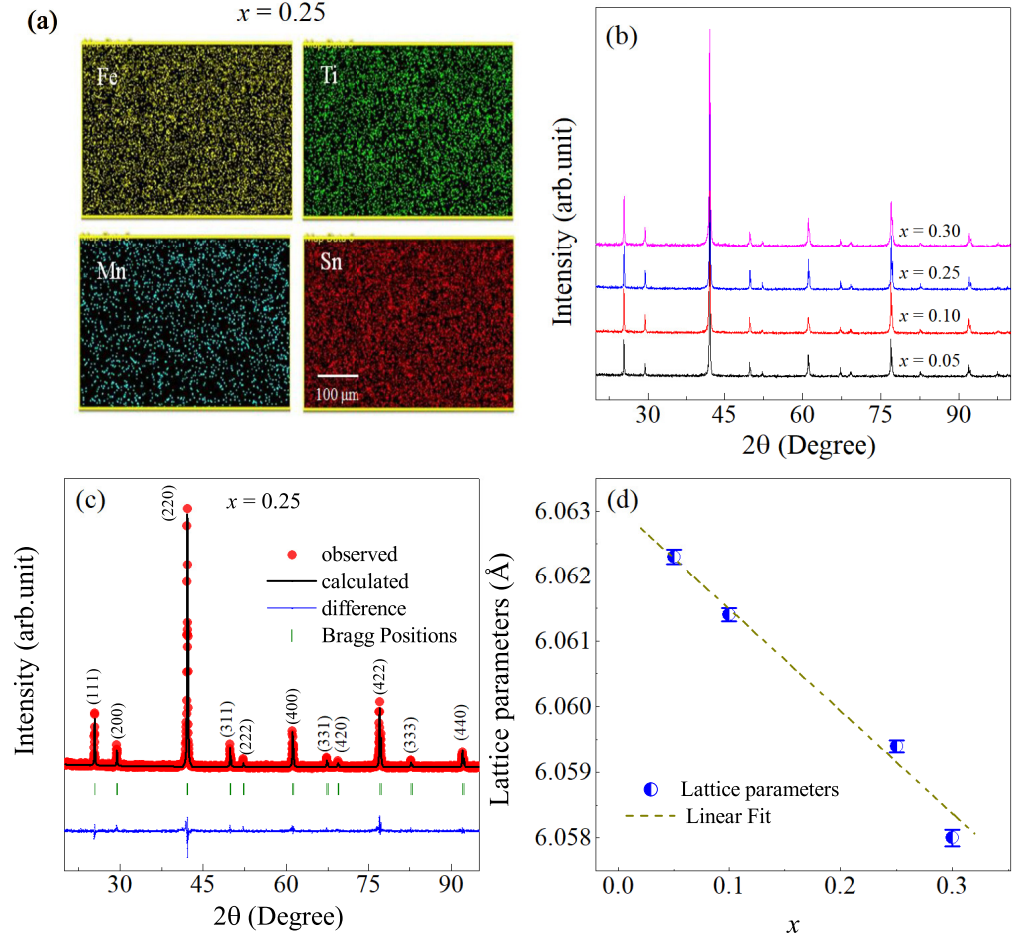
Figure 5.2: (a) The elemental mapping results of $x = 0.25$. The figures are presented at a scale of 100 μm. (b) X-ray diffraction profile of $Fe_2Ti_{1-x}Mn_xSn$, (c) the Rietveld refined XRD profile of $x = 0.25$, and (d) shows the variation of lattice parameter with varying Mn concentration.

started with a scenario of antiferromagnetic coupling between single Mn and eight (ferromagnetically aligned) Fe atoms. Such a system converges to a ferromagnetic coupling among all the magnetic atoms, with negligibly small magnetic moments on Fe (~ 0.016 μ_B) and Ti (~ 0.052 μ_B) atoms and a relatively high moment on Mn (~ 3.161 μ_B) atoms. It appears as if Mn atoms are the ones with localized moments that are interacting through the cloud of conduction electrons formed by Fe and Ti atoms.

Further, to explore the effect of Mn substitution on structural, transport, and magnetic properties of Fe_2TiSn, we begin the experimental investigation into the Mn–substituted Fe_2TiSn compounds. Table.5.1 shows the

Table 5.1: Atomic percentages, parameters determining goodness of fit and magnetic transition temperatures of $Fe_2Ti_{1-x}Mn_xSn$.

x	Atomic %				goodness of fit			T_C	T_S
	Fe	Ti	Mn	Sn	R_{Bragg}	R_F	χ^2	(K)	(K)
0.05	48.05	24.51	1.23	26.21	8.12	10.1	1.94	< 5	250
0.10	48.29	22.76	2.55	26.27	8.44	6.49	2.51	6	268
0.25	48.0	19.55	6.25	26.13	9.68	7.86	2.77	18	320
0.30	47.91	18.10	7.40	26.60	10.7	9.09	2.02	25	325

atomic percentage of Fe, Ti, Mn, and Sn after EDX analysis, and Fig.5.2(a) shows the elemental mapping for $x = 0.25$. The EDX results confirm the formation of stoichiometric compositions with a uniform distribution of each element. The X-ray diffraction (XRD) patterns of $Fe_2Ti_{1-x}Mn_xSn$ ($x = 0.05, 0.1, 0.25,$ and 0.3) are shown in Fig.5.2(b). The presence of strong (111), (200), and (220) peaks confirm the highly ordered cubic $L2_1$ crystal structure in all the prepared compositions. However, the solubility limit of Mn in Fe_2TiSn is limited to 30% as additional peaks related to the secondary phase begin to appear for compositions with $x \geq 0.4$ (not shown here). Contrary to the general expectation of finding an increase in the antisite disorder upon carrying out substitutions in an intermetallic system, the present compositions show a relative increase in the intensity of the (111) and (200) super-lattice peaks, indicating a reduction of the overall disorder in comparison to pristine Fe_2TiSn. Rietveld refinement of the XRD profiles, implemented through the FullProf suite [53], yield values for lattice parameters that follow Vegard's law [78], indicating the desired substitutions at the targeted lattice sites have indeed been achieved.

5.2.2 Electrical resistivity

With the prediction of half-metallic DOS at the Fermi level and a highly ordered crystal structure, studying the electrical resistivity of the Mn-
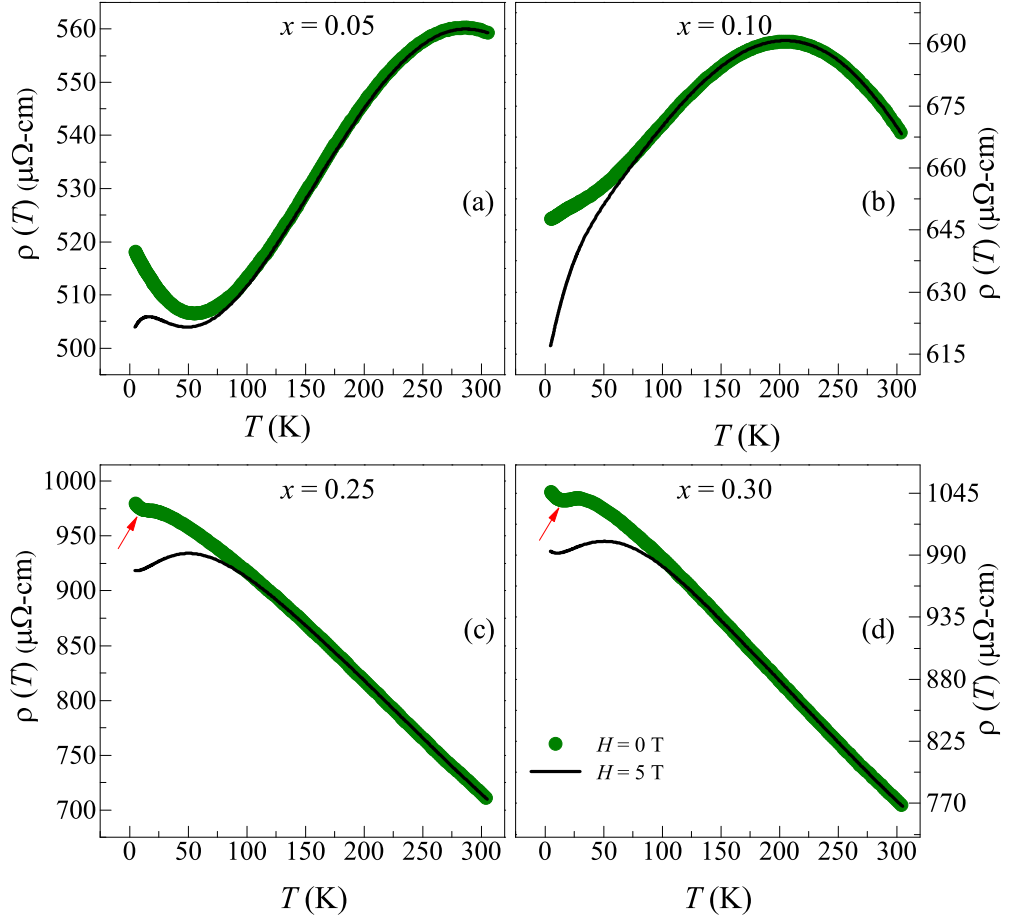
Figure 5.3: Temperature dependent electrical resistivity of $Fe_2Ti_{1-x}Mn_xSn$ measured at an applied magnetic field of 0 T and 5 T.

substituted Fe_2TiSn compounds becomes pertinent. It has been previously observed that the electrical resistivity, $\rho(T)$, of Fe_2TiSn shows a bad metallic behavior with a low-temperature upturn and minimum at 50 K. This low-temperature upturn in $\rho(T)$ is due to weak localization caused by anti-site disorder between the Fe and Ti sites. Fig.5.3 shows the $\rho(T)$ data for $Fe_2Ti_{1-x}Mn_xSn$ ($x = 0.05, 0.10, 0.25, 0.30$) for a temperature range of 5–300 K and at applied magnetic fields of 0 T and 5 T. Fe_2TiSn is inherently a p-type system, indicating hole-dominated transport. When Mn is substituted in place of Ti, we are effectively introducing additional electrons into the system. As a result, these electrons tend to compensate for the existing holes, reducing carrier density. This decrease in carrier density manifests as an increase in electrical resistivity rather than a conventional metallic behavior expected from electron doping. The general features of

Table 5.2: The extracted parameters after fitting the $\rho(T)$ data in low-temperature regions for the applied fields of 0 and 5 T.

x	ρ_0		$\rho_e \times 10^{-2}$		$\rho_K \times 10^{-2}$		$\rho_p \times 10^{-9}$	
	0 T	5 T	0 T	5 T	0 T	5 T	0 T	5 T
0.25	1.389	1.292	0.67	1.20	1.89	1.7	1.239	0.73
0.30	1.376	1.297	1.01	1.24	2.5	1.9	0.397	0.135

$\rho(T)$ curve of $x = 0.05$ sample match that of Fe_2TiSn [67]. However, when viewed from the high-temperature side of the $\rho(T)$ curve for $x = 0.10$, it shows a negative temperature coefficient of resistance (TCR) down to 200 K, followed by positive TCR at low temperatures. On the other hand, $x = 0.25$ and 0.30 compositions exhibit complete negative TCR throughout the measurement range. A closer inspection reveals that the $\rho(T)$ of $x = 0.25$ and 0.30 shows a weak slope change at low temperature, below which $\rho(T)$ increases at a faster rate with decreasing temperature.

The low-temperature data is analyzed by considering the different scattering mechanisms that may contribute to the observed $\rho(T)$ behavior. A low-T upturn in resistivity can result from various mechanisms, including electron-electron interaction (EEI), weak localization (WL), and Kondo-like transport. EEI arises from electron-electron elastic scattering due to the Coulomb interaction between conduction electrons, WL arises from disorder-mediated coherent backscattering of charge carriers, and Kondo-like transport arises from the interaction between the localized magnetic moment associated with the magnetic impurities and mobile conduction electrons [79, 80]. In Mn-substituted Fe_2TiSn, a reduction in atomic disorder and/or magnetic order destroys the WL, suggesting that the low-T upturn of $\rho(T)$ in compositions with higher Mn concentration is not caused by WL [67, 81]. Furthermore, separate fits to the $\rho(T)$ data with EEI and Kondo effect confirm that neither model fits the experimental data independently. Thus, combining both mechanisms likely contributes
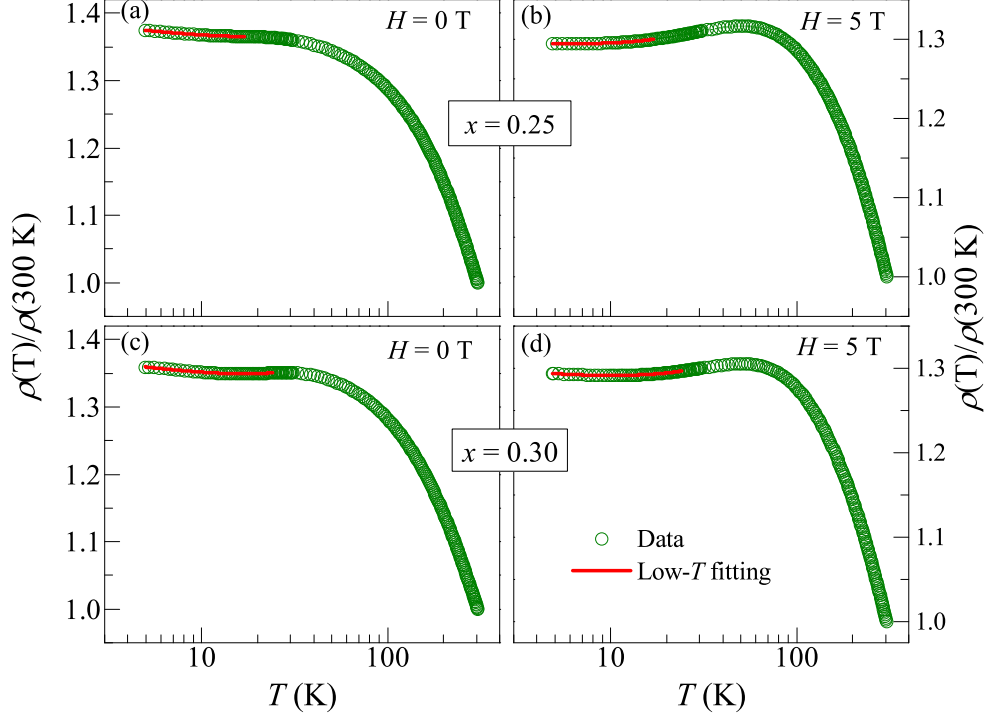
Figure 5.4: (a)-(d) shows the fitting of temperature-dependent resistivity data of $x = 0.25$ and 0.30 at 0 T and 5 T, respectively. The temperature axis is represented on a log scale for better visibility of the low-T fitting.

to the observed low-T upturn in resistivity. Besides, the contribution from electron-phonon scattering should also be added to the form T^5 to represent the resistivity [18]. Thus, the low-T resistivity data at $H = 0$ T and 5 T can be described by the expression

$$\rho(T) = \rho_0 + \rho_e T^{1/2} - \rho_K ln(T) + \rho_p T^5$$

, where, ρ_0 is residual resistivity, and, ρ_e, ρ_K and ρ_p represent coefficients for EEI, Kondo-like transport and electron-phonon scattering respectively. The fitting result is shown in Fig.5.4, and the fitting parameters for different Mn substitution and applied magnetic field are depicted in Table-5.2. It is evident from the Table.5.2 that, both, ρ_e and ρ_K increase with increasing x. Further, the value of ρ_K (i) is higher than ρ_e, and (ii) is higher at $H = 0$ T compared to 5 T for a given composition. This highlights the dominant role of Kondo-like scattering of charge carriers in $Fe_2Ti_{1-x}Mn_xSn$ for $x \geq$ 0.25 compared to EEI.

Next, we analyze the $\rho(T)$ behavior of $x = 0.25$ (and 0.30) composition in the high-T region. While the negative TCR has been observed in Heusler compounds [8, 49, 82–84], the notable feature here is the linear $\rho(T)$ between 100 K and 300 K, which is unusual compared to the common semiconductor and disordered metallic systems. In semiconductors, electron transport exhibits a thermally activated behavior of $\rho(T)$ data where ρ vs T plot is upward convex. On the contrary, disordered metallic systems show a convex downward behavior of $\rho(T)$ data. Further, reports on the high-T resistivity data of Fe$_2$TiSn show a negative TCR from 300 K to 800 K, which is attributed to the interband transition of conduction electrons through a gap at Fermi level [85]. With electron doping in pristine Fe$_2$TiSn, this negative TCR persists below 300 K [86] and may also result in half-metallicity [87, 88]. A similar signature is observed in the present Fe$_2$Ti$_{1-x}$Mn$_x$Sn compositions. Thus, the combined results of theoretical calculations and electrical resistivity strongly suggest the presence of half metallicity in Mn-substituted Fe$_2$TiSn.

Fig.5.5 shows the isothermal magneto-resistance (MR) curves measured at different temperatures ranging from 5 K $\leq T \leq$ 300 K and for all four compositions. Using the standard definition of MR as, $MR(\%) = \left[\frac{\rho(H)-\rho(0)}{\rho(0)}\right] \times 100$, we find that all the Mn–substituted compositions show the isotropic negative MR in the entire temperature range. Generally, the field-dependent resistivity, $\rho(T, H)$, depends on the combined sum of Lorentz force and contribution from different scattering mechanisms. The Lorentz force constitutes the classical MR, which is inherently positive. However, the observed small yet negative MR at high temperatures is attributed to the presence of short-range ferromagnetic correlations, as will be discussed later.

Moreover, the increase in the magnitude of MR at low temperatures with increasing Mn content suggests the presence of magnetic ordering and/or spin-dependent scattering. Additionally, compositions showing signatures of half-metallicity, i.e., $x = 0.25$ (and 0.30), exhibit the dominance of the Kondo-like scattering in low-T resistivity. Notably, the EEI
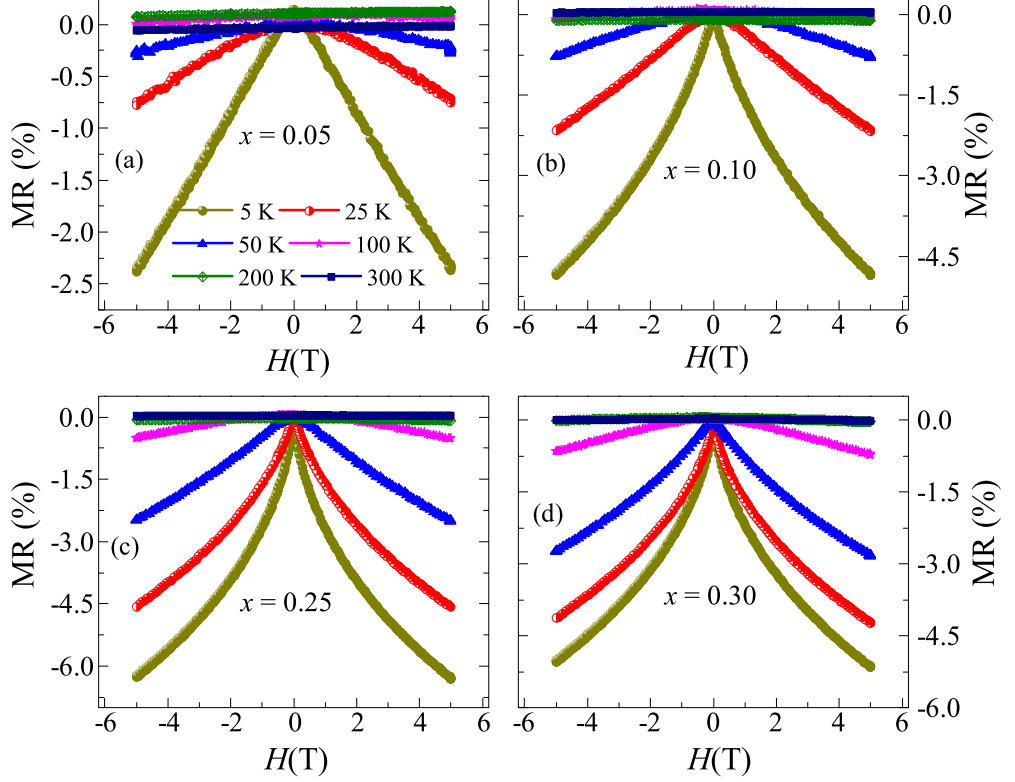
Figure 5.5: Field dependent isothermal magneto-resistance, MR, of $Fe_2Ti_{1-x}Mn_xSn$.

effect leads to a positive MR due to Zeeman splitting and orbital effects, with its magnitude varying as the square root of the applied magnetic field [79, 89–92]. This has been reflected as the increment of ρ_e value with an applied magnetic field of 5 T for a given value of x(see Table-5.2). Conversely, applying the magnetic field suppresses the fluctuation in the localized magnetic moment and spin-dependent scattering, leading to a negative MR in a Kondo system [93]. Thus, for $x = 0.25$ (and 0.30), the negative MR supports that the Kondo effect is the dominant mechanism governing the low-T electrical resistivity. This also explains the higher value of ρ_k compared to the ρ_e obtained from fitting the low-T resistivity data.

5.2.3 Magnetic properties

Having understood the electronic DOS in the $Fe_2Ti_{1-x}Mn_xSn$ compositions and possible half-metallic ground state in $x \geq 0.25$, we now discuss the ex-
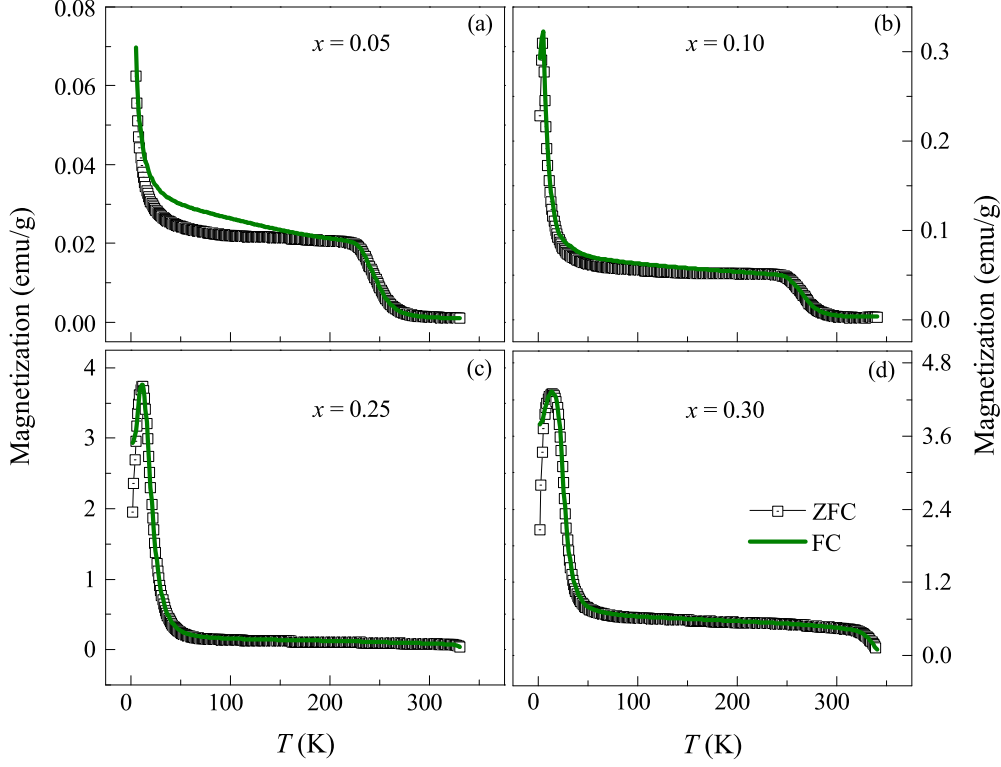
Figure 5.6: Temperature dependence of the magnetization, $M(T)$ curves, of (a) $x = 0.05$, (b) $x = 0.10$, (c) $x = 0.25$, and (d) $x = 0.30$.

perimental study of its magnetic properties. The temperature-dependent magnetization, $M(T)$, measured at $H = 0.01$ T, is plotted in Fig.5.6. According to the previous studies, an inherent Fe-Ti anti-site disorder in the otherwise non-magnetic Fe_2TiSn induces the formation of weak magnetic clusters [67]. These interactions are identified by a step-like feature in the high-temperature region, denoted here as T_S, in the $M(T)$ curve. This step-like feature shifts towards the high-temperature side with rising Mn substitution. Additionally, an abrupt rise in magnetization is observed at low temperatures, marking the transition to a magnetically ordered state. This temperature is identified as T_C, and its value increases with rising Mn content. The values of T_C and T_S are listed in the Table-5.1.

Fig.5.7 shows the magnified view of the $M(T)$ curve for $x = 0.25$, measured at two different applied magnetic fields. At a low applied magnetic field (0.01 T), there is a noticeable contrast between the $M(T)$ plots recorded during the zero field-cooled (ZFC) and field-cooled (FC) pro-
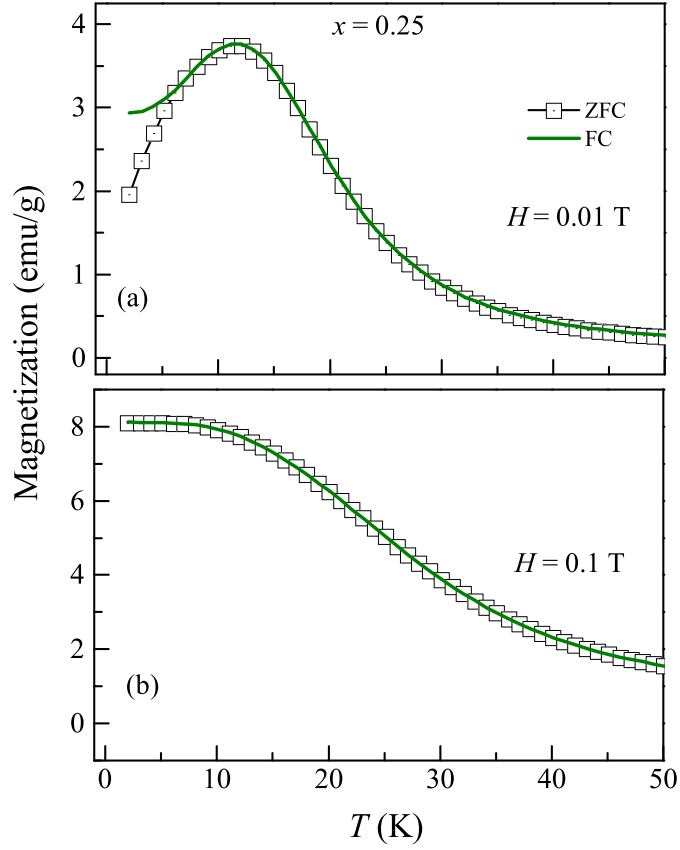
Figure 5.7: Temperature dependence of the magnetization, $M(T)$ curves, of $x = 0.25$ at an applied magnetic field of (a) $H = 0.01$ T, and (b) $H = 0.1$ T.

tocols. This bifurcation between ZFC/ FC disappears when a relatively strong magnetic field of ≥ 0.1 T is applied, suggesting the presence of weak anisotropy in the material. In the ZFC process, the material's anisotropy determines the amount of magnetization below T_C and may prevent a relatively small applied field from aligning the moments in the direction of the field. When the same material is cooled through T_C while being exposed to a magnetic field during the FC process, the moments are locked into the direction of the applied magnetic field. As a result, there is a noticeable contrast between the ZFC and FC curves for small applied fields, and this bifurcation disappears when a slightly stronger magnetic field is applied.

Fig.5.8(a,b) shows the variation of isothermal magnetization (M) as a function of the applied magnetic field (H) for all the compositions measured at 300 K and 5 K, respectively. For $x = 0.05$, the $M(H)$ curve at 300 K
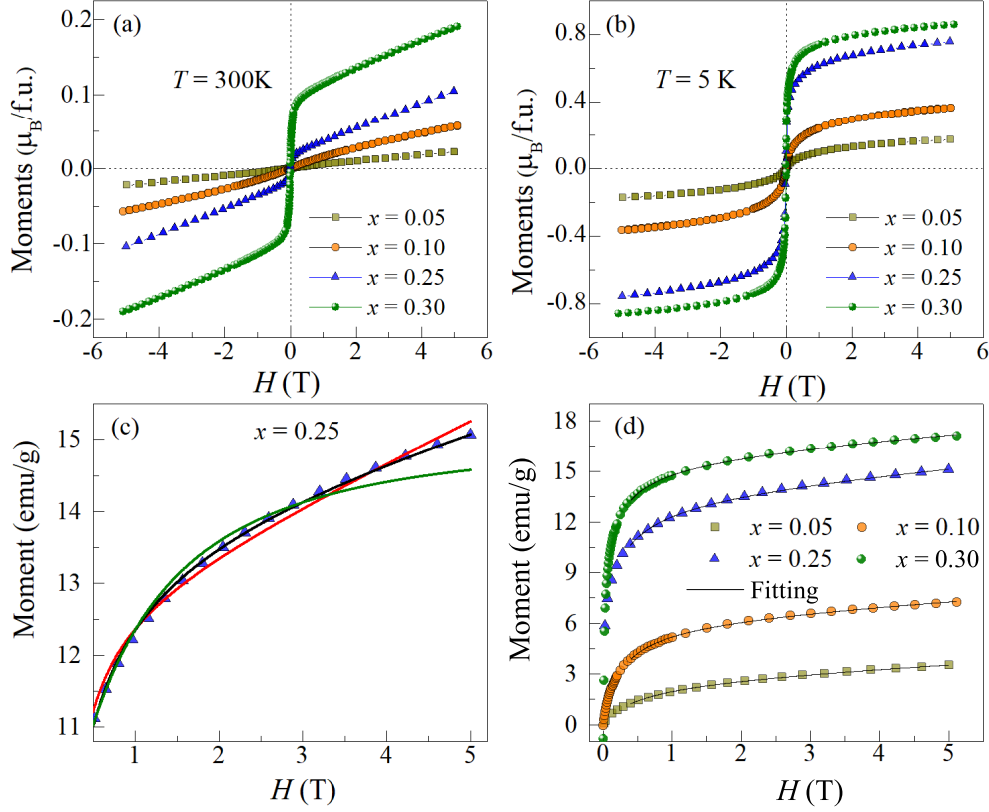
Figure 5.8: Isothermal magnetization, $M(H)$ curve of all the compositions measured at (a) 300 K, (b) 5 K. (c) shows the values of experimental magnetic moment per formula unit at the maximum applied field (M_S) at $T = 5$ K, plotted along with the theoretically predicted Slater-Pauling rule (dotted line) for varying Mn concentration.

displays a linear behavior (Fig.5.8(a)). With increasing x, a sharp rise in M is observed at lower fields, followed by a linear behavior at higher fields, suggesting the presence of short-range ferromagnetic correlations at room temperature. Further, at $T = 5$ K, the $M(H)$ curve shows the characteristics of a ferromagnetic ordering with an increase in the magnetic moment values with x (see Fig.5.8(b)). The value of the experimental magnetic moment per formula unit (M_S) at $H = 5$ T aligns well with the theoretical value predicted by the Slater-Pauling rule. While the $M(H)$ curves do not show complete saturation, this agreement provides strong evidence for a spin-polarized band structure in $Fe_2Ti_{1-x}Mn_xSn$.

Additionally, the presence of ferromagnetic clusters at $T = 300$ K

suggests that the low-temperature magnetization behavior could be solely due to the evolution of these clusters. To interpret this, we have fitted the $M(H)$ curve at 5 K using the modified Langevin function, expressed as $M(H) = M_s L(\alpha) + \chi H$, where $\alpha = \mu H/k_B T$, M_S represents the saturation magnetization, μ is the average magnetic moment and χ represents the paramagnetic susceptibility. The lack of fit of this model to the data (see solid red line in Fig.5.8(c)) rules out any cluster-like evolution in the prepared compositions. Alternatively, it appears that the Mn-substituted Fe_2TiSn compositions display a long-range ferromagnetic order below T_C, which exhibits a substantial dependency on the strength of the applied magnetic field with respect to the random anisotropy. This observation suggests that the weak random anisotropy model [31] could be applicable in describing the low-temperature magnetic properties of these compositions. Such a model has previously been extensively used to explain the FM correlations in Heusler alloys [32, 94, 95]. This model incorporates both the experimentally applied magnetic field and the ground state configuration of magnetic materials with random anisotropy for a wide range of anisotropy strengths. Three distinct regimes can be identified for the weak anisotropy situation based on the magnitude of the applied magnetic field, H, and the parameter H_S $(= H^4{}_r/H^3{}_{ex})$, where H_r and H_{ex} are anisotropic and exchange fields, respectively. For $H < H_S$, one obtains a correlated spin glass phase with a high magnetic susceptibility for low fields. When $H_S < H < H_{ex}$, a ferromagnet with a wandering axis (FMWA) results from a rough alignment of the spins in the presence of a weak magnetic field. The tipping angle of the magnetization vector, with respect to the applied magnetic field, changes throughout the system due to the non-collinear magnetic structure. In this regime, the magnetization approaches saturation as,

$$M(H) = M_s \left[1 - \frac{1}{15} \left(\frac{H_s}{H + H_c} \right)^{\frac{1}{2}} \right] \tag{5.1}$$

where M_s is saturation magnetization, and H_c is the field due to the
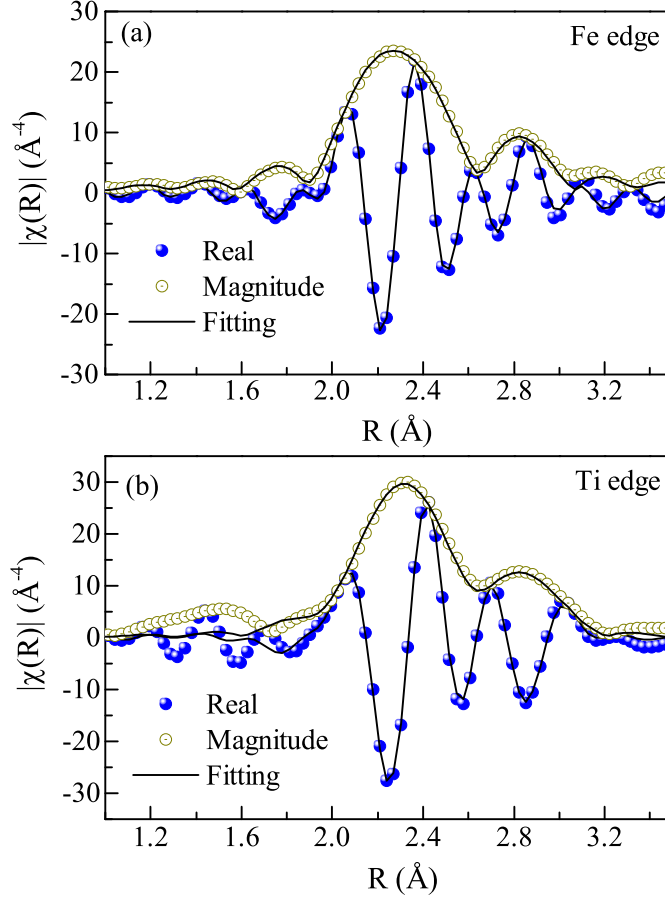
Figure 5.9: Magnitude (hollow spheres) and real component (solid spheres) of Fourier-transformed (a) Fe, and (b) Ti K edge EXAFS spectra at 6 K for $x = 0.25$. See the text for details.

coherent portion of the anisotropy. In the third regime where $H \gg H_S$, the correlation length of the spins reduces as the field strength increases, whereas the tipping angle is completely uncorrelated amongst sites. Except for a slight tipping angle (less than in the case of FMWA) brought on by random anisotropy, all spins in this regime are almost aligned with the field. In such cases, isothermal magnetization gradually approaches saturation as,

$$M(H) = M_s \left[1 - \frac{1}{15} \left(\frac{H_r}{H + H_{ex}} \right)^2 \right] \tag{5.2}$$

We have fitted equation(1) with an additional paramagnetic contribution,χH [33], to the $M(H)$ curve at 5 K of $x = 0.25$, as shown by the solid black line in Fig.5.8(c). It shows a satisfactory fit for a wide

Table 5.3: The coordination number (CN), bond distance (R), and thermal mean square variation (σ^2) from EXAFS data fitting. R_{eff} represents the expected bond distance calculated from the experimental lattice constant.

Bond type	CN	R_{eff}	R(Å)	σ^2(Å^2)
Ti K-edge				
Ti-Fe	8	2.623	2.613(5)	0.00376(38)
Ti-Sn	6	3.029	3.023(9)	0.00543(76)
Fe K-edge				
Fe-Sn	4	2.623	2.621(1)	0.00307(15)
Fe-Ti/Mn	4	2.623	2.596(3)	0.00568(45)
Fe-Fe	6	3.029	3.008(4)	0.00767(43)

range of applied fields from 0.4 to 5 T. The value of H_s derived after the fitting ranges from 0.303 T for $x = 0.05$ to 0.021 T for $x = 0.30$, which is lower than the maximum applied field, following the condition for the system to fall in the second regime. In contrast, equation(2) does not yield a good fit to the data (see the solid green line in Fig.5.8(c), and the value of H_s derived after the fitting is much higher than the maximum applied field despite using the prefactor equal to 1 instead of 1/15 [94]. Thus, the magnetic properties confirm that the low-T magnetic ground state can be well described by the random anisotropy model, with a ferromagnetic-like ordering present below T_C, particularly for $x \geq 0.25$. Although the $M(H)$ curve at $T = 5$ K does not saturate even under an applied magnetic field of 5 T, the experimental magnetization (M_S) reaches its maximum theoretical value (M_{SP}) predicted by the Slater-Pauling rule. Achieving M_{SP} would require complete ferromagnetic ordering, which is inconsistent with the wandering axis ferromagnet scenario. Additionally, while the primary contribution arises from the intrinsic magnetic structure, the possible influence of high-temperature superparamagnetic clusters on the low-temperature $M(H)$ curve can not be entirely ruled out.

Random anisotropy in cubic systems can occur from substitutional impurities and disorder [34]. In Ref. [33], P.M. Gehring *et al.* propose that the random anisotropy in cubic polycrystalline $Dy_{1-x}Y_xAl_2$ could originate from lowering of local lattice symmetry, driven by lattice mismatch, difference in charge screening, and spin-orbit interactions [33]. In certain cubic Heusler systems, such random anisotropy is found to influence their low-temperature magnetic properties [32]. To unravel the reason that the random anisotropy in our cubic $Fe_2Ti_{1-x}Mn_xSn$ originates from local lattice distortion, we undertake measurement of the high-resolution synchrotron-based EXAFS spectra at Fe and Ti K-edges for $x = 0.25$. The EXAFS data is extracted in the reciprocal space, $\chi(k)$, and Fourier transformed to real space, $\chi(R)$, where the magnitude and real part of $\chi(R)$ reflect the radial distribution function around the absorbing atoms. The local structural refinement is carried out by varying the atomic distances and thermal mean square factor (σ^2) until a good fit is obtained in the range of 1.8–3.0 Å in the R space and 3 to 14 Å^{-1} in k space. Based on the information extracted from the XRD profile of the cubic $L2_1$ structure and lattice constant of 6.059 Å , the local atomic arrangement around the Fe atom has 4 Ti and 4 Sn atoms at an equal distance of $\sim$ 2.623 Å, and 6 Fe atoms at $\sim$ 3.029 Å. Similarly, for the Ti atom, there are 8 Fe atoms at $\sim$ 2.623 Å and 6 Sn atoms at $\sim$ 3.029 Å. Given its cubic symmetry, all these bond distances can be represented as a multiple of the lattice constant, and, in principle, only varying the lattice constant should give a good fit. However, this model does not fit the experimental data satisfactorily. Whereas a better fit is achieved by independently varying the individual bond distances, as shown in Fig.5.9, and the obtained fitting parameters are listed in Table-5.3. The notable aspect is the Fe–Ti bond distance discrepancy when viewed separately from the Fe and Ti edges. From the Ti-edge, the Ti–Fe bond distance comes out to be $\sim$2.613 Å, consistent with the value derived from the lattice constant, whereas the same bond distance, when viewed from the Fe edge, yields a value of 2.596 Å. Furthermore, the Fe–Sn bond distance observed from the Fe-edge is 2.621 Å, which aligns well
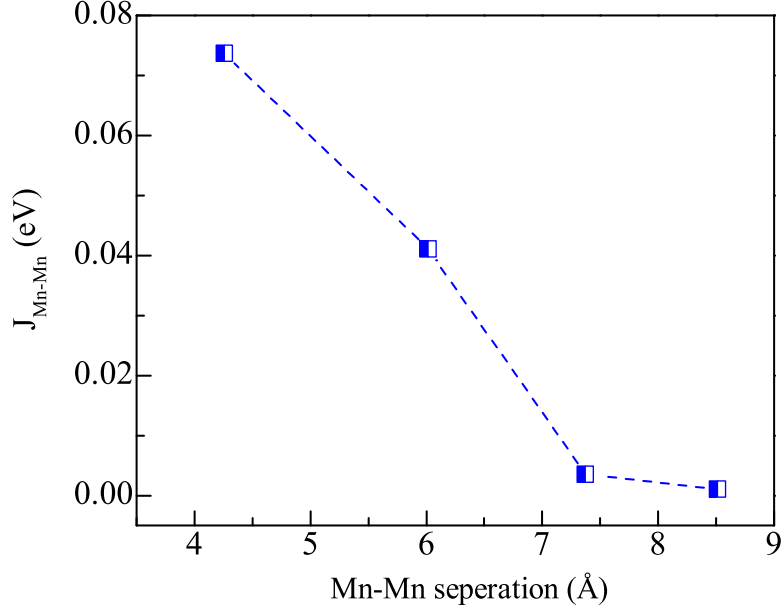
Figure 5.10: Mn-Mn magnetic interaction at various separations in the unit cell of $x = 0.25$. For details, refer to the "Experimental and computational details" section.

with the lattice constant. This observation contradicts the expectations of the cubic symmetry, where Fe–Ti and Fe–Sn bond distances should be equidistant from the Fe atom. This discrepancy in the Fe–Ti correlation comes from the fact that Mn replaces some Ti atoms in $Fe_2Ti_{1-x}Mn_xSn$ compositions, and the bond distance involving the Ti site represents an average distance of Fe–Ti and Fe–Mn. This further indicates that in the Fe–(Ti/Mn) correlation, where Mn occupies the vacant Ti sites, the local lattice environment is distorted, leading to variations in the bond distance. These observations confirm that the lowering of local symmetry causes the random anisotropy in $Fe_2Ti_{1-x}Mn_xSn$ compositions.

Thus, the analysis of *ab initio* DOS calculation, resistivity, and magnetic data suggests that Mn substitution in Fe_2TiSn introduces localized moments. These local moments exhibit strong coupling with the conduction electron, which screens the interaction between two Mn atoms. As the results of this screening, the strength of the magnetic interaction decreases with increasing Mn-Mn distance, and the typical ferromagnetic order is absent in $Fe_2Ti_{1-x}Mn_xSn$. To verify this, we calculated the
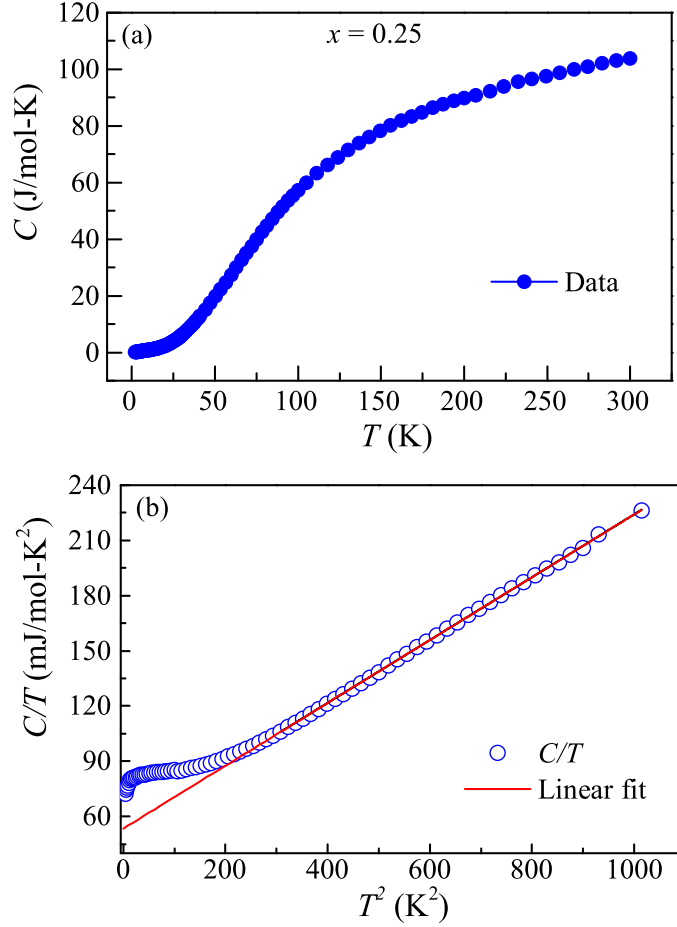
Figure 5.11: (Color online) (a) The temperature variation of specific heat of $x = 0.25$ at an applied field of 0 T, and (b) the specific-heat data in the form C/T versus T^2, along with the linear fit to the experimental data from high temperature to magnetic transition temperature (T_C).

distance-dependent magnetic exchange interaction (J_{Mn-Mn}) between two Mn atoms. Estimating distance-dependent Mn-Mn magnetic interaction with smaller unit cells (considered for 25% substitution) is difficult. This is because, at large Mn-Mn separation in a small unit cell, contributions from the periodic images of Mn atoms at relatively shorter distances will start contributing to the magnetic energy. To avoid this problem, one has to consider a large supercell. We consider a 2×2×2 supercell and replace two Ti atoms with Mn atoms. The distance-dependent Mn-Mn magnetic interaction ($\mathrm{J}_{Mn-Mn} = \mathrm{E}_{AFM}$-$\mathrm{E}_{FM}$) is then estimated as explained in the "Experimental and Computational details" section. Here, we take advan-

tage of the fact that the magnetic moments on Fe and Ti atoms are negligibly small, and hence, their insignificant direct contributions to J_{Mn-Mn} can safely be ignored. The plot of separation dependent J_{Mn-Mn} is shown in Fig. 5.10. One can observe that the effective Mn-Mn interaction is ferromagnetic, consistent with the experimental findings. This ferromagnetic interaction exponentially decreases with Mn-Mn separation and becomes negligible at a separation of 8.51Å.

It is important to emphasize that low-temperature resistivity and isothermal magnetization measurements reveal the coexistence of two seemingly contrasting phenomena: the Kondo effect and ferromagnetic order. However, several studies have reported the coexistence of Kondo scattering and ferromagnetism in heavy fermion systems [80, 96–99]. Thus, to verify the heavy fermionic nature of the prepared composition, we have measured the specific heat of $x = 0.25$ at $H = 0$ T, as shown in Fig.5.12(a). Above magnetic transition temperature, the specific heat data can be described by the standard formula $C(T) = \gamma T + \beta T^3$, where the first and second terms represent the electronic and lattice contributions to $C(T)$. Linear fit of the plot C/T versus T^2, as shown by the straight lines in Fig.5.11(b), yields a moderately enhanced value of the Sommerfeld constant, $\gamma = 54.87 \pm 0.45$ mJ/mol-K^2, that confirms the heavy fermionic behavior of the Fe$_2$Ti$_{1-x}$Mn$_x$Sn ($x \geq 0.25$). In particular, γ for $x = 0.25$ is more than twice the value reported for pristine Fe$_2$TiSn [67]. The γ values ranging from a few mJ/mol-K^2 to 2500 mJ/mol-K^2 are not uncommon in Kondo systems [100, 101]. An estimate of the Debye temperature (θ_D) is obtained from the β using the relation $\beta = 12\pi^4 nR/5\theta_D$, where n and R represent the number of atoms in the formula unit and universal gas constant, respectively. The value of θ_D obtained here is $sim359.3 \pm 1.2$ K.

Hence, according to the results of magnetic measurements, the magnetic state of Fe$_2$Ti$_{1-x}$Mn$_x$Sn changes with temperature as marked in the x-T phase diagram, as shown in Fig.5.12(a). Fe$_2$Ti$_{1-x}$Mn$_x$Sn is in a typical PM state when the temperature is higher than T$_s$. As the temperature decreases, ferromagnetic correlation appears because of the formation of
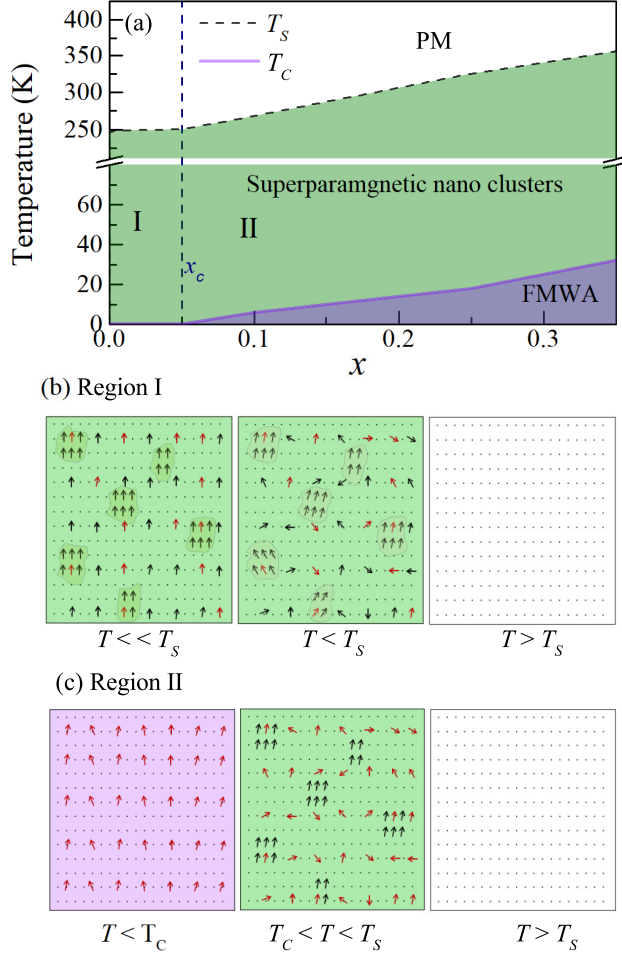
Figure 5.12: (a) x-T phase diagram representing the change in the magnetic state of $Fe_2Ti_{1-x}Mn_xSn$ with temperature. (b) and (c) represents the schematic diagram of the magnetic state as a function of temperature in regions I and II, respectively. The local Mn moments (red arrow) align at an angle with the direction of the applied magnetic field.

magnetic clusters. In the case of $x < x_c$ (region-I), clusters continue to evolve with falling temperatures and lead to a superparamagnetic ground state, and no long-range magnetic order is observed in this region. The simplified schematic diagram of the magnetic state as a function of temperature is presented in Fig.5.12(b-c). Substituting higher Mn content ($x > x_c$) in place of Ti in $Fe_2Ti_{1-x}Mn_xSn$ significantly alters this magnetic behavior. The strong local moments of Mn suppress the influence of high-temperature FM clusters on the low-temperature magnetic ground state and result in an unconventional ferromagnetic ordering driven by random

anisotropy, known as the "ferromagnet with wandering axis" state, as represented as region-II in the phase diagram. This transition from a superparamagnetic state in Fe_2TiSn to a weak random anisotropy-driven state with Mn substitution underscores the significant impact of Mn substitution on the magnetic properties of Heusler alloys. Furthermore, as confirmed from electrical resistivity and magnetic measurements and further supported through our DFT calculations, Mn substitution induces half-metallicity in the $Fe_2Ti_{1-x}Mn_xSn$, enhancing its potential for spintronic applications.

5.3   Conclusion

This study investigated structural, magnetic, and transport properties of Mn-substituted Fe_2TiSn through room temperature XRD, temperature and field-dependent magnetization, and magneto-transport measurements. Room temperature XRD patterns confirm the single-phase formation of all the compositions with ordered $L2_1$ structure. The temperature variation of electrical resistivity $Fe_2Ti_{1-x}Mn_xSn$ shows an overall increase in the magnitude with increasing Mn content. For $x \geq 0.25$, $\rho(T)$ shows a negative temperature coefficient of resistance, followed by an upturn at T < 20 K due to Kondo-like scattering and EEI. High-temperature electrical transport measurements, combined with the density of states calculation, indicate the possible formation of spin-polarized electronic structures and suggest half-metallicity in Mn-substituted Fe_2TiSn. Magnetization measurements display features indicative of weak anisotropy in the system, and low-temperature $M(H)$ behavior aligns with the random anisotropy model, suggesting that a ferromagnet with a wandering axis can be an apt description of the magnetic ground state of the $Fe_2Ti_{1-x}Mn_xSn$ compositions. The local lattice distortion in the prepared compositions leads to weak random anisotropy, affecting the overall magnetic properties.

.

Chapter 6

Evidence of magnetoelastic coupling and magnetic phase coexistence in cubic $Mn_{1.7}Fe_{1.3}Si$ Heusler Alloy

6.1 Overview

This chapter presents a detailed study of the structural, magnetic, and transport properties of cubic $Mn_{1.7}Fe_{1.3}Si$. Magnetization measurements reveal a paramagnetic to ferromagnetic transition at 85 K, followed by a spin reorientation. Neutron diffraction confirms magnetoelastic coupling and canted antiferromagnetic ordering below 55 K. The compound shows metallic behavior with a field-induced metamagnetic transition at low temperatures, supported by magnetization and magneto-transport data. An H-T phase diagram reveals a phase coexistence region below 2.5 T. Unlike typical Heusler alloys, the observed metamagnetic transition is purely magnetic, underscoring the material's relevance for spintronic applications.
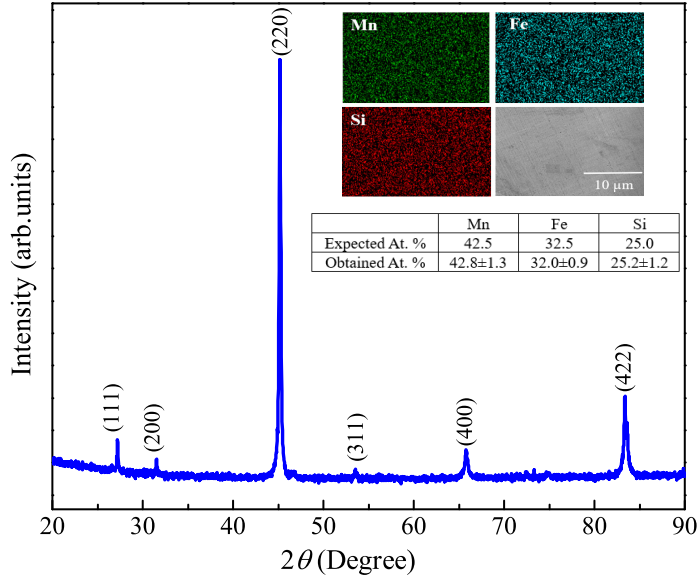
Figure 6.1: Room temperature X-ray diffraction profile of $Mn_{1.7}Fe_{1.3}Si$. The inset of the figure shows the elemental mapping and SEM image at the scale of 10 μm. Additionally, the table in the inset compares the expected and experimentally obtained atomic percentages of the elements from EDX analysis.

6.2 Results

We begin by examining the crystal structure and magnetic transitions of the prepared $Mn_{1.7}Fe_{1.3}Si$ using X-ray diffraction (XRD), EDS, and temperature-dependent magnetization measurements of the prepared composition. Fig.6.1 shows the room temperature XRD profile of the $Mn_{1.7}Fe_{1.3}Si$, where strong superlattice reflections (111) and (200) at low angles indicate the formation of a cubic Heusler structure. No secondary phase is observed in the XRD profile. The inset of Fig.6.1 shows the elemental mapping and SEM image of the $Mn_{1.7}Fe_{1.3}Si$, with EDS analysis confirming the Mn, Fe, and Si ratios aligning with the derived stoichiometry. The temperature-dependent magnetization, $M(T)$, measured in an applied external field of 0.01 T, is shown in Fig.6.2. Measurements were performed under three different protocols: zero-field-cooled warming (ZFCW), field-cooled cooling (FCC), and field-cooled warming
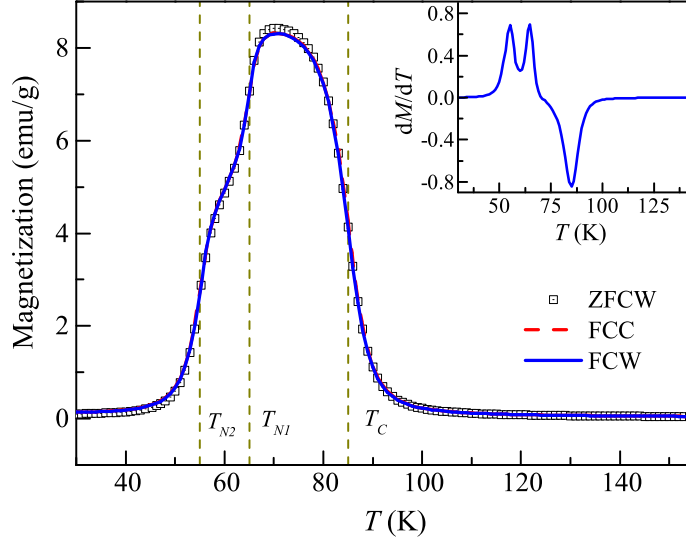
Figure 6.2: Temperature dependent magnetization, $M(T)$, of $Mn_{1.7}Fe_{1.3}Si$ measured at an applied field of 0.01 T. The vertical dotted lines represent the magnetic transition temperatures obtained from the inflection point in the derivative plot of the magnetization with respect to temperature (shown in the inset of the figure).

(FCW). The $M(T)$ curve undergoes a paramagnetic (PM) to ferromagnetic (FM)/ferrimagnetic (FiM) transition at $T_C = 85$ K. With a further decrease in temperature, the FM/FiM-to-antiferromagnetic (AFM) transition is marked by a sharp drop in M below 70 K, with two cusp like features at $T_{N1} = 65$ K and $T_{N2} = 55$ K. These features are clearly observed in the dM/dT curve, presented in the inset of the figure. All observed transitions match well with the previously reported values [102, 103].

The crystal structure of Heulser alloys is best described in terms of four interpenetrating FCC sublattices situated at four Wyckoff positions (0,0,0), (0.25, 0.25, 0.25), (0.5, 0.5, 0.5) and (0.75, 0.75, 0.75). An ordered Heusler structure, described by compositional formula X_2YZ, where X and Y are transition metals and Z is the main group element, crystallizes either with Cu_2MnAl-type structure (space group Fm$\bar{3}$m; L2$_1$) or with Hg_2CuTi-type structure (space group F$\bar{4}$3m; XA). In L2$_1$ structure, the Wyckoff positions (0.75, 0.75, 0.75) and (0.25, 0.25, 0.25) are equivalent and occupied by X atoms, while the positions (0, 0, 0) and (0.5, 0.5, 0.5)
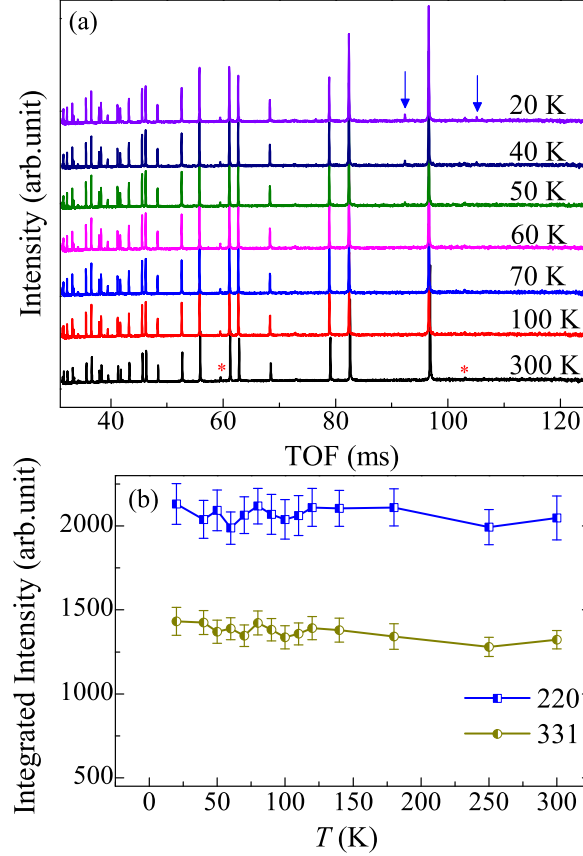
Figure 6.3: (a) Neutron powder diffraction pattern of $Mn_{1.7}Fe_{1.3}Si$. The asterisks show spurious peaks from the vanadium window, and arrows mark the new satellite peak below 55 K due to antiferromagnetic ordering. (b) The integrated intensity over the entire temperature range of the two most intense peaks, (220) and (331), present at TOF $\sim$ 96 ms and $\sim$ 82 ms, respectively.

are occupied by Y and Z atoms, respectively. On the other hand, in the XA structure, X atom occupies the position (0, 0, 0) and (0.75, 0.75, 0.75), and Y and Z atoms occupy positions (0.25, 0.25, 0.25) and (0.5, 0.5, 0.5), respectively.

Amongst the full Heusler compositions derived from the $Fe_{3-x}Mn_xSi$ series, the Fe_2MnSi composition crystallizes in an ordered $L2_1$ structure [104], while Mn_2FeSi adopts XA structure [24]. The similar scattering factor of Mn and Fe makes it difficult to distinguish the crystal structure and detect the antisite disorder through XRD analysis. Consequently, the crystal structure of the present composition could be either $L2_1$ or XA, a

distinction not considered in the previous reports. Furthermore, the two cusp-like features, labeled as T_{N1} and T_{N2} in Fig.6.2, are often interpreted as the onset of two consecutive antiferromagnetic transitions [102, 103]. However, to our knowledge, no study has yet fully addressed these magnetic transitions. Previous neutron diffraction measurement on $Fe_{3-x}Mn_xSi$ was performed above T_{N1}, and below T_{N2}, missing any potential AFM signal between T_{N1} and T_{N2} [105]. To fill this gap in understanding the crystal structure and magnetic ordering in $Mn_{1.7}Fe_{1.3}Si$, we performed high-resolution neutron powder diffraction (NPD) measurements. The measurements were conducted from 20 K to 300 K using the time-of-flight (TOF) method, covering all magnetic transitions. Fig.6.3 presents typical data collected from this experiment. At 300 K, the NPD pattern reveals peaks consistent with the cubic full Heusler structure. The peaks marked as asterisks are from vanadium windows in the sample environment.

For analysis of the NPD data, we initially assumed a structural model based on pure XA phase, and space group $F\bar{4}3m$ was assumed for the $Mn_{1.7}Fe_{1.3}Si$ compound at the start of the refinement. In this arrangement, the Wyckoff position (0.25, 0.25, 0.25) is partially substituted by Mn (denoted as Mn1) and Fe (denoted as Fe1). Meanwhile, the remaining Mn (Mn2) and Fe (Fe2) occupy the Wyckoff positions (0, 0, 0) and (0.75, 0,75, 0.75). The Si atom occupies the position (0.5, 0.5, 0.5). To account for any antisite disorder, the occupancies were adjusted to preserve the consistent total atom occupancy at both sites. After refining this model, the general formula of the prepared composition turns out to be $Mn_{1.4}Fe_{1.68}Si$, implying a straight deviation from the target stoichiometry of $Mn_{1.7}Fe_{1.3}Si$. Also, such an atomic ratio contradicts the EDX results, suggesting the prepared composition does not crystallize in the XA phase. As a result, we have modified our model to the $L2_1$ structure (space group $Fm\bar{3}m$) to refine the nuclear structure. In this model, the Wyckoff position (0.25, 0.25, 0.25) is jointly occupied by Fe and Mn1, while Si and Mn2 occupy the (0.5,0.5,0.5) and (0,0,0) positions, respectively. By changing the structural model from XA to $L2_1$, the refinement of the pattern gives the general formula to be
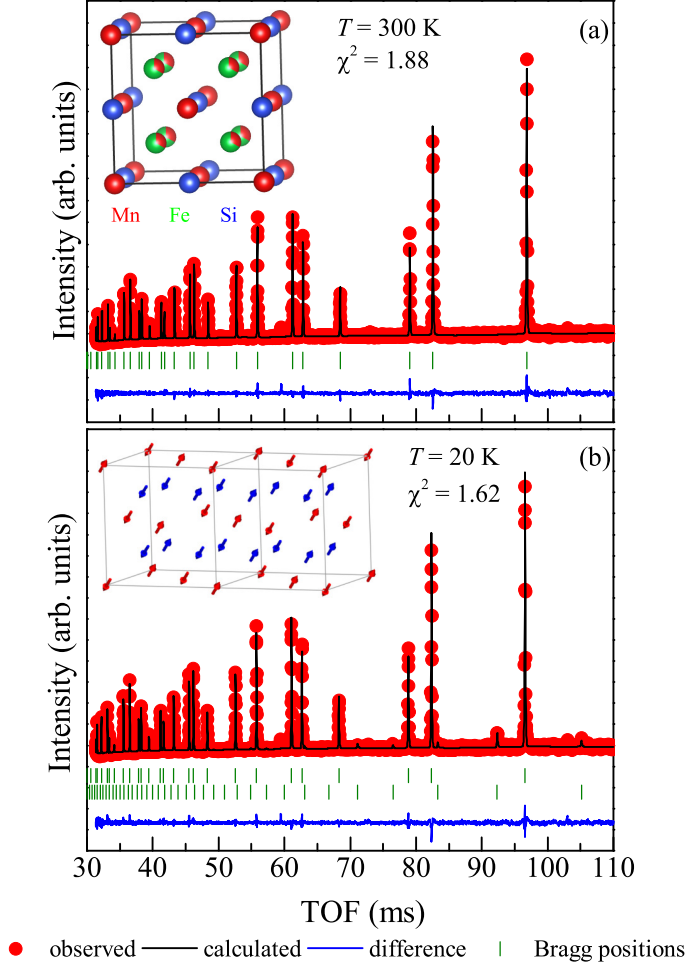
Figure 6.4: The Rietveld refined neutron powder diffraction pattern of $Mn_{1.7}Fe_{1.3}Si$ at (a) 300 K and (b) 20 K. The inset in (a) depicts the crystallographic unit cell of $Mn_{1.7}Fe_{1.3}Si$, while the inset in (b) illustrates a three-dimensional representation of the magnetic spin arrangement, as determined from the neutron diffraction data at 20 K.

Table 6.1: Crystallographic parameters of $Mn_{1.7}Fe_{1.3}Si$ obtained from the Rietveld refinement of the neutron powder diffraction data at 300 K (space group $Fm\bar{3}m$, No. 225). The estimated lattice parameter is 5.6757(4) Å.

Atom	x	y	z	Occupancy	$B_{iso}(\text{Å}^2)$
Fe	0.25	0.25	0.25	0.0270(4)	0.487(0)
Mn1	0.25	0.25	0.25	0.0146(2)	0.487(0)
Mn2	0.00	0.00	0.00	0.0211(5)	0.629(25)
Si	0.50	0.50	0.50	0.0207(1)	0.492(23)

$Mn_{1.69}Fe_{1.31}Si$, which matches well with the target stoichiometry, as well as with the EDX results. This confirms that $Mn_{1.7}Fe_{1.3}Si$ crystallizes in long-range $L2_1$ order. The refinement of the room temperature ND pattern with $Fm\bar{3}m$ space group is shown in Fig.6.4(a), and the crystallographic parameters obtained from the refinement are listed in Table 6.1. The inset of Fig.6.4(a) presents the crystal structure of $Mn_{1.7}Fe_{1.3}Si$ after refinement.

Next, we analyze the magnetic contribution to the NPD pattern. As shown in Fig.6.3(a), the overall NPD pattern remains unchanged across the temperature range of 20 K to 300 K, spanning all magnetic transition temperatures (marked in Fig.6.2). This consistency confirms the absence of a nuclear phase transition down to 20 K. However, new satellite peaks appear only at T $\leq$ 55 K (marked by arrows in Fig.6.3(a)), indicating the onset of AFM order. Viewing from the high-temperature side, no additional Bragg reflections appear as the temperature reaches 70 K (i.e., $\leq T_C$). The magnetic order in this temperature range can be weak FM/FiM, as there is no enhancement of the peak intensity below T_C, which may be due to the weak magnetic signal beyond the instrument's sensitivity. For further clarity, the temperature dependence of the integrated intensity of some selected Bragg peaks is shown in Fig.6.3(b), which reveals no intensity enhancement at low temperatures, preventing us from refining the magnetic structure at T_C. Upon lowering the temperature further, new satellite
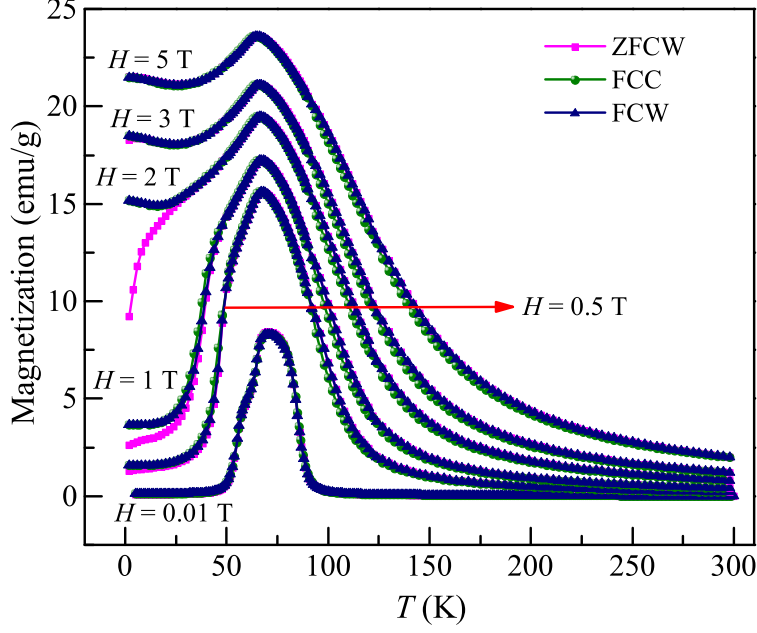
Figure 6.5: Variation of magnetization with the temperature ($M(T)$) measured at different applied magnetic fields under ZFC, FCC, and FCW protocols.

peaks appear at T ≤ 55 K, confirming the onset of AFM order. Notably, no AFM transition is detected between T_{N1} and T_{N2}. This result counters the observation made in Ref. [102, 103]. It is worth noting that such a cusp-like feature in magnetization is often interpreted as the spin reorientation transition (SRT) in various Mn-based intermetallic alloys [106–109]. The SRT leads to a noncollinear magnetic order with uniaxial anisotropy and extreme sensitivity to the DC-field bias.

To analyze the newly observed satellite peaks, the magnetic structure compatible with Fm$\bar{3}$m space group symmetry is determined using representation analysis with the BasIreps program implemented in the FULLPROF suite [53]. A search for a wave vector that yields intensities corresponding to this set of magnetic reflections revealed that the extra peaks could only be indexed to propagation vector $k = [1/2, 1/2, 1/2]$. We observed only two Bragg peaks in the NPD pattern of Mn$_{1.7}$Fe$_{1.3}$Si, which is insufficient to unambiguously solve the magnetic structure. To determine the magnetic structure and ordered magnetic moment of the

Mn atoms, we assumed that Mn atoms present at two equivalent sites (Mn1 at (0.25,0.25,0.25) and Mn2 at (0.5,0.5,0.5)) have the same magnetic moment. The refinement of the magnetic structure, as shown in Fig.6.4(b), suggests a canted antiferromagnetic ordering, with magnetic moments parallel to <111> axis, which is consistent with the previous reports on $Fe_{3-x}Mn_xSi$ [105]. These moments are ferromagnetically aligned within the respective {111} planes while adjacent planes are coupled antiferromagnetically. Our refinement indicates that the Mn moments exhibit equal components along the x, y, and z crystallographic directions, with the magnetic moment per Mn atom along each axis determined to be 0.5413 ± 0.019 μ_B. In our magnetic structure refinement, we considered the magnetic moments at the Mn sites, as Mn is known to be the dominant magnetic species responsible for introducing spin canting in $Fe_{3-x}Mn_xSi$ compounds [110]. Since Fe also occupies the (0.25, 0.25, 0.25) site alongside Mn, its contribution to the overall magnetic ordering warrants further discussion. To address this, we tested an alternative refinement where magnetic moments were assigned to Fe atoms as well. Interestingly, we found that the refined moment on Fe was equal to that of Mn atoms. However, due to Fe and Mn sharing the same crystallographic site, neutron diffraction cannot distinguish their individual contributions.

Fig.6.5 shows the temperature-dependent magnetization, $M(T)$, recorded for different applied fields measured from 2 K to 300 K under ZFCW, FCC, and FCW protocols. A sharp rise in magnetization observed around 100 K is attributed to the magnetic phase transition from PM to FM/FiM state. Intriguingly, magnetization in this FM/FiM state decreases gradually after attaining a peak value at around 75 K. However, the corresponding NPD data shows only one AFM phase below 55 K. Therefore, the gradual decrease in magnetization below 75 K could be a result of a spin re-orientation transition (SRT) from FM/FiM structure to canted AFM structure. This onset of SRT can be linked to the appearance of kink-like features at $T \sim 65$ K in the $M(T)$ curve, as clearly marked in Fig.6.2. Additionally, below 55 K, the $M(T)$ curve becomes constant with a value
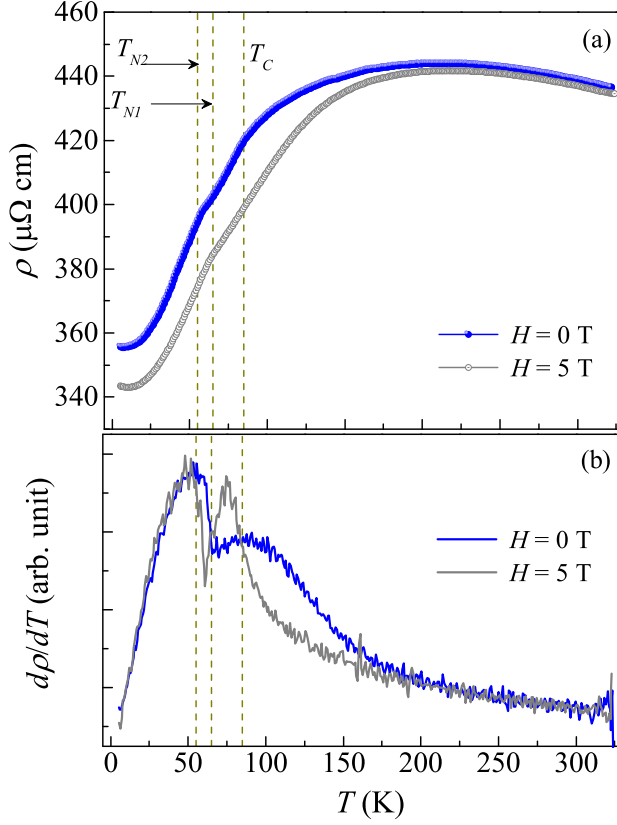
Figure 6.6: (a) Temperature-dependent resistivity, ρ(T) of $Mn_{1.7}Fe_{1.3}Si$ and, (b) derivative plot of ρ with temperature under an applied magnetic field of 0 T and 5 T.

close to zero, indicating the SRT occurs between 65 K and 55 K. Further observations can be made from $M(T)$ curves measured at higher fields: (i) the bifurcation between the ZFCW and FCC curve first increases and then decreases with an increase in the applied field, as shown in the Fig.6.5; (ii) the kink around 65 K becomes less pronounced and eventually disappears at higher fields; and (iii) the step-like characteristics of $M(T)$ at around T_{N1} at lower field gives way to regular peak-like characteristic at higher fields, which further becomes less pronounced and transition becomes more diffuse. The weakening of the feature associated with SRT and the diminishing of the bifurcation between ZFCW-FCC suggests that the SRT from the FM/FiM to the canted AFM structure is stable only in moderate fields and becomes weaker in higher fields.

Fig.6.6(a) presents the variation of electrical resistivity, ρ(T), with
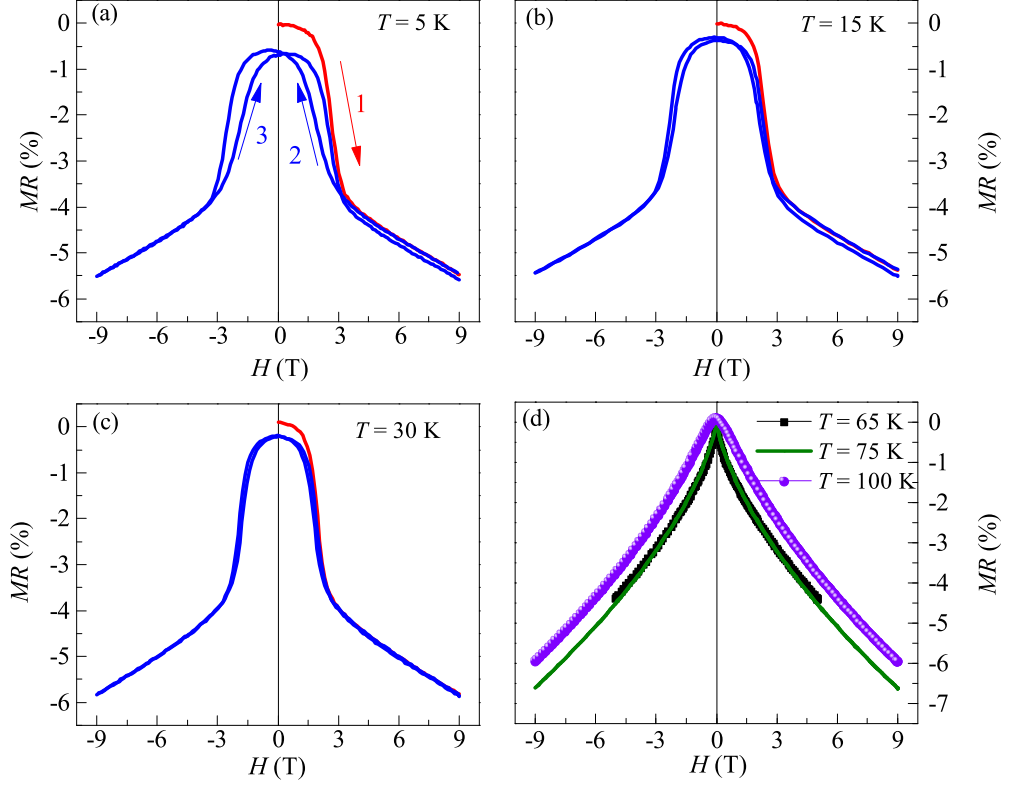
Figure 6.7: The field-dependent transverse magnetoresistance (I ⊥ B) of $Mn_{1.7}Fe_{1.3}Si$ measured at fixed temperatures by varying the applied magnetic field of $\pm$ 9 T. The arrows labeled 1, 2, and 3 depict the magnetic field excursion paths: 0 to +9 T, +9 T to −9 T, and −9 T to +9 T, respectively.

temperature measured under an applied magnetic field of 0 and 5 T. The $\rho(T)$ curve at $H = 0$ T shows three consecutive slope changes as temperature decreases. These anomalies are prominent in the derivative plots (Fig.6.6(b)), and the transition temperatures are in good agreement with those derived from magnetization measurements (at Fig.6.2). With decreasing temperature, $\rho(T)$ drops rapidly, followed by a gradual saturation to a constant value near 5 K, confirming the metallic character of the system. Further, the $\rho(T)$ measured with $H = 5$ T begins to deviate from the 0 T curve around 150 K, indicating the presence of magnetoresistance over a wide temperature range. The effect of the magnetic field on magnetic transition temperatures can be observed in the derivative plots presented in Fig.6.6(b).

The corresponding field-dependent transverse (I ⊥ B) magnetoresis-

tance (MR) at various temperatures is shown in Fig.6.7. The MR plots were obtained after warming the sample to the PM state before each measurement. At $T = 5$ K, MR remains nearly constant in the low field region (≤ 1.5 T) and then decreases abruptly after $H_1 \sim 1.5$ T. This sharp decrease in MR persists until $H_2 \sim 3$ T; thereafter, it decreases linearly with the field. Upon lowering the applied field (path-2), MR retraces the curve up to H_2 but shows hysteresis with a further decrease in the field. During the field cycling from +9 T to -9 T along path-2 and -9 T and +9 T along path-3, the virgin curve (path-1) lies outside the envelope curve, forming a butterfly-like hysteresis loop. The MR at $H = 0$ after field excursion, denoted as $MR(0)^{mixed}$, is marginally lower than the initial or virgin $MR(0)$ value. As the temperature increases to 15 K and 30 K, the size of the butterfly-like loop becomes smaller compared to that observed at 5 K, and the $MR(0)^{mixed}$ value undergoes gradual reduction relative to the respective virgin $MR(0)$ value. With further increase in temperature, the hysteresis loop completely vanishes, and a quasi-linear behavior of the MR curve is observed, as shown in Fig 6.7(d).

This motivated us to investigate the isothermal field-dependent magnetization, $M(H)$. The $M(H)$ data were measured at selected temperatures between 5 K and 300 K over a field range of ± 5 T, as shown in Fig.6.8. In the low-field region, $M(H)$ shows linear variation with the field, akin to AFM ordering of the material. However, an increase in M at a specific field value, H_1, indicates a field-induced metamagnetic transition, occurring over a broad field range from H_1 (~ 1.5 T) to H_2 (~ 3 T). As the field increases further from 3 to 5 T, the $M(H)$ curve shows a curvature with a non-saturating tendency. A hysteresis is observed when the field is reduced from 5 T to 0 T. The hysteresis loop, however, collapses before the field reaches zero, exhibiting a high coercive field of 0.17 T. This $M(H)$ behavior is irreversible following the first-order magnetic transition. The $M(H)$ recorded at 15 K and 30 K also show similar behavior, though the metamagnetic transitions and hysteresis loop occur at lower field values. The virgin curve lying outside the envelope loop and the irreversible hysteresis

106
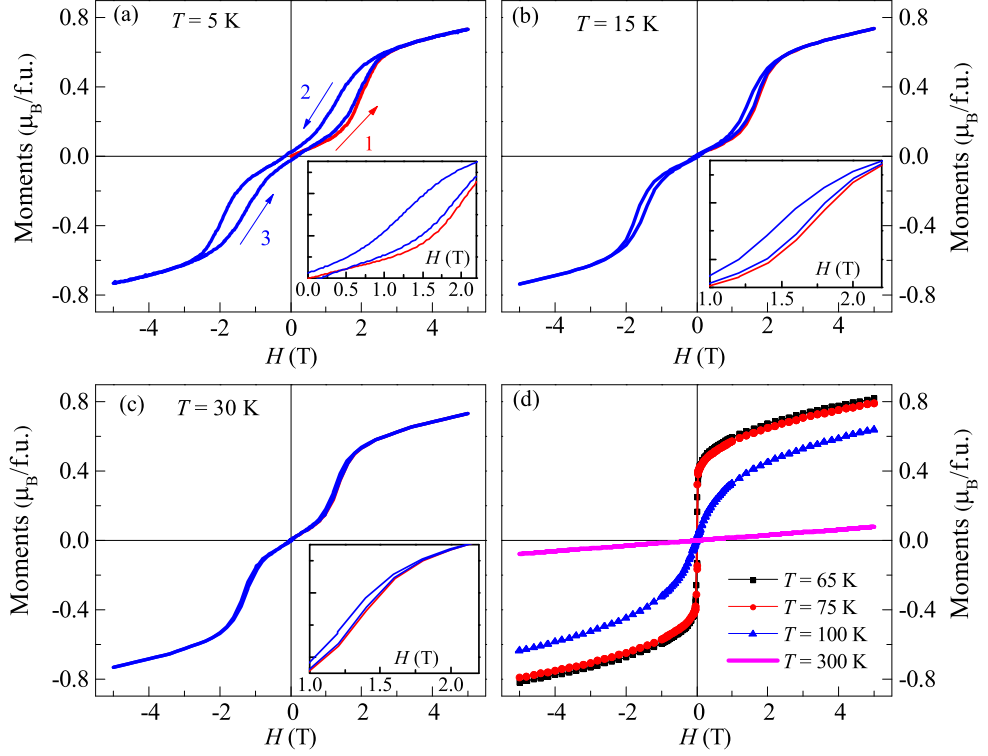
Figure 6.8: Isothermal field-dependent magnetization curves measured at fixed temperatures by varying the applied magnetic field of $\pm$ 5 T. The arrows labeled 1, 2, and 3 depict the magnetic field excursion paths: 0 to +5 T, +5 T to -5 T, and -5 T to +5 T, respectively.

suggest an incomplete metamagnetic transition for T $\leq$ 30 K. However, the $M(H)$ recorded at $T \geq 65$ K becomes fully reversible in all quadrants, with the virgin curve coinciding with the corresponding part of the hysteresis loop. Additionally, the feature of metamagnetic transition completely vanishes at 65 K, and a soft FM/FiM behavior is observed. A paramagnetic $M(H)$ is observed at 300 K. Returning to the description of the $M(H)$ observed at $T \leq 30$ K, the smooth curvature of the high field, non-saturating $M(H)$ with high coercivity confirms the FM/FiM ordering of the high-field phase. This high-field phase is partially retained even when the field is reduced to zero, suggesting a coexistence of AFM–FM/FiM phase in the material. The influence of these magnetic transitions is echoed in the MR measurements discussed earlier.

6.3 Discussion

6.3.1 Spin-reorientation transition and canted antiferromagnetic ordering

Intriguingly, the magnetization (M) in the FM phase exhibits an unconventional behavior, gradually decreasing after reaching its peak around 70 K (see Fig.6.2), rather than saturating as expected in a typical FM system. This decline in M indicates the onset of a spin-reorientation transition (SRT). The temperature derivative of $M(T)$ curve at 0.01 T reveals that SRT begins at T^{onset} = 65 K. Additionally, a further change in slope is observed at 55 K, suggesting SRT occurs within the temperature range of 65 K to 55 K.

Temperature-dependent NPD measurement further supports the presence of SRT in $Mn_{1.7}Fe_{1.3}Si$. While two consecutive kinks in the $M(T)$ curves at 65 K and 55 K were often associated with two simultaneous antiferromagnetic (AFM) transitions in previous studies, the present NPD patterns recorded across this temperature range do not show any signatures of AFM ordering between 65 K and 55 K (shown in Fig.6.3(a)). As the temperature approaches 70 K($< T_C$) from the high-temperature side, no additional Bragg reflections emerge, nor is there a noticeable enhancement in the integrated peak intensity (see Fig.6.3(b)). Upon further cooling, no new peaks appear between 65 K and 55 K, confirming the absence of long-range AFM order in this temperature range. However, below 55 K (T_{N2}), the emergence of distinct satellite peaks in the NPD patterns provides clear evidence that AFM ordering is established only below T_{N2}. These results strongly support the conclusion that the cusp-like features in magnetization at T_{N1} and T_{N2}, as shown in Fig. 6.2, correspond to a spin-reorientation transition rather than distinct AFM transitions, as also observed in other Mn-based intermetallic compounds [106–109]. The absence of a structural phase transition and the lack of detectable AFM order between 65 K and

55 K suggest that the observed SRT is driven purely by spin realignment mechanisms rather than a change in crystallographic symmetry.
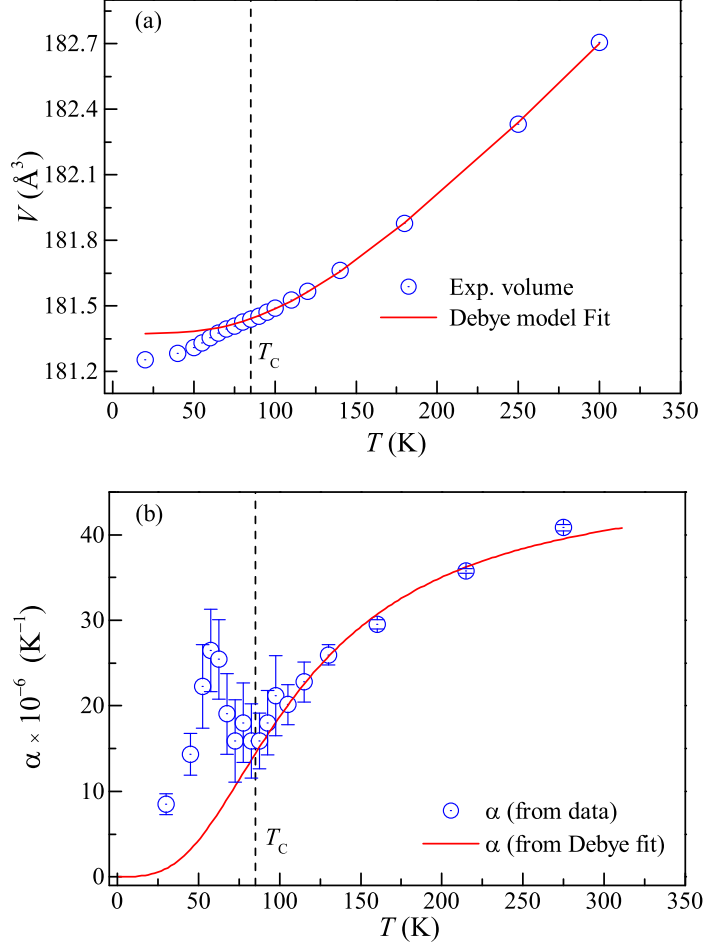
Figure 6.9: (a) The variation of unit cell volume with temperature, where the solid line shows the fit obtained using the Debye-Grüneisen model. (b) Shows the calculated volumetric thermal expansion coefficient, α (open symbols), alongside its theoretical variation (red curve) expected from the Debye fit .

The gradual decrease in magnetization below 70 K signals the onset of magnetocrystalline anisotropy (MCA), which emerges as a precursor effect preceding a magnetic phase transition. In this case, this behavior is indicative of an impending SRT, where the system evolves from a weak FM state to a noncollinear canted AFM structure, as confirmed by our neutron powder diffraction measurements. This transition reflects the competition between anisotropy energy and exchange interactions, which dictates

the realignment of spins in response to temperature variations. SRT has been studied extensively in perovskites, rare-earth oxides, and intermetallic compounds [106, 107, 111–114]. A prerequisite for SRT is the presence of magnetostructural coupling. Fig.6.9(a) shows the temperature dependence of the lattice volume, $V(T)$, derived from the Rietveld refinement of the NPD data. Although the cubic symmetry is preserved down to 20 K, the unit cell volume shows a clear slope change near T_C. The observed changes in unit cell volume around the magnetic transitions, without any change in crystallographic symmetry, suggest an isostructural distortion driven by magnetoelastic coupling. However, no prior studies have reported this effect in $Mn_{1.7}Fe_{1.3}Si$, making its investigation crucial for uncovering the mechanisms underlying the SRT in this compound. The magnetoelastic coupling can be validated by modeling the thermal expansion of unit cell volume using the Debye-Grüneisen model:

$$V(T) = V_0 + \frac{9\gamma k_B T}{B} \left(\frac{T}{\Theta_D} \right)^3 \int_0^{\Theta_D/T} \frac{x^3}{e^x - 1} \, dx \qquad (6.1)$$

where V_0, γ, k_B, B, and Θ_D are unit cell volume at 0 K, Grüneisen parameter, Boltzmann constant, bulk modulus, and Debye temperature, respectively. The extracted fitting parameters are $V_0 = (181.3739 \pm 0.0006)Å^3$ and $\Theta_D = 460.66 \pm 4.45$ K, which is reassuringly close to the value obtained from specific heat measurement [103]. It is evident from Fig.6.9(a) that above T_C, the experimental unit cell volume is well described by the Debye-Grüneisen model. However, large deviations occur in the vicinity of magnetic transitions, indicating a need for alteration in the underlying structural model. These observations confirm the genesis of the magnetic transitions in $Mn_{1.7}Fe_{1.3}Si$ to be of magnetoelastic coupling-induced structural distortion [115–117]. To further support this conclusion, we calculated the volumetric thermal expansion coefficient ($\alpha = 1/V(dV\,dT)$). Fig.6.9(b) shows the temperature variation of α alongside the expected trend from the Debye-Grüneisen model. The observed deviation in α from its expected theoretical behavior below T_C highlights the presence of strong magneto-elastic coupling in the system.

Previous NPD studies on $Fe_{3-x}Mn_xSi$ [105] have observed new satellite peaks at 4.2 K but failed to capture any change in the NPD profile between T_{N1} and T_{N2}, probably due to large temperature intervals used in those measurements. In contrast, the present study utilizes high-resolution NPD patterns recorded at an interval of 5 K below T_C, enabling us to capture anomalies in lattice parameters across the T_C and SRT. Our results show that the SRT in $Mn_{1.7}Fe_{1.3}Si$ is correlated with marked structural distortions around the magnetic transition temperature.

6.3.2 Metamagnetic transition and its effect on the magnetic and transport properties

Based on the experimental observations made in this study, an $H - T$ phase diagram of $Mn_{1.7}Fe_{1.3}Si$ has been constructed, as shown in Fig.6.10. The critical magnetic field values, while increasing ($H_{cr}(up)$) and decreasing ($H_{cr}(dn)$), for the field-induced metamagnetic transition, are plotted against temperature. FM/FiM and AFM phases coexist between $H_{cr}(up)$ and $H_{cr}(dn)$.

Tracing the anomalous magnetic behavior of $Mn_{1.7}Fe_{1.3}Si$ through this phase diagram, Path-A, B, and C indicate the $M(T)$ measurements at various constant fields. When the sample is cooled in zero field, it transforms entirely into the AFM phase. Following Path-A (at a small applied magnetic field) under ZFCW, FCC, and FCW protocols results in almost no bifurcation, as it lies outside the phase-coexistence region. A similar scenario is observed for Path-C (for $H \geq 2.5$ T). However, the low-temperature portion of Path-B lies within the phase-coexistence region. Cooling and warming the sample in the 0 and 2 T leads to bifurcation in the ZFCW and FCC/FCW curves. The absence of bifurcation in the ZFCW and FCC curve in the low-T low-H and low-T high-H regions confirms the long-range single phase of $Mn_{1.7}Fe_{1.3}Si$. This observation also supports our isothermal $M(H)$ data, where the low-H AFM region transforms into the FM/FiM state as the magnetic field increases. As discussed

111
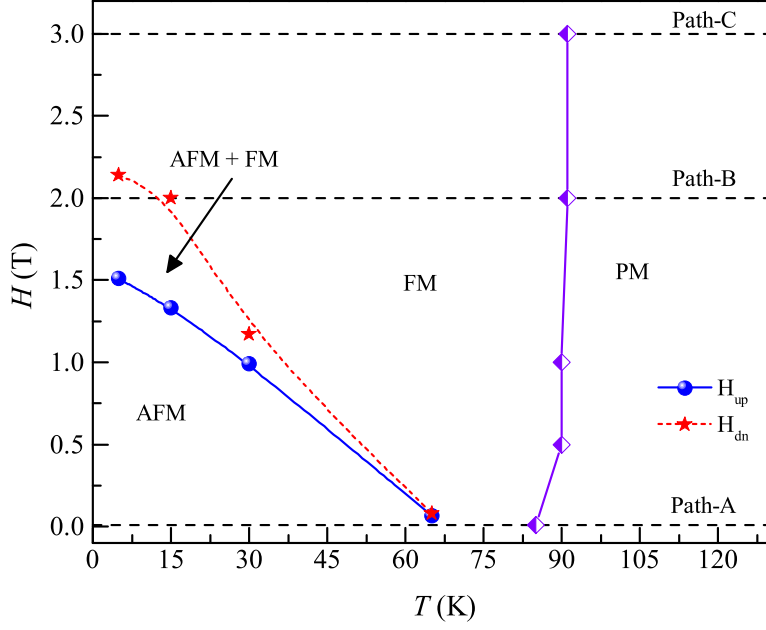
Figure 6.10: The $H - T$ phase diagram of $Mn_{1.7}Fe_{1.3}Si$. The critical magnetic field corresponding to metamagnetic is obtained from the inflection point of the derivative of the isothermal magnetization, dM/dH curve.

earlier, the initial cooling of the sample in a 2 T field results in a finite fraction of the high-temperature FM/FiM phase to exist even at $T = 5$ K, highlighting the presence of hindered kinetics during the phase transformation. During isothermal field reduction from 5 T to 0 T, the kinetics of the FM/FiM to AFM transition become impeded, indicating metastable behavior in $Mn_{1.7}Fe_{1.3}Si$ at or below 5 K after field cycling.

Next, we address the nature of MR data to investigate the effect of metastability, kinetic hindrance, and phase co-existence on transport properties. Referring to Fig.6.7, the MR plots measured at high temperatures (65 K, 75 K, and 100 K) exhibit a negative magnetoresistance, which decreases with the field starting from $H = 0$. At lower temperatures, the virgin curves of the MR plots (path-1) showed a field-induced AFM to FM/FiM transition. The decrease in MR begins at H_1 due to the onset of the FM/FiM phase, as the AFM phase gradually converts into the FM/FiM phase. This process continues until the field reaches H_2, beyond which MR exhibits the typical negative behavior associated with the fully

112

transformed FM/FiM state across the entire sample at high fields. During the field decreasing cycle (path-2), the entire sample remains in the phase-coexisted form with the lower $MR(0)$ compared to the virgin $MR(0)$. This is an expected behavior across the first-order transition, indicating metastability when the field is cycled across the transition field. The anomalous open hysteresis loop in the MR is apparent as the virgin curve lies outside the butterfly-like loop. The difference between the $MR(0)^{mixed}$ and the corresponding virgin $MR(0)$ gradually decreases with increasing temperature, reflecting the reduction in the size of the butterfly loop compared to that at 5 K. These observations are consistent with our $M(H)$ data. To the best of our knowledge, field-induced magnetic phase transitions accompanied by hindered kinetics and metastability have not been reported in cubic Heusler compounds, unlike many intermetallic compounds [118, 119], non-cubic Heusler alloys [120–122], and manganites [123]. Similar behavior has been observed in germanides, where it arises due to their coupled crystallographic-magnetic transition [124–127].

6.4   Conclusion

In conclusion, a comprehensive study of structural, magnetic, and transport properties of cubic $Mn_{1.7}Fe_{1.3}Si$ has been conducted. The room temperature powder XRD pattern confirms a long-range cubic $L2_1$ order, while temperature-dependent NPD further supports the cubic Heusler structure without any change in crystal symmetry down to 20 K. The magnetic structure refinement at $T = 20$ K confirms a canted antiferromagnetic ordering. The variation in magnetization below 70 K is attributed to a spin reorientation transition, likely driven by a gradual change in magnetocrystalline anisotropy, as evidenced by the unusual behavior of the unit cell volume around magnetic transition temperatures. The ρ(T) measurement confirms the low-temperature metallic behavior of $Mn_{1.7}Fe_{1.3}Si$. Furthermore, we have established the presence of field-induced metamagnetic transition at low temperatures. Several features characterizing the first-order

transition, such as irreversibility, metastability, and phase-coexistence, are seen distinctly in the magnetic and magnetotransport properties. While the characteristics of the compound are intriguing, the question remains whether the first-order magnetic transition is driven by a simultaneous structural transition as seen in other intermetallic compounds [126] and shape memory Heusler alloys [121, 122]. Therefore, further neutron and X-ray diffraction measurements as a function of the magnetic field will be highly valuable in addressing this question.

.

Chapter 7

Epilogue

7.1 Concluding remarks

I often reflect on the quote, "If you can't explain it to a six-year-old, you don't understand it yourself," and remind myself to seek simplicity and clarity in whatever I study. During my visits home to the village, when I walk through the fields, I'm met with a familiar question: *"What do you do?"* I answer, "Research," but it's always followed by another question: *"What is your research about?"* I try my best to explain—avoiding technical terms, simplifying where I can—but more often than not, the conversation ends with a gentle smile and words of encouragement: *"Do well and succeed"*. Though I may have failed to make them understand, these exchanges always leave me with a quiet joy. From agricultural tools and jewelry to smartphones, the products of condensed matter are used everywhere—from remote villages to the offices of world leaders. Yet, the science behind them remains a mystery to most. The behavior of condensed matter hides countless wonders, and I consider myself fortunate to have been allowed to explore even a few of them. In the final chapter, we revisit some of those explorations that brought results worth documenting and those that led to dead ends, now tucked away in the corners of the mind or on forgotten pages of a notebook. Perhaps I've failed to explain it to the populace, but I believe what's written here might still be useful to

someone.

In Chapter 1, we began with a simple yet fascinating idea: how a combination of just three elements from the periodic table, arranged in a specific cubic symmetry known as the Heusler structure, can give rise to a plethora of physical properties. This seemingly modest arrangement of atoms has historically revealed a rich tapestry of behaviors, ranging from magnetism to semiconducting, half-metallicity, and topological characteristics. To set the stage, we revisited some early pioneering studies that brought Heusler alloys to the forefront of condensed matter research. These works not only underscored the versatility of these materials but also laid the foundation for understanding the intricate relationship between their atomic structure and physical behavior. A central theme in our discussion was the critical role of structural ordering. In Heusler alloys, the arrangement of atoms across the crystallographic sites plays a decisive role in governing their magnetic and transport properties. A small deviation from their ideal ordering, a phenomenon known as antisite disorder, can drastically alter the materials' magnetic and transport properties. The overarching aim of this thesis has thus been to deepen our understanding of the structure-property relationship in Heusler alloys. Thus, we sought to characterize and quantify the disorder and uncover how it can be controlled or utilized to engineer desired functionalities in these complex intermetallic systems.

In the next two chapters, Chapter 3 and Chapter 4, we explored two Heusler systems, Fe_2TiSn and Mn_2FeSi. Chapter 3 begins with exploring the amount of anti-site disorder and the effect of secondary annealing on the physical properties of Fe_2TiSn and its Sb and Cr substituted half-metallic compositions, namely $Fe_2TiSn_{0.5}Sb_{0.5}$ and $Fe_2Ti_{0.75}Cr_{0.25}Sn$. We have quantified the amount of anti-site disorder in these compositions using temperature-dependent powder neutron diffraction. Anti-site disorder significantly affects these compositions' magnetic and electrical transport properties. Further, we have subjected all the compositions to secondary heat treatment and studied their effects on their electrical resistivity and magnetization, suggesting a noticeable decrease in antisite disorder. Fur-

ther, in Chapter 4, we have explored the electronic structure, crystal and microstructure, and magnetic properties of Mn_2FeSi, using the density of states calculations, X-ray diffraction, and temperature and field-dependent magnetization measurements. We have also elucidated the impact of atom swapping among different constituents of Mn_2FeSi on its magnetic and electronic properties. Furthermore, we synthesized Mn_2FeSi in a pure cubic inverse Heusler phase by substituting 10% Al at the Si site and subsequently examined its magnetic properties in detail. Our magnetic study unveiled an antiferromagnetic (AFM) ground state at temperatures below 50 K and a Griffiths-like phase within 184–260 K in a cubic Heusler compound. These findings contribute to a deeper understanding of the electronic properties of Mn_2FeSi and highlight the intriguing complexities arising from disorder and its profound influence on the magnetic behavior of Heusler alloys.

Chapters 5 and 6 take a step further by exploring the impact of elemental substitution on the Fe_2TiSn and Mn_2FeSi systems. Chapter 5 comprehensively studies the structural, magnetic, and transport properties of Mn-substituted Fe_2TiSn compositions. Ab initio calculations reveal that Mn substitution introduces localized magnetic moments, which play a central role in establishing the magnetic order of the system. These localized moments interact with the conduction electrons, giving rise to a Kondo-like scattering mechanism that governs the electrical transport behavior. Magnetic measurements as a function of temperature and magnetic field point to a pronounced magnetic anisotropy, influencing the low-temperature magnetic ground state. Complementary EXAFS analysis suggests that this magnetocrystalline anisotropy stems from subtle local lattice distortions within the cubic Heusler structure. Interestingly, the system exhibits a rare coexistence of two seemingly contradictory phenomena—ferromagnetic ordering and the Kondo effect—highlighting the delicate interplay between structure, magnetism, and electronic transport in disordered Heusler systems.

In Chapter 6, we build upon the findings of Chapter 4, where phase-pure Mn_2FeSi was shown to exhibit antiferromagnetic ordering below 50 K.

Here, we explore the effect of partially substituting Mn with Fe, focusing on the composition $Mn_{1.7}Fe_{1.3}Si$. This substitution brings about remarkable changes in the magnetic behavior. Temperature-dependent magnetization and neutron powder diffraction measurements reveal a spin reorientation transition between 65 K and 55 K, followed by a canted antiferromagnetic ground state below this range. Isothermal magnetization and magneto-transport studies further uncover a field-induced metamagnetic transition at low temperatures. Interestingly, the unit cell volume, as extracted from temperature-dependent neutron diffraction refinements, displays a distinct change in slope near the magnetic transition points, indicating a strong magnetoelastic coupling in this system. The constructed H–T phase diagram, based on magnetoresistance and magnetization data, illustrates the coexistence of multiple magnetic phases at low temperatures, emphasizing the intricate interplay between structural distortions, magnetic anisotropy, and external magnetic fields in $Mn_{1.7}Fe_{1.3}Si$.

7.2 Future prospects

Over the course of this study, we have explored how small rearrangements-some swapping places with each other, some introduced after substitution-can lead to big changes in how a material behaves. But the story doesn't end here. Several promising directions emerge from this work.

- A systematic study of the dynamic evolution of magnetic phases under external perturbations such as pressure or strain may provide deeper insights into the magneto-elastic coupling observed in $Mn_{1.7}Fe_{1.3}Si$.

- Furthermore, magnetic phase coexistence and field-driven transition make it a candidate for magnetocaloric and spintronic applications, warranting further investigation of its thermal and spin transport properties.

- Third, the coexistence of ferromagnetic ordering and the Kondo effect opens up exciting possibilities for studying quantum criticality

in $Fe_2Ti_{1-x}Mn_xSn$.

Some of what I have found is documented here. I believe it's a quiet contribution, like the unseen roots of a plant, but I hope it supports something that grows. Well, with this, *this thesis* comes to an end.

Bibliography

[1] Friedrich Heusler. Über magnetische manganlegierungen. Verh. Dtsch. Phys. Ges, 5, 1903.

[2] Sabine Wurmehl, Gerhard H. Fecher, Hem C. Kandpal, Vadim Ksenofontov, Claudia Felser, Hong-Ji Lin, and Jonder Morais. Geometric, electronic, and magnetic structure of Co_2FeSi: Curie temperature and magnetic moment measurements and calculations. Phys. Rev. B, 72:184434, 2005.

[3] Hiroshi Matsui, Terutaka Goto, Tadao Fujimura, Yoshichika , nuki , Takemi Komatsubara, Yosikazu Isikawa, and Kiyoo Sato. Magneto-acoustic effect of heavy fermion compound $CeInCu_2$. J. Phys. Soc. Jpn., 59:3451–3454, 1990.

[4] C. Pfleiderer, J. Bœuf, and H. v. Löhneysen. Stability of antiferro-magnetism at high magnetic fields in Mn_3Si. Phys. Rev. B, 65:172404, 2002.

[5] S. L. Town P. J. Webster, K. R. A. Ziebeck and M. S. Peak. Magnetic order and phase transformation in Ni_2MnGa. Philosophical Magazine B, 49:295–310, 1984.

[6] P. A. Bhobe, K. R. Priolkar, and A. K. Nigam. Room temperature magnetocaloric effect in Ni–Mn–In. Appl. Phys. Lett., 91, 2007.

[7] Fabian Garmroudi, Michael Parzer, Alexander Riss, Andrei V. Ruban, Michele Reticcioli, Matthias Knopf, Herwig Michor, Andrej

Pustogow, Takao Mori, and Ernst Bauer. Anderson transition in stoichiometric Fe_2VAl: high thermoelectric performance from impurity bands. Nat. Commun., 13, 2022.

[8] A. Chanda, Deepika Rani, Jadupati Nag, Aftab Alam, K. G. Suresh, M. H. Phan, and H. Srikanth. Emergence of asymmetric skew-scattering dominated anomalous nernst effect in the spin gapless semiconductors $Co_{1+x}Fe_{1-x}CrGa$. Phys. Rev. B, 106:134416, 2022.

[9] S. Chadov, X. Qi, J. Kübler, and et al. Tunable multifunctional topological insulators in ternary heusler compounds. Nature Mater, 9:541–545, 2010.

[10] E Persson. On the structure of the heusler alloys. Z. Phys, 57:115–133, 1929.

[11] A. J. Bradley and J. W. Rodgers. The crystal structure of the heusler alloys. Proc. R. Soc. Lond. A, 144:340–359, 1934.

[12] Peter J. Webster. Heusler alloys. Contemp. Phys., 10:559–577, 1969.

[13] I. Galanakis, P. H. Dederichs, and N. Papanikolaou. Slater-pauling behavior and origin of the half-metallicity of the full-heusler alloys. Phys. Rev. B, 66:174429, 2002.

[14] MI Katsnelson, V Yu Irkhin, Liviu Chioncel, AI Lichtenstein, and Robert A de Groot. Half-metallic ferromagnets: From band structure to many-body effects. Rev. Mod. Phys., 80:315–378, 2008.

[15] Valentin Yu Irkhin and Mikhail Iosifovich Katsnel'son. Half-metallic ferromagnets. Phys. Usp., 37:659, 1994.

[16] Shambhu KC, R Mahat, S Regmi, A Mukherjee, P Padhan, R Datta, WH Butler, A Gupta, and P LeClair. Tunable properties and potential half-metallicity in $Co_{2-x}Ti_xFeGe$ heusler alloys: An experimental and theoretical investigation. Phys. Rev. Mater., 3:114406, 2019.

[17] Deepika Rani, Lakhan Bainsla, Aftab Alam, and KG Suresh. Spin-gapless semiconductors: Fundamental and applied aspects. J. Appl. Phys., 128, 2020.

[18] Snehashish Chatterjee, Souvik Chatterjee, Saurav Giri, and Subham Majumdar. Transport properties of heusler compounds and alloys. J. Phys.: Condens.Matter, 34:013001, 2021.

[19] GP Felcher, JW Cable, and MK Wilkinson. The magnetic moment distribution in Cu_2MnAl. J. Phys. Chem. Solids, 24:1663–1665, 1963.

[20] DP Oxley, RS Tebble, and KC Williams. Heusler alloys. J. Appl. Phys., 34:1362–1364, 1963.

[21] J Kübler, AR William, and CB Sommers. Formation and coupling of magnetic moments in heusler alloys. Phys. Review. B, 28:1745, 1983.

[22] JL Moran-Lopez, R Rodriguez-Alba, and F Aguilera-Granja. Modeling the magnetic properties of heusler alloys. J. Magn. Magn. Mater., 131:417–426, 1994.

[23] Stephen Blundell. Magnetism in condensed matter. OUP Oxford, 2001.

[24] Kulbhushan Mishra and P.A. Bhobe. Magnetic properties and identification of griffiths-like phase in Mn_2FeSi heusler antiferromagnet. J. Alloys Compd., 970:172611, 2024.

[25] Snehashish Chatterjee, Saurav Giri, Subham Majumdar, Prabir Dutta, Pintu Singha, and Aritra Banerjee. Observation of griffiths-like phase in the quaternary heusler compound NiFeTiSn. J. Condens. Matter Phys., 34(29), 2022.

[26] K.H.J. Buschow A.P. Ramirez. Handbook of magnetic materials. Elsevier Science B.V, 539:423, 2001.

[27] Kavita Yadav, Mohit K Sharma, Sanjay Singh, and K Mukherjee. Exotic magnetic behaviour and evidence of cluster glass and griffiths-

like phase in heusler alloys $Fe_{2-x}Mn_xCrAl$ ($0 \leq x \leq 1$). Sci. Rep., 9, 2019.

[28] Tamalika Samanta, PA Bhobe, A Das, A Kumar, and AK Nigam. Reentrant cluster glass and stability of ferromagnetism in the Ga_2MnCo heusler alloy. Phys. Rev. B, 97:184421, 2018.

[29] Jyoti Sharma, KG Suresh, and Aftab Alam. Large exchange bias in Mn-Ni-Sn heusler alloys: Role of cluster spin glass state. Phys. Rev. B, 107:054405, 2023.

[30] Shuvankar Gupta, Sudip Chakraborty, Santanu Pakhira, Anis Biswas, Yaroslav Mudryk, Amit Kumar, Bodhoday Mukherjee, Gunadhor S Okram, Amitabh Das, Vitalij K Pecharsky, et al. Experimental observation of spin glass state in the highly disordered quaternary heusler alloy FeRuMnGa. Phys. Rev. B, 107:184408, 2023.

[31] E. M. Chudnovsky, W. M. Saslow, and R. A. Serota. Ordering in ferromagnets with random anisotropy. Phys. Rev. B, 33:251, 1986.

[32] Ritwik Saha, V. Srinivas, and T. V. Chandrasekhar Rao. Evolution of ferromagnetic-like order in $Fe_2V_{1-x}Cr_xAl$. Phys. Rev. B, 79:174423, 2009.

[33] P. M. Gehring, M. B. Salamon, A. del Moral, and J. I. Arnaudas. Magnetic static and scaling properties of the weak random-axis magnet $Dy_xY_{1-x}Al_2$. Phys. Rev. B, 41:9134, 1990.

[34] Ronald Fisch. Cubic models with random anisotropy. Phys. Rev. B, 48:15764, 1993.

[35] L D Landau and I Pomeranchuk. On the properties of metals at very low temperatures. Phys. Z. Sowjet, 10:649, 1936.

[36] W. G. Baber and Nevill Francis Mott. The contribution to the electrical resistance of metals from collisions between electrons. Proc. R. Soc. London Ser, 158:383, 1937.

[37] Patrick A. Lee and T. V. Ramakrishnan. Disordered electronic systems. Rev. Mod. Phys., 57, 1985.

[38] R. W. Cochrane, R. Harris, J. O. Ström-Olson, and M. J. Zuckermann. Structural manifestations in amorphous alloys: Resistance minima. Phys. Rev. Lett., 35:676, 1975.

[39] R. W. Cochrane, R. Harris, J. O. Ström-Olson, and M. J. Zuckermann. Structural manifestations in amorphous alloys: Resistance minima. Phys. Rev. Lett., 35, 1975.

[40] M A Continentino and N Rivier. On the resistivity of amorphous ferromagnets. Journal of Physics F: Metal Physics, 8, 1978.

[41] D. Dahlberg, K. V. Rao, and K. Fukamichi. Magnetoresistance studies of melt-spun amorphous $Fe_{1-x}Zr_x$ ferromagnets. J. Appl. Phys., 55, 1984.

[42] D. Gómez Plaza, L. Fernández Barquín, J. García Soldevilla, R. Antras, and J.C. Gómez Sal. Annealing and magnetic field effects on the resistivity of Fe-rich Fe-Zr glasses. Solid State Commun., 102, 1997.

[43] B.L. Altshuler and A.G. Aronov. Chapter 1 - electron–electron interaction in disordered conductors. In Electron–Electron Interactions in Disordered Systems, volume 10. Elsevier, 1985.

[44] N. F. Mott and E. A. Davis. Electron processes in non-crystalline materials. Oxford, I, 1971.

[45] T. E. Faber and J. M. Ziman. A theory of the electrical properties of liquid metals. Philos. Mag, 11, 1965.

[46] P. J. Cote and L. V. Meisel. Origin of saturation effects in electron transport. Phys. Rev. Lett., 40, 1978.

[47] R. Harris, M. Shalmon, and M. Zuckermann. Negative temperature coefficient of electrical resistivity in disordered metallic alloys. Phys. Rev. B, 18, 1978.

[48] U Mizutani, M Tanaka, and H Sato. Studies of negative tcr and electronic structure of nonmagnetic metallic glasses based on Y and La. J. Phys. F. Met. Phys, 17, 1987.

[49] Daniel Gnida, Kamil Ciesielski, and Dariusz Kaczorowski. Origin of the negative temperature coefficient of resistivity in the half-heusler antimonides LuNiSb and YPdSb. Phys. Rev. B, 103:174206, 2021.

[50] M Pollak and B. Shklovskii. Hopping Transport in Solids. Elsevier, North Holland, 1991.

[51] N. F. Mott. Conduction in non-crystalline materials. Philos. Mag, 19, 1969.

[52] A L Efros and B I Shklovskii. Coulomb gap and low-temperature conductivity of disordered systems. J. Phys. C: Solid State Phys, 8, 1975.

[53] Juan Rodríguez-Carvajal. Recent advances in magnetic structure determination by neutron powder diffraction + fullprof. Phys. B: Condens. Matter, 192:55–69, 1993.

[54] B Ravel and M Newville. Athena, artemis, hephaestus: data analysis for X-ray absorption spectroscopy using ifeffit. Journal of synchrotron radiation, 12:537–541, 2005.

[55] Paolo Giannozzi, Stefano Baroni, Nicola Bonini, Matteo Calandra, Roberto Car, Carlo Cavazzoni, Davide Ceresoli, Guido L Chiarotti, Matteo Cococcioni, Ismaila Dabo, and et al. Quantum espresso: a modular and open-source software project for quantum simulations of materials. J. Phys. Condens. Matter, 21:395502, 2009.

[56] P Giannozzi, O Andreussi, T Brumme, O Bunau, M Buongiorno Nardelli, M Calandra, R Car, C Cavazzoni, D Ceresoli, M Cococcioni,

N Colonna, I Carnimeo, A Dal Corso, S de Gironcoli, P Delugas, R A DiStasio, A Ferretti, A Floris, G Fratesi, G Fugallo, R Gebauer, U Gerstmann, F Giustino, T Gorni, J Jia, M Kawamura, H-Y Ko, A Kokalj, E Küçükbenli, M Lazzeri, M Marsili, N Marzari, F Mauri, N L Nguyen, H-V Nguyen, A Otero de-la Roza, L Paulatto, S Poncé, D Rocca, R Sabatini, B Santra, M Schlipf, A P Seitsonen, A Smogunov, I Timrov, T Thonhauser, P Umari, N Vast, X Wu, and S Baroni. Advanced capabilities for materials modeling with quantum espresso. J. Phys. Condens. Matter, 29:465901, 2017.

[57] John P. Perdew, Kieron Burke, and Matthias Ernzerhof. Generalized gradient approximation made simple. Phys. Rev. Lett., 77:3865–3868, 1996.

[58] S. Chaudhuri, Velaga Srihari, A. K. Nigam, and P. A. Bhobe. Origin of the magnetic ground state developed upon si, ge, and sb-substitution at sn site in Fe_2TiSn. J. Appl. Phys., 126(8), 2019.

[59] S Chaudhuri, P A Bhobe, and A K Nigam. Possible half-metallicity and variable range hopping transport in Sb-substituted Fe_2TiSn heusler alloys. J. Phys.: Condens. Matter, 30:015703, 2017.

[60] S. Chaudhuri, D. Salas, V. Srihari, E. Welter, I. Karaman, and P. A. Bhobe. Half metallicity in cr substituted Fe_2TiSn. Sci. Rep., 11:524, 2021.

[61] S Chaudhuri, P A Bhobe, Arpan Bhattacharya, and A K Nigam. Unraveling the physical properties and superparamagnetism in anti-site disorder controlled Fe_2TiSn. J. Phys.: Condens. Matter, 31:045801, 2018.

[62] Ilaria Pallecchi, Daniel I. Bilc, Marcella Pani, Fabio Ricci, Sébastien Lemal, Philippe Ghosez, Philippe Ghosez, and Daniele Marré. Roles of defects and Sb-doping in the thermoelectric properties of full-heusler Fe_2TiSn. ACS Appl. Mater. Interfaces, 14:25722–25730, 2022.

[63] Ilaria Pallecchi, Marcella Pani, Fabio Ricci, Sébastien Lemal, Daniel I. Bilc, Philippe Ghosez, Cristina Bernini, Niccolò Ardoino, Gianrico Lamura, and Daniele Marré. Thermoelectric properties of chemically substituted full-heusler $Fe_2TiSn_{1-x}Sb_x$ (x = 0, 0.1, 0.2) compounds. Phys. Rev. Mater., 2:075403, 2018.

[64] I Gavrikov, M Seredina, M Zheleznyy, I Shchetinin, D Karpenkov, A Bogach, Ratnamala Chatterjee, and V Khovaylo. Magnetic and transport properties of Mn_2FeAl. J. Magn. Magn. Mater., 478:55–58, 2019.

[65] Tanja Graf, Claudia Felser, and Stuart S.P. Parkin. Simple rules for the understanding of heusler compounds. Prog. Solid State Chem., 39:1–50, 2011.

[66] Varaprasad Bollapragada, Ananthakrishnan Srinivasan, Y.K. Takahashi, Hayashi Masamitsu, A. Rajanikanth, and Kazuhiro Hono. Spin polarization and gilbert damping of $Co_2FeGa_xGe_{1-x}$ heusler alloys. Acta Materialia, 60:6257–6265, 2012.

[67] S Chaudhuri, P A Bhobe, Arpan Bhattacharya, and A K Nigam. Unraveling the physical properties and superparamagnetism in anti-site disorder controlled Fe_2TiSn. J. Phys. Condens. Matter, 31:045801, 2018.

[68] Thorsten Krenke, Mehmet Acet, Eberhard F Wassermann, Xavier Moya, Lluís Mañosa, and Antoni Planes. Martensitic transitions and the nature of ferromagnetism in the austenitic and martensitic states of Ni-Mn-Sn alloys. Phys. Rev. B: Condens. Matter Phys., 72:014412, 2005.

[69] Jitender Kumar, Soumendra Nath Panja, Shanu Dengre, and Sunil Nair. Identification of a griffiths singularity in a geometrically frustrated antiferromagnet. Phys. Rev. B, 95:054401, 2017.

[70] RM Eremina, II Fazlizhanov, IV Yatsyk, KR Sharipov, AV Pyataev, H-A Krug von Nidda, N Pascher, A Loidl, KV Glazyrin, and Ya M

Mukovskii. Phase separation in paramagnetic $Eu_{0.6}La_{0.4-x}Sr_xMnO_3$. Phys. Rev. B Condens. Matter Phys., 84:064410, 2011.

[71] Kaipamangalath Aswathi, Jasnamol P Palakkal, and Manoj Raama Varma. Observation of griffiths-like phase in Y_2CrMnO_6 perovskites. J. Magn. Magn. Mater., 514:167276, 2020.

[72] Jasnamol P Palakkal, Cheriyedath Raj Sankar, and Manoj Raama Varma. Multiple magnetic transitions, griffiths-like phase, and magnetoresistance in La_2CrMnO_6. J. Appl. Phys., 122(7), 2017.

[73] AK Pramanik and A Banerjee. Griffiths phase and its evolution with mn-site disorder in the half-doped manganite $Pr_{0.5}Sr_{0.5}Mn_{1-y}Ga_yO_3$ ($y = 0.0$, 0.025, and 0.05). Phys. Rev. B: Condens. Matter Phys., 81:024431, 2010.

[74] Robert B Griffiths. Nonanalytic behavior above the critical point in a random ising ferromagnet. Phys. Rev. Lett., 23:17, 1969.

[75] Krishanu Ghosh, Chandan Mazumdar, R Ranganathan, and S Mukherjee. Griffiths phase behaviour in a frustrated antiferromagnetic intermetallic compound. Sci. Rep., 5:15801, 2015.

[76] MK Majee, Preeti Anand Bhobe, and AK Nigam. Griffiths phase in antiferromagnetic $CuCr_{0.95}Ti_{0.05}O_2$. J. Magn. Magn. Mater., 485:112–117, 2019.

[77] Andrzej Ślebarski, J Goraus, and Marcin Fijałkowski. Short-range ferromagnetic correlations in disordered Fe_2VGa with distinct similarities to the griffiths phase. Phys. Rev. B, 84(7):075154, 2011.

[78] A. R. Denton and N. W. Ashcroft. Vegard's law. Phys. Rev. A, 43:3161, 1991.

[79] Patrick A. Lee and T. V. Ramakrishnan. Disordered electronic systems. Rev. Mod. Phys., 57:287, 1985.

[80] O. O. Bernal, D. E. MacLaughlin, H. G. Lukefahr, and B. Andraka. Copper nmr and thermodynamics of $UCu_{5-x}Pd_5$: Evidence for kondo disorder. Phys. Rev. Lett., 75:2023, 1995.

[81] S. Chaudhuri, Velaga Srihari, A. K. Nigam, and P. A. Bhobe. Origin of the magnetic ground state developed upon Si, Ge, and Sb-substitution at Sn site in Fe_2TiSn. J. Appl. Phys., 126, 2019.

[82] Siham Ouardi, Gerhard H. Fecher, Claudia Felser, and Jurgen Kubler. Realization of spin gapless semiconductors: the heusler compound Mn_2CoAl. Phys. Rev. Lett., 110:100401, 2013.

[83] Y. Venkateswara, Sachin Gupta, S. Shanmukharao Samatham, Manoj Raama Varma, Enamullah, K. G. Suresh, and Aftab Alam. Competing magnetic and spin-gapless semiconducting behavior in fully compensated ferrimagnetic CrVTiAl: Theory and experiment. Phys. Rev. B, 97:054407, 2018.

[84] Lakhan Bainsla, A. I. Mallick, M. Manivel Raja, A. A. Coelho, A. K. Nigam, D. D. Johnson, Aftab Alam, and K. G. Suresh. Origin of spin gapless semiconductor behavior in CoFeCrGa: Theory and experiment. Phys. Rev. B, 92:045201, 2015.

[85] Andrzej Ślebarski. Electron-correlation effects in a disordered Fe_2TiSn heusler alloy. J. Phys. D Appl. Phys., 39:856, 2006.

[86] A. Ślebarski, M. B. Maple, A. Wrona, and A. Winiarska. Kondo-type behavior in $Fe_{2-x}M_xTiSn$ (M = Co, Ni). Phys. Rev. B, 63:214416, 2001.

[87] S Chaudhuri, P A Bhobe, and A K Nigam. Possible half-metallicity and variable range hopping transport in Sb-substituted Fe_2TiSn heusler alloys. J. Phys. Condens. Matter, 30:015703, 2017.

[88] S. Chaudhuri, D. Salas, V. Srihari, E. Welter, I. Karaman, and P. A. Bhobe. Half metallicity in Cr substituted Fe_2TiSn. Sci. Rep., 11:524, 2021.

[89] P. A. Lee and T. V. Ramakrishnan. Magnetoresistance of weakly disordered electrons. Phys. Rev. B, 26:4009, 1982.

[90] V. Hien-Hoang, NK. Chung, and HJ. Kim. Electrical transport properties and Kondo effect in $La_{1-x}Pr_xNiO_{3-\delta}$ thin films. Sci Rep, 11:5391, 2021.

[91] Sayandeep Ghosh, R. G. Tanguturi, P. Pramanik, D. C. Joshi, P. K. Mishra, S. Das, and S. Thota. Low-temperature anomalous spin correlations and Kondo effect in ferromagnetic $SrRuO_3/LaNiO_3/La_{0.7}Sr_{0.3}MnO_3$ trilayers. Phys. Rev. B, 99:115135, 2019.

[92] Rik Dey, Tanmoy Pramanik, Anupam Roy, Amritesh Rai, Samaresh Guchhait, Sushant Sonde, Hema C. P. Movva, Luigi Colombo, Leonard F. Register, and Sanjay K. Banerjee. Strong spin-orbit coupling and zeeman spin splitting in angle-dependent magnetoresistance of Bi_2Te_3. Applied Physics Letters, 104, 2014.

[93] Tsuyoshi Sekitani, Michio Naito, and Noboru Miura. Kondo effect in underdoped n-type superconductors. Phys. Rev. B, 67:174503, 2003.

[94] M. Vasundhara, V. Srinivas, and V. V. Rao. Evidence for cluster glass behavior in Fe_2VAl heusler alloys. Phys. Rev. B, 78:064401, 2008.

[95] Sanchayita Mondal, Chandan Mazumdar, R. Ranganathan, Eric Alleno, P. C. Sreeparvathy, V. Kanchana, and G. Vaitheeswaran. Ferromagnetically correlated clusters in semimetallic Ru_2NbAl heusler alloy and its thermoelectric properties. Phys. Rev. B, 98:205130, 2018.

[96] Jincang Zhang, Yan Xu, Shixun Cao, Guixin Cao, Yufeng Zhang, and Chao Jing. Kondo-like transport and its correlation with the spin-glass phase in perovskite manganites. Phys. Rev. B, 72:054410, 2005.

[97] N. T. Huy, A. Gasparini, J. C. P. Klaasse, A. de Visser, S. Sakarya, and N. H. van Dijk. Ferromagnetic quantum critical point in URhGe doped with Ru. Phys. Rev. B, 75:212405, 2007.

[98] Hyunsoo Yang, See-Hun Yang, Grzegorz Ilnicki, Jan Martinek, and Stuart S. P. Parkin. Coexistence of the kondo effect and a ferromagnetic phase in magnetic tunnel junctions. Phys. Rev. B, 83:174437, 2011.

[99] Sourabh Barua, M Ciomaga Hatnean, Martin R Lees, and Geetha Balakrishnan. Signatures of the kondo effect in VSe_2. Scientific reports, 7:10964, 2017.

[100] A. D. Hillier, D. T. Adroja, S. R. Giblin, W. Kockelmann, B. D. Rainford, and S. K. Malik. Understanding the heavy fermion behavior in $CeInPt_4$. Phys. Rev. B, 76:174439, 2007.

[101] Marcelo Jaime, Roman Movshovich, Gregory R. Stewart, Ward P. Beyermann, Mariano Gomez Berisso, Michael F. Hundley, Paul C. Canfield, and John L. Sarrao. Closing the spin gap in the Kondo insulator $Ce_3Bi_4Pt_3$ at high magnetic fields. Nature, 405:160–163, 2000.

[102] Masahiko Hiroi, Tomohito Nonoyama, Genta Adachi, Iduru Shigeta, Hirotaka Manaka, and Norio Terada. Magnetic properties of heusler compound $Fe_{1.3}Mn_{1.7}Si$. J. Phys. Conf. Ser., 969, 2018.

[103] Masahiko Hiroi, Tomohito Nonoyama, Iduru Shigeta, and Touru Yamauchi. Multiple magnetic phase transitions in $Fe_{3-x}Mn_xSi$ heusler compounds. J. Phys. Soc. Jpn., 90, 2021.

[104] JCG Tedesco, Sandra S Pedro, RJ Caraballo Vivas, Clebson Cruz, VM Andrade, AM Dos Santos, AMG Carvalho, M Costa, Pedro Venezuela, Daniel Leandro Rocco, et al. Chemical disorder determines the deviation of the slater–pauling rule for Fe_2MnSi-based heusler alloys: evidences from neutron diffraction and density functional theory. J. Phys.: Condens. Matter, 28(47):476002, 2016.

[105] S Yoon and J G Booth. Magnetic properties and structures of some ordered (FeMn)$_3$Si alloys. J. Phys. F: Met. Phys., 7, 1977.

[106] Guizhou Xu, Yurong You, Jiaxuan Tang, Hongguo Zhang, Hang Li, Xuefei Miao, Yuanyuan Gong, Zhipeng Hou, Zhenxiang Cheng, Jianli Wang, Andrew J. Studer, Feng Xu, and Wenhong Wang. Simultaneous tuning of magnetocrystalline anisotropy and spin reorientation transition via cu substitution in Mn-Ni-Ga magnets for nanoscale biskyrmion formation. Phys. Rev. B, 100:054416, 2019.

[107] Wenhong Wang, Ying Zhang, Guizhou Xu, Licong Peng, Bei Ding, Yue Wang, Zhipeng Hou, Xiaoming Zhang, Xiyang Li, Enke Liu, Shouguo Wang, Jianwang Cai, Fangwei Wang, Jianqi Li, Fengxia Hu, Guangheng Wu, Baogen Shen, and Xi-Xiang Zhang. A centrosymmetric hexagonal magnet with superstable biskyrmion magnetic nanodomains in a wide temperature range of 100–340 k. Adv. Mater., 28, 2016.

[108] O. Meshcheriakova, S. Chadov, A. K. Nayak, U. K. Rößler, J. Kübler, G. André, A. A. Tsirlin, J. Kiss, S. Hausdorf, A. Kalache, W. Schnelle, M. Nicklas, and C. Felser. Large noncollinearity and spin reorientation in the novel Mn$_2$RhSn heusler magnet. Phys. Rev. Lett., 113:087203, 2014.

[109] M. Gotoh, M. Ohashi, T. Kanomata, and Y. Yamaguchi. Spin reorientation in the new heusler alloys Ru$_2$MnSb and Ru$_2$MnGe. Physica B, 213-214:306–308, 1995.

[110] Lakhan Pal, K. G. Suresh, and A. K. Nigam. Effect of mn substitution on the magnetic and magneto-transport properties of Fe$_{3-x}$Mn$_x$Si (0 $\leq x \leq$ 1.25) alloys. J. Appl. Phys., 113, 2013.

[111] J. Krishna Murthy and A. Venimadhav. Magnetization reversal phenomena and bipolar switching in La$_{1.9}$Bi$_{0.1}$FeCrO$_6$. Physica B, 448:162–166, 2014.

[112] Sudipta Mahana, Bipul Rakshit, Raktima Basu, Sandip Dhara, Boby Joseph, U. Manju, Subhendra D. Mahanti, and D. Topwal. Local inversion symmetry breaking and spin-phonon coupling in the perovskite $GdCrO_3$. Phys. Rev. B, 96:104106, 2017.

[113] Tusita Sau, Shivani Sharma, Poonam Yadav, R. Baumbach, T. Siegrist, Alok Banerjee, and N. P. Lalla. First-order nature of the spin-reorientation phase transition in $SmCrO_3$. Phys. Rev. B, 106, 2022.

[114] Anupam K. Singh, Parul Devi, Nisha Shahi, K.K. Dubey, Sanjay Singh, and Dhananjai Pandey. Nature of magnetic transitions and evidence for magnetoelastic coupling in the biskyrmion-host hexagonal compound $MnNiGa$. J. Alloys Compd., 954:170082, 2023.

[115] Arun Kumar, Pascal Manuel, and Sunil Nair. Successive magnetic phase transitions with magnetoelastic and magnetodielectric coupling in the ordered triple perovskite $Sr_3CaRu_2O_9$. Phys. Rev. Materials, 8:024405, 2024.

[116] Papiya Saha, R Nithya, AT Sathyanarayana, Amitabh Das, K Vinod, Suman Karmakar, and Rajeev Rawat. Magnetoelastic coupling with inverse magnetocaloric effect observed in Sr_2YRuO_6. J. Magn. Magn. Mater., 574:170682, 2023.

[117] Arun Kumar, SD Kaushik, V Siruguri, and Dhananjai Pandey. Evidence for two spin-glass transitions with magnetoelastic and magnetoelectric couplings in the multiferroic $(Bi_{1-x}Ba_x)(Fe_{1-x}Ti_x)O_3$ system. Phys. Rev. B, 97:104402, 2018.

[118] Kausik Sengupta and E. V. Sampathkumaran. Field-induced first-order magnetic phase transition in an intermetallic compoundNd_7Rh_3: Evidence for kinetic hindrance, phase coexistence, and percolative electrical conduction. Phys. Rev. B, 73:020406, 2006.

[119] A. Tekgül, M. Acet, M. Farle, and N. Ünal. Kinetic arrest of the ferrimagnetic state in indium-doped $Mn_{1.82}Co_{0.18}Sb$. J. Alloys Compd., 695:418–425, 2017.

[120] Ajaya K. Nayak, Michael Nicklas, Chandra Shekhar, and Claudia Felser. Kinetic arrest related to a first-order ferrimagnetic to antiferromagnetic transition in the heusler compound Mn_2PtGa. J. Appl. Phys., 113, 2013.

[121] Tapas Samanta, Ahmad Us Saleheen, Daniel L. Lepkowski, Alok Shankar, Igor Dubenko, Abdiel Quetz, Mahmud Khan, Naushad Ali, and Shane Stadler. Asymmetric switching-like behavior in the magnetoresistance at low fields in bulk metamagnetic heusler alloys. Phys. Rev. B, 90:064412, 2014.

[122] S. Chatterjee, S. Giri, S. Majumdar, and S. K. De. Metastability and magnetic memory effect in $Ni_2Mn_{1.4}Sn_{0.6}$. Phys. Rev. B, 77:012404, 2008.

[123] H. Kuwahara, Y. Tomioka, A. Asamitsu, Y. Moritomo, and Y. Tokura. A first-order phase transition induced by a magnetic field. Science, 270:961–963, 1995.

[124] Durga Paudyal, V K Pecharsky, and K A Gschneidner. Origins of ferromagnetism and antiferromagnetism in Gd_5Ge_4. J. Condens. Matter Phys., 20:235235, 2008.

[125] C Magen, L Morellon, P A Algarabel, C Marquina, and M R Ibarra. Magnetoelastic behaviour of Gd_5Ge_4. J. Phys.: Condens. Matter, 15:2389, 2003.

[126] Z. W. Ouyang, H. Nojiri, S. Yoshii, G. H. Rao, Y. C. Wang, V. K. Pecharsky, and K. A. Gschneidner. Field-induced magnetostructural transition in Gd_5Ge_4 studied by pulsed magnetic fields. Phys. Rev. B, 77:184426, 2008.

[127] Y. Y. Wu, Z. C. Xia, Z. W. Ouyang, Y. Huang, and L. Li. High magnetic-field-induced phase transitions and refined magnetic phase diagram of Gd$_5$Ge$_4$. <u>J. Appl. Phys.</u>, 109, 2011.